# MONOPULSE PROCESSING AND TRACKING OF MANEUVERING TARGETS

A Thesis
Presented to
The Academic Faculty

by

John D. Glass

In Partial Fulfillment
of the Requirements for the Degree
Doctor of Philosophy in the
School of Electrical and Computer Engineering

Georgia Institute of Technology
May 2015

# MONOPULSE PROCESSING AND TRACKING OF MANEUVERING TARGETS

Approved by:

Dr. Aaron Lanterman, Advisor
School of Electrical and Computer Engineering
*Georgia Institute of Technology*

Dr. James H. McClellan
School of Electrical and Computer Engineering
*Georgia Institute of Technology*

Dr. William Dale Blair
Georgia Tech Research Institute
*Georgia Institute of Technology*

Dr. Doug Williams
School of Electrical and Computer Engineering
*Georgia Institute of Technology*

Dr. Luca Dieci
School of Mathematics
*Georgia Institute of Technology*

Date Approved: 26 March 2015

*To my parents, J.B. and Pam*

# ACKNOWLEDGEMENTS

First, I would like to thank my advisor Dr. Aaron Lanterman. Aaron was always there when I needed him, and he knew exactly when to guide me and when to let me figure things out on my own. Second, I would like to thank Dr. Dale Blair of GTRI. Dale was very helpful in the selection of a relevant topic of research in the field of radar tracking. Furthermore, I thank Dale for providing much needed advice on constructing research papers, particularly in presenting research in a meaningful way. In my opinion, the presentation of research is often more important than the research itself, and this philosophy stems from my interactions with Dale. I would also like to thank Donnie Smith, Dr. George Brown, Paul Miceli, Dr. Jim Sangston, Dr. Mark Smith, and many other individuals of GTRI for their helpful and often challenging discussions on my research. Finally, I would like to thank all of my friends and family who helped me endure the tough stretches of graduate school. Without them, I would not have made it this far.

# TABLE OF CONTENTS

## LIST OF TABLES

# LIST OF FIGURES

# SUMMARY

Surveillance radars detect the presence of targets and estimate their locations. With several measurements collected over time, tracking algorithms are used to compute track state estimates and predict future locations. This dissertation re-examines some of the often ignored practical considerations of radar tracking.

With the advent of digital computers, modern radars now use sampled versions of received signals for processing. Sampling rates used in practice result in multiple adjacent samples containing target energy, and those samples are statistically correlated. This is often called range bin straddling and is ubiquitous in modern radar systems. Instead of simply treating bin straddling as an undesired loss in signal power, as in traditional radar processing, we provide new detection and estimation techniques that take advantage of the observed correlation in radar signal samples. In this dissertation, the average loglikelihood ratio test (ALLRT) is derived and shown to outperform traditional radar detectors. We further show that the ALLRT rivals traditional detectors that use oversampled radar signals. This work represents the first appearance of the ALLRT formalism in detection theory.

Using a maximum-likelihood approach that incorporates the observed correlation between samples, we develop a new method for the estimation of monopulse target direction-of-arrival (DOA) and target range. We further derive new closed-form Cramér-Rao lower bounds (CRLBs) on unbiased parameter estimates of target DOA and target range that treat target strength, target DOA, and target range as unknown parameters. Using the CRLB for target DOA, bin-straddling is shown as a direct loss in target SNR, and the magnitude of the loss depends on the functional form of the transmitted waveform. The new target DOA estimator outperforms an existing technique by a factor of up to two in root mean square error. Since tracking algorithms require an error variance on monopulse measurements, we propose using the generalized Cramér-Rao lower bound (GCRLB), which is the CRLB evaluated at estimated parameters. The average normalized estimation error squared metric is used to analyze the statistical consistency and statistical efficiency of the estimates. This work represents the first appearance of the GCRLB formalism in estimation theory.

With the advent of agile-beam surveillance radars with programmable energy waveforms, optimal scheduling of radar resources is a topic of interest. Reasonable approaches in the literature suggest selecting waveform energy based upon a desired SNR level. However, optimal use of radar resources for the tracking of highly maneuverable targets is not treated in the literature. Tracking highly maneuverable targets is also of theoretical interest since multiple kinematic models of differing state dimensions are often required, causing issues in the model mixing step of the interacting multiple model filter. Here, we extend a recently proposed unbiased mixing procedure from the case of two kinematic models to three, and use this procedure in the comparison of two competing multiple model filtering methods. Furthermore, we introduce the radar management operating curve (RMOC), which shows the fundamental tradeoff in radar time and energy, to aid radar designers in the selection of an operating SNR level. With a given set of hardware constraints and set of waveforms, the RMOC can be used to select an optimal operating SNR level.

# CHAPTER I

# INTRODUCTION

In order to track and report on targets, surveillance radars detect their presence and estimate their locations. Since radar systems operate in the presence of random noise, concepts from detection and estimation theory are often applied to effectively perform this task. Each radar detection leads to location estimates in terms of range and angle. Detections and corresponding measurements are associated to predicted target state estimates, and they are further used in the tracking to estimate the kinematic state of the target for display and other purposes. Through effective use of radar resources along with reliable state predictions, a secondary task of surveillance radar systems is to maximize the number of tracked objects.

Monopulse radars use a simultaneous lobing technique to provide accurate angle estimates of a target. Pulse compression techniques are used in radar systems to provide voltage gain, and to refine estimates of the target location in range. In practice, in-phase and quadrature voltage samples of the matched filter output are provided to signal processing algorithms in radar software for detection, range estimation, and angle estimation. Traditionally, each sample is treated individually, since target energy is assumed to be contained in a single sample. However, in practice, samples rarely occur at the peak of the matched filter response, and target energy is contained in mutliple adjacent samples, often called range bin straddling. Range bin straddling is ubiquitous in surveillance radar systems, and it is important to account for its effects in the loss budget when assessing system performance in terms of detection and estimation. Generally, rough generic estimates are often quoted. Furthermore, bin-straddling effects on monopulse angle estimation have not previously been well studied.

Detections and corresponding measurements reported from the signal processing algorithms are clustered together to form tracks. State estimation techniques are typically used on the clustered measurements to provide kinematic track states. The selection of a measurement clustering algorithm along with a corresponding state estimation technique is an issue of design, and it is typically dictated by the quality of the sensing environment and expected types of targets. For maneuverable air targets, the interacting multiple model (IMM) filter is a preferred tracking algorithm. Typically, a maneuver model is coupled with a non-maneuver model, and observed measurement likelihoods dictate the dominance of either mode in the overall kinematic track state estimate. Numerous maneuver models appear in the literature. However, clear guidelines on the selection of one maneuver model over the others has not been well studied. Since the state dimension of the non-maneuver model is often less than the state dimension of the maneuver model, issues can arise during the model mixing phase of the IMM filter. A typical approach of augmenting the missing elements with zeros for purposes of mixing can result in estimator bias in the extra elements of the state vector.

The fundamental radar resources are radar time and radar energy. Each radar dwell (transmit and recieve sequence) consumes a certain amount of radar time that depends on the number of pulses, range of receive window, and nominal processing time. Radar energy is proportional to the amount of time that the radar transmitter is active. In practice, radar energy is limited by duty cycle constraints, and violation can result in failure of the antenna elements and internal electronics. Under the constraint of meeting system performance requirements, agile beam radars with waveforms of varying energy have the ability to optimize the use of radar resources. Reasonable approaches in the literature suggest selecting waveform energy based upon a desired SNR level. Existing literature has studied the case of non-maneuvering targets with single kinematic filtering methods. However, impacts of the IMM filtering and maneuvering targets on the selection of desired SNR levels has not been previously well studied.

A focus of this dissertation is the re-examination of detection and range and angle estimation, in light of the range bin straddling phenomenon. In particular, a more general systematic treatment of matched filter sampling is used to overcome losses due to bin-straddling. While oversampling of radar signals is an alternative approach to overcome these losses, oversampling may not be cost effective or even possible with the advent of high-bandwidth radar signals. Through a new systematic treatment of the sampling process, losses due to sampling of radar signals are overcome through new processing techniques. A focus is placed on providing simple detectors and estimators that can be implemented in current practical radar systems. A new average loglikelihood ratio test (ALLRT) detector is proposed in Chapter 3, which provides detection performance that rivals oversampled radar signals. Derivation of the ALLRT is outlined in Appendix A This dissertation represents the first appearance of the ALLRT formalism in the literature. In Chapter 4, issues associated with standard monopulse ratio estimation are discussed, and new joint-bin monopulse processing techniques for estimation of target range and direction-of-arrival (DOA) are proposed. For use in tracking algorithms, error variance estimates are required for parameter estimates. We propose the generalized Cramér-Rao lower bound (GCRLB), which is the Cramér-Rao lower bound evaluated at maximum-likelihood estimates, as a variance report on the joint-bin monopulse estimates. Derivations of the new joint-bin monopulse processing techniques and CRLBs are outlined in Appendix B. This work represents the first appearance of the GCRLB formalism in the literature. The required number of pulses and SNR levels for statistical efficiency and consistency of the proposed joint-bin monopulse processing techniques are provided. Statistical efficiency is achieved when estimation errors achieve the CRLB, and variance consistency is achieved when reported error variance estimates reflect true estimation errors.

A second focus of this research is to study the tracking and energy management considerations of tracking highly maneuverable targets. Two configurations of the IMM estimator often found in the literature are investigated for tracking target maneuvers in three dimensional space. A performance comparison is the two IMM estimators is provided. As part of this research, unbiased mixing for the IMM estimator is extended to the three mode case as outlined in Appendix C. In Chapter 5, an IMM estimator that includes a 3D coordinated turn kinematic model is recommended as a state estimation algorithm for the tracking of a highly maneuverable air targets. Furthermore, a new radar management operating curve is proposed to illustrate the tradeoff between radar time and energy, as they relate to an overall operating SNR level. Although operating SNR values have been studied in the literature, the effects of highly maneuverable targets have not been considered.

Many of the contributions contained in this dissertation build upon existing literature in monopulse radar tracking. The next chapter includes relevant prerequisite material from the literature.

# CHAPTER II

# BACKGROUND

Radar tracking with monopulse systems has been studied extensively in the literature. Rudy Kalman introduced the Kalman filter in 1960, which is arguably one of the most important contributions to applied mathematics in the last century [29]. Following Kalman, Athans contributed the extended Kalman filter in 1968 [2], and Blom contributed the interacting multiple model filter in 1988 [14], both of which are invaluable to modern radar tracking algorithms. In terms of angle estimation in monopulse systems, the work of Mosca in 1969 [34] is considered foundational. Many authors have studied monopulse systems from a parameter estimation point of view, with a good example being the work of Blair in 1998 [8]. This chapter provides a brief overview of monopulse processing and state estimation techniques as they relate to the contributions of this dissertation.

## *2.1 Amplitude Comparison Monopulse*

Amplitude comparison monopulse systems use a simultaneous lobing technique to determine the angular position of a target [43]. A pulse is emitted to illuminate a target, and the receiver forms sum and difference signals of the scattered target reflection with two squinted sub-beams for each coordinate. An illustration of a monopulse radar with squinted sub-beams is provided in Figure 1, and an example of sum and difference voltage patterns is provided in Figure 2. The ratio of the (noiseless) difference pattern voltage to the (noiseless) sum pattern voltage defines a unique off-axis angle within the main lobe of the sum pattern beam. This ratio is called the monopulse ratio; an example is illustrated in Figure 3. The ratio can be approximated as nearly linear within one-half of the main beamwidth of the sum pattern. The slope of the linear region is often termed the monopulse error slope [43].

In practice, radar waveforms are transmitted at the operating frequency of the radar. For example, X-Band radars are common in practice and operate around 9-10 GHz. Received signals are demodulated onto baseband, resulting in in-phase and quadrature parts of the

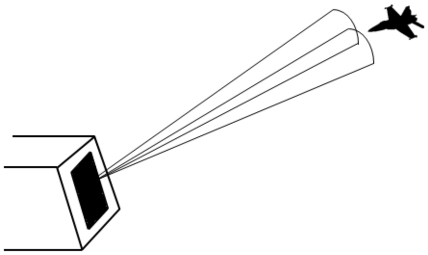

Figure 1: Illustration of an amplitude-comparison monopulse system.

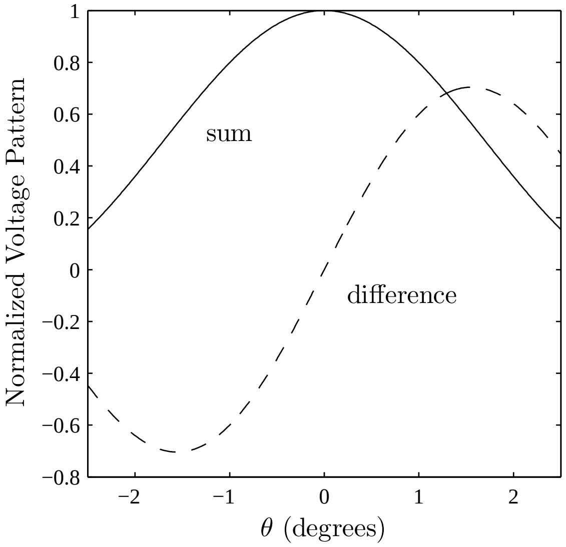

Figure 2: Examples of monopulse sum and difference voltage patterns.

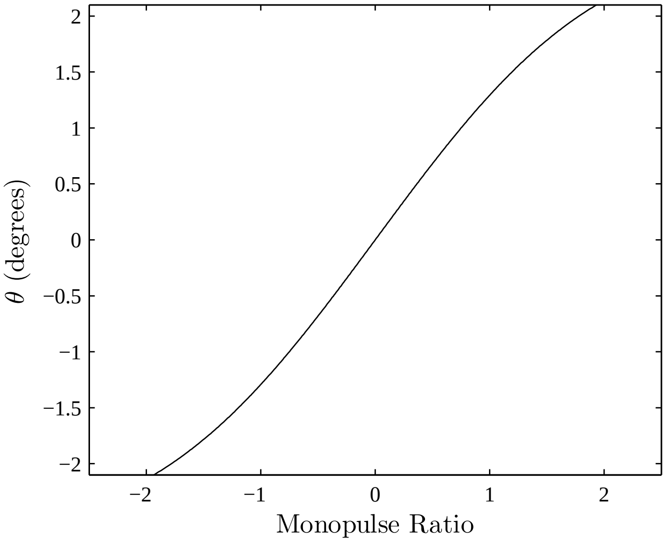

Figure 3: Example monopulse ratio versus off-boresight angle.

sum and difference channels. Some radar signal processing algorithms take advantage of the return signal phase for detection purposes and Doppler processing [39]. This work does not specifically deal with the return signal phase due to the assumption of Rayleigh targets, as will be outlined shortly. Other aspects regarding operating frequencies of a radar are beyond the scope of this work; readers are referred to [39] among many others.

At first glance, a monopulse radar system may appear as an array signal processing system as described in [28] for the case of two array elements. However, this is not the case since the antenna elements in [28] are omnidirectional, whereas the two squinted sub-beams in a monopulse system typically have high directional gain. For a monopulse system the beamforming "gains" described in [28] are formed in a somewhat ad-hoc way for a "focused" region of interest (i.e., the region illuminated by the sum channel). From an angle-of-arrival estimation perspective, monopulse systems are closely related to the beamforming techniques of [28]; since out of the scope of this study, curious readers are referred to [36].

In practice, the measured sum and difference channels are corrupted by thermal noise. Upon detecting the presence of a target using the measured voltage levels of the sum channel, a DOA must be estimated from the noisy signals. A straightforward approach to DOA estimation is direct computation of the monopulse ratio using the measured voltages of the sum and difference channels. Using the observed monopulse ratio provides reasonable estimation performance for high SNR situations, especially if targets are located near boresight. However, as reported in the literature, the observed monopulse ratio suffers from estimator bias and high error variance for the case of low SNR targets, especially when the targets are located off-boresight [34]. Furthermore, if multiple targets are present in the beam, then the monopulse ratio can become highly corrupted. Much work has been devoted to optimal estimation of target DOA (some examples are [34], [43], [47], [8], [9], [10], and [50]).

Assuming a single point target is illuminated in a radar beam, the voltage signals at the output of the matched filters of a monopulse system can be expressed as

$$\tilde{s}_c(t) = \alpha G_\Sigma(\theta) G_\Sigma(\theta) e^{j\phi} r(t-\tau) + \tilde{n}_{cs}(t), \tag{1}$$

$$\tilde{d}_c(t) = \alpha G_\Sigma(\theta) G_\Delta(\theta) e^{j\phi} r(t-\tau) + \tilde{n}_{cd}(t), \tag{2}$$

where

$\tilde{s}_c(t) =$ complex-valued sum channel signal,

$\tilde{d}_c(t) =$ complex-valued difference channel signal,

$\alpha =$ voltage signal amplitude of the target,

$\theta =$ target AOA,

$G_\Sigma(\theta) =$ sum pattern voltage gain at $\theta$,

$G_\Delta(\theta) =$ difference pattern voltage gain at $\theta$,

$\phi =$ return signal phase,

$r(t) =$ autocorrelation function of the transmitted pulse,

$\tilde{n}_{cs}(t) =$ zero-mean complex Gaussian noise process in sum channel,

$\tilde{n}_{cd}(t) =$ zero-mean complex Gaussian noise process in difference channel,

$\tau =$ round-trip time delay from the target.

Note that the sum channel gain pattern arises in the difference channel signal because the expression is a two-way gain, and the sum beam is used to illuminate the target. Also note that complex notation is used for conciseness; in practice, the sum and difference signals have corresponding in-phase (i.e., real) and quadrature (i.e., imaginary) channels. The signal amplitude of the target can be expressed as

$$\alpha = \sqrt{\kappa \sigma_r p_0}, \tag{3}$$

where $\kappa$ is a constant proportional to transmitted power and includes elements of the radar range equation, $\sigma_r$ is the radar cross section (RCS) of the target, and $p_0$ is the matched filter gain of the waveform.[1] Under the Rayleigh target assumption, $\sqrt{\sigma_r}$ is Rayleigh distributed, and thus the voltage signal amplitude of the target is also Rayleigh distributed. Since matched filter gain is explicitly modeled as $p_0$, one may safely assume $r(0) = 1$ without any

---

[1] Matched filter gain is typically reported as the time-bandwidth product of the transmitted waveform, where time is equal to the pulsewidth.

loss of generality. Explicitly defining DOA for AOA $\theta$ as

$$\eta = \frac{G_{\Delta}(\theta)}{G_{\Sigma}(\theta)}, \tag{4}$$

and defining

$$A = \alpha G_{\Sigma}(\theta)^2, \tag{5}$$

the sum and difference channel signals can be rewritten in terms of $\eta$ as

$$\tilde{s}_c(t) = Ae^{j\phi} r(t-\tau) + \tilde{n}_{cs}(t), \tag{6}$$

$$\tilde{d}_c(t) = A\eta e^{j\phi} r(t-\tau) + \tilde{n}_{cd}(t). \tag{7}$$

Notice that since $\alpha$ is Rayleigh distributed, $A$ is also Rayleigh distributed. At the output of the matched filter, the I&Q signals are sampled with a sampling period $\Delta t$. Thus (6) and (7) become

$$s_c(b) = \tilde{s}_c(b\Delta t) = Ae^{j\phi} r(b\Delta t-\tau) + n_{cs}(b), \tag{8}$$

$$d_c(b) = \tilde{d}_c(b\Delta t) = A\eta e^{j\phi} r(b\Delta t-\tau) + n_{cd}(b), \tag{9}$$

where $b$ is an index to the samples, often called range bins. Under the Rayleigh target assumption, $\phi$ is uniformly distributed over $(-\pi, \pi]$. Denoting the second moment of $A$ as $2\beta^2$, $Re\{Ae^{j\phi}\}$ and $Im\{Ae^{j\phi}\}$ are independent zero-mean Gaussian random variables with a variance of $\beta^2$ [37]. Furthermore, assuming the in-phase noise (i.e., real part) is uncorrelated with the quadrature noise (i.e. imaginary part), quadrature samples can be treated as extra observations of the in-phase samples. Denoting $x$ as $Re\{Ae^{j\phi}\}$ (or $Im\{Ae^{j\phi}\}$, as quadrature samples are treated as another observation of the in-phase samples), the signal model can be expressed as

$$s(b) = xr(b\Delta t-\tau) + n_s(b\Delta t), \tag{10}$$

$$d(b) = x\eta r(b\Delta t-\tau) + n_d(b\Delta t). \tag{11}$$

Note that a single pulse corresponds to two independent and identically distributed (i.i.d.) observations of both (10) and (11).

The selection of a sample rate determines the magnitude of noise correlation across adjacent samples, which arises from the matched filtering process as shown in [53]. The Rayleigh range resolution (not to be confused with Rayleigh targets) of a waveform is defined as the peak to first null of the matched filter response [39]. A radar waveform that is sampled at Rayleigh resolution results in uncorrelated noise for adjacent matched filter samples. However, sampling at a rate higher than the Rayleigh resolution will result in correlated noise.

A Swerling 2 target corresponds to a Rayleigh target with pulse-to-pulse fluctuations in target amplitude and phase.[2] The target SNR for a Rayleigh target, a fundamental quantity that is used to characterize detection and estimation performance, is defined as

$$\mathfrak{R}_r = \frac{\beta^2}{\sigma_s^2}, \tag{12}$$

where $\sigma_s^2$ is the noise variance in the sum channel samples, and the total target SNR is defined as

$$\mathfrak{R}_t = N\mathfrak{R}_r, \tag{13}$$

where $N$ is the total number of pulses. Total target SNR is important since it represents the total SNR of a constant energy waveform (i.e., total pulse width) regardless of the selection of number of pulses. In this work, $\beta^2$, $\eta$, and $\tau$ are assumed as unknown parameters, whereas $\sigma_d^2$ and $\sigma_s^2$ are assumed as known parameters. Estimators for the unknown parameters $\eta$ and $\tau$ along with statistically consistent variance reports for each parameter estimate are a major focus of this thesis. In this work, $\beta^2$ is treated as a nuisance parameter and its estimation is not studied in depth.

Traditional monopulse processing literature assumes the received energy is contained in a single sample. This assumption greatly simplifies the estimation problem, since the effect of $r(b\Delta t - \tau)$ in (10) and (11) is essentially multiplication by a constant and typically treated as a loss in voltage. In practice, target energy is usually contained in multiple adjacent matched filter samples, and clustering and centroiding procedures are used to arrive at estimates of

---

[2] In a radar system, pulse-to-pulse fluctuations are often the result of frequency diversity in the radar waveform achieved through discrete frequency steps [19].

$\tau$ and $\eta$. For the single-target case, Slocumb and Blair propose using traditional monopulse processing for DOA estimates based on each individual sample, followed by standard fusion equations on those estimates [45]. For range estimation, the authors propose using an observed SNR-weighted centroid of matched filter samples to arrive at a range estimate. However, these estimators are suboptimal since they do not consider correlation between adjacent samples. By inspection of (10)-(11) correlated samples are the result of correlated noise and the sampling of the matched filter response through $r(b\Delta t - \tau)$. Furthermore, the observed correlation can be advantageous for detection and estimation purposes.

## *2.2 Radar Tracking*

In this section, some relevant concepts of radar tracking are introduced. In particular, a brief overview of state estimation is provided, and equations for the discrete Kalman filter and IMM filter are provided explicitly. The role of motion models in the IMM estimator is discussed. Relevant aspects of radar resource management, including the concept of a nominal tracking SNR and adaptive track maintenance revisit times, are also introduced.

### 2.2.1 State Estimation

Monopulse processing, as described in Chapter 2.1, is a topic of parameter estimation, whereas target tracking is considered a topic of state estimation. State estimation differs from parameter estimation in that the target state of interest evolves in time according to a stochastic process equation. By making explicit assumptions on the functional form of target state dynamics, Bayesian estimation techniques may be applied, resulting in optimal or nearly optimal target state estimators.

The workhorse for state estimation is the discrete Kalman filter. The Kalman filter sequentially estimates the target state as the minimum mean squared error estimate (MMSE) of the posterior distribution, assuming linear and Gaussian dynamic and measurement models [29]. Derivations of the Kalman filter, along with the resulting equations, are widely available [3]. The discrete Kalman filtering equations are as follows. Given a set of state dynamic and measurement equations

$$\mathbf{x}(k) = \mathbf{F}(k-1)\mathbf{x}(k-1) + \mathbf{v}(k-1), \tag{14}$$

$$\mathbf{z}(k) = \mathbf{H}(k)\mathbf{x}(k) + \mathbf{w}(k), \tag{15}$$

where

$\mathbf{x}(k) =$ unknown state vector at time index $k$,

$\mathbf{F}(k) =$ known linear state update equations at time index $k$,

$\mathbf{v}(k) =$ zero-mean Gaussian random vector with known $\mathrm{E}[\mathbf{v}(k)\mathbf{v}(k)^T]$=$\mathbf{Q}(k)$,

$\mathbf{z}(k) =$ measured data at time index k,

$\mathbf{H}(k) =$ known measurement equations,

$\mathbf{w}(k) =$ zero-mean Gaussian random vector with known $\mathrm{E}[\mathbf{w}(k)\mathbf{w}(k)^T]$=$\mathbf{R}(k)$,

and initial conditions $\hat{\mathbf{x}}(0|0)$ with $\mathrm{E}\left[\hat{\mathbf{x}}(0|0)\hat{\mathbf{x}}(0|0)^T\right]$=$\mathbf{P}(0|0)$, then the sequential Kalman update equations can be expressed in terms of a prediction step followed by an update step. The prediction step is given by[3]

$$\hat{\mathbf{x}}(k+1|k) = \mathbf{F}(k)\hat{\mathbf{x}}(k|k), \tag{16}$$

$$\mathbf{P}(k+1|k) = \mathbf{F}(k)\mathbf{P}(k|k)\mathbf{F}(k)^T + \mathbf{Q}(k), \tag{17}$$

and the update step is given by

$$\hat{\mathbf{x}}(k+1|k+1) = \hat{\mathbf{x}}(k+1|k) + \mathbf{W}(k+1)\left(\mathbf{z}(k+1) - \mathbf{H}(k+1)\hat{\mathbf{x}}(k+1|k)\right), \tag{18}$$

$$\mathbf{P}(k+1|k+1) = \left[\mathbf{I} - \mathbf{W}(k+1)\mathbf{H}(k+1)\right]\mathbf{P}(k+1|k), \tag{19}$$

where $\mathbf{W}(k+1)$ is the Kalman gain matrix

$$\mathbf{W}(k+1) = \mathbf{P}(k+1|k)\mathbf{H}(k+1)^T\left(\mathbf{S}(k+1)\right)^{-1}, \tag{20}$$

and $\mathbf{S}(k+1)$ is the measurement residual covariance

$$\mathbf{S}(k+1) = \mathbf{H}(k+1)\mathbf{P}(k+1|k)\mathbf{H}(k+1)^T + \mathbf{R}(k+1). \tag{21}$$

---

[3] A control input can also be included in (14), which would result in slightly different Kalman prediction and update equations. A common example is gravity, which can be seen as a nearly constant acceleration. However, in this work no control inputs are used, so this is led out of the discussion.

One of the main advantages of state estimation is the ability to estimate higher-order dynamic parameters that are not directly observable in the measurement space. For example, radars typically cannot directly measure the acceleration of an object, yet state estimation techniques provide a straightforward methodology to estimate it.

In practice, the $\mathbf{H}(k)$ and $\mathbf{R}(k)$ are predetermined by the sensor and its characterized accuracy levels. However, the selection of state dynamic equations $\mathbf{F}(k)$ and process noise covariance $\mathbf{Q}(k)$ are often challenging design choices that depend upon the expected types of targets. The simplest state dynamic model in the literature is the nearly constant velocity (NCV) model, which is given in continuous time as

$$\ddot{x}(t) = \tilde{w}(t), \tag{22}$$

where $\ddot{x}(t)$ denotes the scalar acceleration of a target, $\tilde{w}(t)$ is zero-mean white noise with

$$E[\tilde{w}(t)\tilde{w}(\tau)] = q\delta(t-\tau), \tag{23}$$

and $\delta(t-\tau)$ is the Dirac delta function. Using standard state-space discretization methods, a discrete time representation of the NCV model becomes

$$\begin{bmatrix} x(k) \\ \dot{x}(k) \end{bmatrix} = \begin{bmatrix} 1 & \Delta t \\ 0 & 1 \end{bmatrix} \begin{bmatrix} x(k-1) \\ \dot{x}(k-1) \end{bmatrix} + \mathbf{v}(k-1), \tag{24}$$

where $\mathbf{v}(k-1)$ is a zero mean Gaussian random vector with covariance matrix

$$\mathbf{Q}(k-1) = q \begin{bmatrix} \frac{\Delta t^3}{3} & \frac{\Delta t^2}{2} \\ \frac{\Delta t^2}{2} & \Delta t \end{bmatrix}. \tag{25}$$

Any deviations in constant-velocity motion is captured by the power spectral density, $q$. Assuming process noise as additive white noise as in (22) followed by state-space discretization is referred to as the continuous white noise (CWN) acceleration model. Another approach to model acceleration errors is the discrete white noise (DWN) acceleration model, where $\mathbf{v}(k-1)$ in (24) is a scalar-valued zero-mean white sequence $v(k-1)$ with

$$E[v(k)v(j)] = \sigma_a^2\delta_{kj}, \tag{26}$$

where $\delta_{kj} = 1$ for $k = j$ and zero elsewhere. In other words, the deviations from modeled dynamics are unknown, but are assumed constant in magnitude throughout the sampling interval and uncorrelated with the next sampling interval. Consequently, the selection of $\sigma_a^2$ is only valid for the specific sampling interval. For (24), the zero-mean white sequence has units of acceleration and the model can be rewritten as

$$\begin{bmatrix} x(k) \\ \dot{x}(k) \end{bmatrix} = \begin{bmatrix} 1 & \Delta t \\ 0 & 1 \end{bmatrix} \begin{bmatrix} x(k-1) \\ \dot{x}(k-1) \end{bmatrix} + \begin{bmatrix} \frac{\Delta t^2}{2} \\ \Delta t \end{bmatrix} v(k-1). \tag{27}$$

As discussed in [3], the DWN process noise model is more appropriate for constant revisit rate, but the CWN process noise model is more appropriate for a variable revisit rate.

In many practical applications of state estimation, the measurement and/or dynamical equations are nonlinear and cannot be represented by simple matrices (i.e., $\mathbf{H}(k)$ and $\mathbf{F}(k)$). For example, many radar measure targets in range-angle space as described in Chapter 2.1, but target state estimates are maintained in a coordinate system in which target state dynamical models are derived (i.e., a Cartesian coordinates). Therefore, the transformation from state space to measurement space is nonlinear and the standard Kalman filtering equations do not apply. The remedy in [2] uses an $n$th-order approximation of the Taylor series expansion of the nonlinear measurement or state dynamic equations. In practice, a first-order approximation is common, in which the nonlinear measurement equations and/or state dynamic equations are replaced by their Jacobians matrices in (17), (19), (20), and (21).

### 2.2.2 Multiple Model Approaches

The motion of many practical targets can be characterized by a family of kinematic models, as illustrated in Figure 4. In the figure, the solid line represents straight and level flight with constant velocity motion and the dotted line represents a turn. An appropriate kinematic model for straight-and-level flight might be the nearly constant velocity (NCV) model, whereas an appropriate model for a coordinated turn might be a horizontal nearly coordinated turn (HNCT) model (described in detail in Chapter 5.2.1.2). Instead of modeling target motion with a single kinematic model, target motion can be explicitly assumed

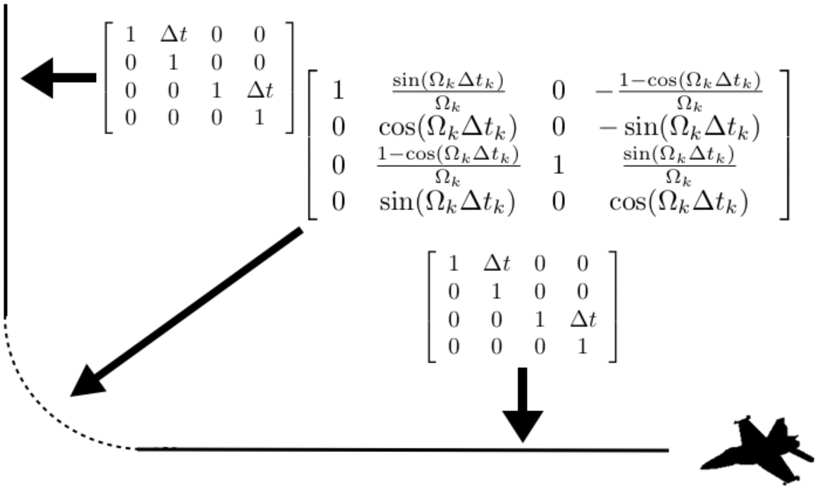

Figure 4: Illustration of target motion. Solid line represents constant velocity motion and dotted line represents turning motion. Matrices contain appropriate state update equations for the respective kinematics.

as having a set of possible modes, and at each measurement update, the target dynamics follow one of the modes. Under these assumptions, the dynamical equations of (14) can be rewritten as

$$\mathbf{x}(k) = \mathbf{F}(k-1, \theta(k-1))\mathbf{x}(k-1) + \mathbf{v}(k-1, \theta(k-1)), \tag{28}$$

where $\theta(k-1)$ is an index to one out of $r$ possible modes. Furthermore, assume $\theta(k)$ is a finite state Markov process with the probability of transitioning to mode $j$ given the target is in mode $i$ denoted as

$$p_{ij} = Pr\left\{\theta(k) = j | \theta(k-1) = i\right\}, \quad i, j = 1, ...r. \tag{29}$$

Under this framework, an optimal approach would consider every possible sequence of modes from the initial measurement to the final measurement. This cannot be implemented in a practical tracking system due to computational complexity. Therefore several suboptimal approaches are suggested in the literature. The IMM estimator from [14] is generally accepted to be the superior tracking algorithm among all multiple model approaches when computational aspects are considered [3]. The IMM algorithm results in a sequential state estimation process using a parallel set of discrete Kalman filters that interact through a process called "mixing." An iteration through the IMM algorithm is as follows. Along with initial conditions for the individual Kalman filters, assume initial set of mode probabilities $\mu_i(0)$ for each mode $i$ and a set of Markov transition probabilities. Denoting $\hat{\mathbf{x}}^j(k-1|k-1)$ as the Kalman update of mode $j$ at time $(k-1)$, the "mixed" means and covariances are given as

$$\hat{\mathbf{x}}^{0j}(k-1|k-1) = \sum_{i=1}^{r} \mu_{i|j}(k-1|k-1)\hat{\mathbf{x}}^{i}(k-1|k-1), \tag{30}$$

$$\mathbf{P}^{0j}(k-1|k-1) = \sum_{i=1}^{r} \mu_{i|j}(k-1|k-1)\left[\mathbf{P}^{i}(k-1|k-1) + \tilde{\mathbf{P}}^{i}(k-1|k-1)\right] \tag{31}$$

for $j = 1, ..., r$, where the mixing probabilities are computed as

$$\mu_{i|j}(k-1|k-1) = \frac{1}{\bar{c}_j} p_{i,j}\mu_i(k-1), \qquad i, j = 1, ....r, \tag{32}$$

with normalizing constant

$$\bar{c}_j = \sum_{i=1}^{r} p_{ij}\mu_i(k-1) \quad j = 1, ...., r, \tag{33}$$

and $\mu_i(k-1)$ is the probability that mode $i$ is the correct mode at time index $(k-1)$. The $\tilde{\mathbf{P}}^i(k-1|k-1)$ in (31) is a "spread-of-the-means" term

$$\begin{aligned}\tilde{\mathbf{P}}^{i}(k-1|k-1) = &\left[\hat{\mathbf{x}}^{i}(k-1|k-1) - \hat{\mathbf{x}}^{0j}(k-1|k-1)\right] \times \\ &\left[\hat{\mathbf{x}}^{i}(k-1|k-1) - \hat{\mathbf{x}}^{0j}(k-1|k-1)\right]^{T}.\end{aligned} \tag{34}$$

The mixed states and covariances of (30) and (31) are used as the inputs to the Kalman filtering prediction steps of (16)-(17) to provide $\hat{\mathbf{x}}^{0j}(k|k-1)$ and $\mathbf{P}^{0j}(k|k-1)$, and further used in the update steps of (18)-(19) to yield $\hat{\mathbf{x}}^{j}(k|k)$ and $\mathbf{P}^{j}(k|k)$. Measurement likelihoods, computed as

$$\Lambda_j(k) = \mathscr{N}\left(\mathbf{z}(k); \hat{\mathbf{z}}^j, \mathbf{S}^j\right), \tag{35}$$

where $\mathscr{N}(\mathbf{a}; \mathbf{b}, \mathbf{C})$ denotes the Gaussian distribution with mean $\mathbf{b}$ and covariance $\mathbf{C}$ evaluated at $\mathbf{a}$, with

$$\hat{\mathbf{z}}^j = H(k)\hat{\mathbf{x}}^{0j}(k|k-1) \tag{36}$$

$$\mathbf{S}^j = \mathbf{H}(k+1)\mathbf{P}^{0j}(k+1|k)\mathbf{H}(k+1)^T + \mathbf{R}(k+1), \tag{37}$$

are used to update the mode probabilities of the IMM filter,

$$\mu_j(k) = \frac{1}{c}\Lambda_j(k)\bar{c}_j \quad j = 1, ..., r, \tag{38}$$

where $\bar{c}_j$ is given by (33) and

$$c = \sum_{j=1}^{r} \Lambda_j(k)\bar{c}_j. \tag{39}$$

Notice the fundamental quantities that determine mode probability updates are the Markov transition probabilities and measurement likelihoods. Often in practice, measurement likelihoods dominate over the Markov transition probabilities, so the mode distinguishing capabilities of the IMM are driven through observed measurement likelihoods.

An often overlooked aspect of multiple model approaches is the implementation of a set of models with differing state dimension. For example, a 2D NCV model will have a state dimension of four, whereas a 2D HNCT model will typically have an extra dimension for the unknown turn rate. Strong theoretical support for such a case is lacking, as briefly mentioned in [41]. In fact, the derivation of the IMM estimator assumes the state dimension of all modes are equal [3]. For the case of an IMM estimator with models of differing state dimension, issues arise during the mixing phase. The standard approach of augmenting extra elements with zeros introduces a bias in the mixed estimate [4]. Recently, an unbiased mixing approach has been suggested for the case of an IMM estimator with two modes to predict the impact point of ballistic missiles [55]. In Chapter 5, this is extended to three modes.

### 2.2.3 Radar Resource Management

Traditional track-while-scan radars use mechanically rotated antennas, rotated at a constant rate, to scan for new targets, while simultaneously performing track maintenance on existing targets. As a consequence, most radar tracking literature assumes measurements are provided to state estimation techniques at a near constant rate. With the advent of phased array technology, agile beam radars can quickly switch the direction of a radar beam without any mechanical steering. Therefore, with agile beam radars, track maintenance dwells are not constrained to a near constant revisit period. Along with the advent of agile-beam tracking radars, the problem of optimal track maintenance scheduling appeared in the literature beginning with the work of Van Keuk and Blackman in [48]. Typical approaches for the radar scheduling problem, as in [48], suggest scheduling track maintenance dwells when a predicted track covariance (as in from (17) from the discrete Kalman filter) grows to occupy a specified fraction of the main beam in angle space, as illustrated in Figure 5.

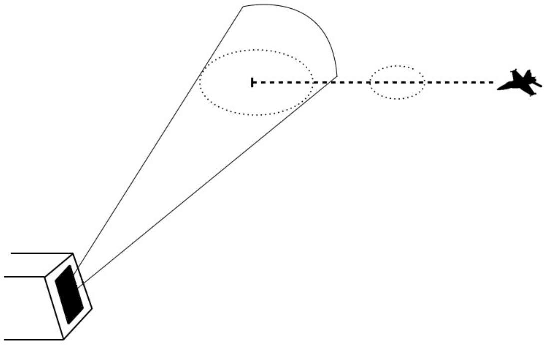

Figure 5: Illustration of adaptive revisit time calculations for an agile beam radar.

Along with agile beam systems, modern radars are able to select from multiple waveforms such that waveform energy may be coordinated with the tracking algorithm. With a target strength in hand, a reasonable criterion for selection of a radar waveform is a desired return signal strength. In general, a higher energy waveform results in higher probability of detection and higher measurement accuracy, thus more accurate state estimation and lower total number of required track maintenance dwells. However, high energy waveforms cost more energy. Therefore, a tradeoff exists between radar time and energy in the selection of a radar waveform and overall operating SNR.

In [48], the authors show that an operating point of 16 dB is an optimal tracking level minimizing radar load for an individual track. Radar load, as defined in [48], is the multiplication of total energy times the total number of track maintenance dwells. Blair proposed the tracking Benchmark problems described in [12] and [13] for addressing the issue of optimal track maintenance scheduling algorithms. The Benchmark problem included a Monte Carlo simulation that all algorithm developers could use as a means of comparison. In [12], the goal of developers was to minimize the total number of track dwells while maintaining a maximum allowed track loss percentage. In [13], the primary measure of tracking performance was a weighted sum of the average radar energy per second and the average radar time per second. Although the Benchmark problems in [12] and [13] considered maneuvering targets, a nominal tracking SNR was not part of the optimization in published solutions. In fact, the impact of maneuvering targets on a nominal tracking SNR has not been previously reported in the literature.

# CHAPTER III

# TARGET DETECTION

Detection of the presence of one or more targets is one of the most fundamental purposes of a surveillance radar. Improvements in detection performance, often the result of sensitivity gains, are valued since they result in more reliable localization of targets. However, sensitivity gains in the form of more powerful antennas, more bandwidth, or faster analog-to-digital converters may not be cost effective or even possible. Processing gains that do not require additional, possibly expensive, hardware are welcome additions to the design of a surveillance radar system. In this chapter, improvement in detection performance is pursued through alternative detection processing of near-Nyquist sampled signals.

Traditional radar detectors compare the observed signal-to-noise ratio (SNR) at samples of the output of the matched filter to a threshold. Threshold values are typically set to achieve a specified probability of false alarm, usually low in most radar applications, around $10^{-3}$ to $10^{-5}$ [39]. Since sample rates used in practice often result in two or more adjacent samples in the main lobe of the matched filter response, traditional radar detection ignores a key piece of information - the correlation between samples.

Since the location of a target in range is usually not known a-priori, matched filter samples are not guaranteed to occur at the maximum of the matched filter response. In the radar literature, this is called range bin straddling, bin splitting, or bin spacing loss and is treated, like many other losses, as a loss in voltage or power. However, since probability of detection is a nonlinear function of observed SNR, bin straddling loss should actually be described in terms of the loss in probability of detection, as described by Cann in [17]. Using Swerling 0 and Swerling 1 target models, Cann shows that although the average loss in power is around 2.5 dB, the average loss in terms of probability of detection can be as high as 4 dB. When Cann moved from contiguous range bins to 50% overlapped range bins, the loss was smaller and reliably predicted with the actual loss in power. Xie further refines the work of [17] by proposing a more accurate predictor for probability of detection assuming a Swerling 0 target, a single pulse, and 50% overlapped range bins [54]. Although the authors in [17] and [54] use the correlation between range bins to refine a probability of detection estimate for a traditional detection scheme, they do not propose using the correlation between range bins in the actual detection process.

Using an explicit model of adjacent matched filter samples of the sum channel of a monopulse system and the functional form of the matched filter response, the average loglikelihood ratio test (ALLRT), which includes the correlation between matched filter samples, is derived below. Key features relevant to the design of a detector are illustrated via simulations. In particular, performance comparisons of the ALLRT detector with traditional radar signal detectors using various sample rates is provided. Large portions of this Chapter follow our work described in [25].

## *3.1 Signal and Target Modeling*

Following the assumptions described in Section 2.1, samples of the sum channel signal can be expressed as

$$s(b) = xr(b\Delta t - \tau) + n(b), \tag{40}$$

where $x$ is a zero mean Gaussian random variable with variance equal to $\beta^2$. Note that a single pulse corresponds to two independent and identically distributed (i.i.d.) observations of (40). Therefore, the total number of i.i.d. observations is equal to $2N$, where $N$ is the total number of pulses. Denote the $l$th i.i.d. observation vector as

$$\mathbf{s}_l = \left[s_l(1)...s_l(B)\right], \qquad 1 \leq l \leq 2N, \tag{41}$$

where $B$ is the total number of matched filter samples in the range window. Denoting $\sigma^2$ as the variance of the noise in each matched filter sample, (41) forms a zero-mean Gaussian random vector with correlation matrix $\mathbf{K}$ having elements

$$E[s_l(i)s_l(j)] = \beta^2 r(i\Delta t - \tau)r(j\Delta t - \tau) + \sigma^2 r((i-j)\Delta t), \tag{42}$$

where $E[.]$ denotes expected value.

For the rest of this chapter, $\tau$ and $\beta^2$ are treated as unknown parameters and $\sigma^2$ is treated as a known parameter. However, note that the exact value of $\sigma^2$ is irrelevant; detectors can be designed independent of the actual noise power since the test statistic is often a signal-to-noise ratio. As discussed in Chapter 2.1, the selection of a sample rate determines the magnitude of noise correlation across adjacent samples, which arises from the matched filtering process.

As discussed in [17], signal-plus-noise fluctuations are almost entirely due to target fluctuations for Swerling 1 and 2 targets, and are therefore highly correlated in adjacent samples. The contribution of the second sample to total detection performance is small (i.e. if a target is detected in the first sample, it is likely to also be detected in the second sample) [17]. This correlation is written explicitly in (42), where a sample rate greater than or equal to the Rayleigh resolution gives a correlation greater than or equal to zero that increases with $\beta^2$. Therefore, using the observed correlation between matched filter samples may aid in the detection process, providing a motivating factor for this work.

### 3.1.1 Signal Model for Region Under Test

Traditional radar detection compares observed signal strength in a matched filter sample under test to a threshold. Often a Neyman-Pearson approach is taken such that a detection threshold achieves a desired $P_{fa}$ for that sample, where $P_{fa}$ denotes the probability of a false alarm. If the threshold value for samples collected at Rayleigh resolution is used for samples collected at a higher sample rate, then the $P_{fa}$ across a given range window, or region under test, is not generally equal. This is problematic for comparison of detection tests over a specified window. For fair comparison of detection performance, $P_{fa}$ for a given region under test should be equal for detectors being analyzed. In this work, the region under test is defined as Rayleigh resolution of the transmitted waveform, denoted as $\Delta t_r$. Furthermore, a detection test is the determination of target presence in this region under test, where only matched filter samples (and possibly their correlations) in the region under test are considered applicable for detection. For waveforms sampled at the Rayleigh resolution, two matched filter samples are included in the region under test as shown in

Figure 6a. Similarly, waveforms sampled at the Rayleigh resolution divided by two result in three matched filter samples in the region under test (four samples with target energy), as shown in Figure 6b.

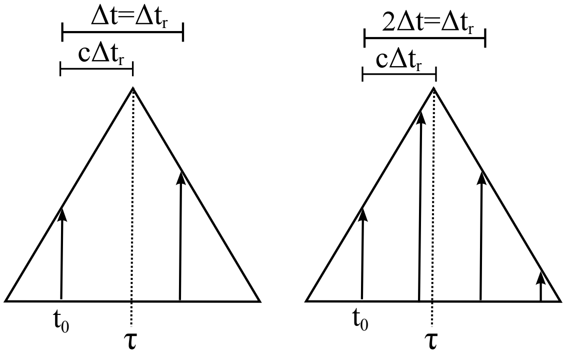

(a) Sample period equal to Rayleigh resolution

(b) Sample period equal to half Rayleigh resolution

Figure 6: Sampling the output of the matched filter in the region under test. The region under test has size equal to the Rayleigh resolution of transmitted waveform.

Defining the matched filter response with time axis normalized by the Rayleigh resolution as

$$q(x) = r(x\Delta t_r), \tag{43}$$

the location of the first sample in the region under test as $t_0$, and the sub-Rayleigh resolution location of the target in the region under test as

$$c = \frac{\tau - t_0}{\Delta t_r}, \tag{44}$$

allows for (40) to be expressed in a more useful form for the region under test. Note that $c \in [0, 1]$ and is also unknown since $\tau$ is treated as an unknown parameter. Assuming $U$ samples in the region under test, with exactly two samples on the edges, (40) can be expressed as

$$s(u) = xq\left(c - \frac{u}{U-1}\right) + n(u), \tag{45}$$

where $u = [0, ..., U-1]^T$. Then (45) forms a zero-mean $U$-dimensional Gaussian random vector with correlation matrix $\mathbf{K}$, with elements

$$E[s_l(u)s_l(v)] = \beta^2 q\left(c - \frac{u}{U-1}\right) q\left(c - \frac{v}{U-1}\right) + \sigma^2 q\left(\frac{u-v}{U-1}\right), \tag{46}$$

where $v = [0, ..., U - 1]^T$. Since the matched filter samples form a zero-mean Gaussian random vector, (46) defines the distribution of observations under the hypothesis of target presence. The distribution used for the hypothesis of no target present is simply (46) with $\beta^2 = 0$ (which implies $x = 0$ in (45)).

### 3.1.2 Special Case: Rectangular Waveform and Rayleigh Sampling

For a transmitted rectangular waveform, the time scaled matched filter response is the triangle function

$$q_T(x) = \begin{cases} 1 - |x|, & \text{if } |x| < 1 \\ 0 & \text{otherwise.} \end{cases} \tag{47}$$

Although rectangular waveforms are not practical because of infinite bandwidth, using a triangular matched filter response to model bin straddling has appeared several times in recent literature (for examples see [15, 44, 45, 53, 56, 57]). With a sample rate equal to $\Delta t_r$, two samples are in the region under test and the signal model becomes

$$s(0) = xq_T(c) + n(0), \tag{48}$$

$$s(1) = xq_T(c-1) + n(1), \tag{49}$$

with correlation matrix

$$\mathbf{K} = \begin{bmatrix} \beta^2 q_T(c)^2 + \sigma^2 & \beta^2 q_T(c) q_T(c-1) \\ \beta^2 q_T(c) q_T(c-1) & \beta^2 q_T(c-1)^2 + \sigma^2 \end{bmatrix}. \tag{50}$$

Recalling $c \in [0, 1]$, analytic evaluation of the triangle function gives

$$\mathbf{K} = \begin{bmatrix} \beta^2 (1-c)^2 + \sigma^2 & \beta^2 c(1-c) \\ \beta^2 c(1-c) & \beta^2 c^2 + \sigma^2 \end{bmatrix}. \tag{51}$$

As a reminder, $c$ and $\beta^2$ in (51) are treated as unknown parameters in this study.

## *3.2 Detection Analysis*

In this section, test statistics for traditional detection and the newly proposed ALLRT detector are provided, and performance comparisons are made using numerical simulations.

The simulations used in this study generated in-phase and quadrature matched filter samples in a region under test according to (8) and (9) for a given $\mathfrak{R}_r$, matched filter response, number of pulses, and target location within the region under test. Recall that noise in (8) and (9) can be correlated, with magnitude of correlation depending upon the matched filter response along with sample rate. The simulations accounted for this correlation. In this section, metrics computed by the simulation are discussed in detail, along with relevance to practical systems. Finally, the optimal number of pulses given $\mathfrak{R}_t$ is investigated.

### 3.2.1 Test Statistics

Traditional radar detection compares the observed SNR in a given range bin to a detection threshold. In terms of the signal model described by (45) and (46), the average observed SNR for matched filter sample $u$ is defined as

$$\mathfrak{R}_o(u) = \frac{1}{2N\sigma^2} \sum_{l=1}^{2N} s_l(u)^2, \tag{52}$$

where $N$ is the total number of pulses.[1] Note that $\mathfrak{R}_o$ is treated as a random variable, whereas $\mathfrak{R}_r$ and $\mathfrak{R}_t$ are treated as unknown parameters. As discussed in Section 3.1.1, the region under test is defined as the distance across adjacent matched filter samples of size equal to the Rayleigh resolution of the transmitted waveform. Sampling at a rate higher than the Rayleigh resolution corresponds to three or more matched filter samples in the region under test. In traditional radar approaches, a detection is reported if any matched filter sample in the region under test exceeds a detection threshold. This is equivalent to comparing the maximum $\mathfrak{R}_o$ in the region under test to a threshold

$$\max\left([\mathfrak{R}_o(0), ..., \mathfrak{R}_o(U-1)]\right) \quad \underset{H_0}{\overset{H_1}{\gtrless}} \gamma, \tag{53}$$

where $\gamma$ denotes the detection threshold and $U$ is the total number of samples in the region under test.

In Appendix A, the average loglikelihood ratio test (ALLRT) is derived for a sample rate equal to the Rayleigh resolution of the transmitted waveform. The derivation shows that

---

[1] $\mathfrak{R}_o$ is actually a signal-plus-noise-to-noise-ratio as described in [7], but it will be referred to as a signal-to-noise-ratio to be consistent with previous literature.

the test statistic in the loglikelihood ratio test (LLRT) involves the unknown $c$. To handle the unknown $c$, a uniform distribution between zero and one is assumed and integrated through the LLRT, thus providing the *average* loglikelihood ratio test. Defining the observed correlation between matched filter samples as

$$\mathfrak{C}_o = \frac{1}{2N\sigma^2} \sum_{l=1}^{2N} s_l(0) s_l(1), \tag{54}$$

the ALLRT detector can be expressed as

$$a_1 \left( \mathfrak{R}_o(0) + \mathfrak{R}_o(1) \right) + a_2 \mathfrak{C}_o \quad \underset{H_0}{\overset{H_1}{\gtrless}} \gamma_a, \tag{55}$$

where $a_1$ and $a_2$ depend upon the matched filter response of the transmitted waveform, and $\gamma_a$ denotes the ALLRT threshold. As discussed in Appendix A, the ALLRT detector incorporates the functional form of the matched filter response across multiple matched filter samples. Thus, a new avenue of waveform design in terms of matched filter response is discussed in Appendix A.

Assuming pulse-to-pulse fluctuations in target amplitude (i.e., a Swerling 2 target), detection performance of three detectors is compared. First, the traditional detector is defined as the threshold test given by (53), with a sample rate equal to the Rayleigh resolution given as

$$\max \left( [\mathfrak{R}_o(0),\ \mathfrak{R}_o(1)] \right) \quad \underset{H_0}{\overset{H_1}{\gtrless}} \gamma_t. \tag{56}$$

The second detector is the ALLRT detector given by (55) with a sample rate also equal to the Rayleigh resolution. The third detector, denoted as the oversample detector, is the threshold test given by (53) with $U = 3$, corresponding to double the sample rate of the traditional and ALLRT detectors,

$$\max \left( [\mathfrak{R}_o(0),\ \mathfrak{R}_o(1),\ \mathfrak{R}_o(2)] \right) \quad \underset{H_0}{\overset{H_1}{\gtrless}} \gamma_o. \tag{57}$$

These three detectors are compared using matched filter responses of a triangle function and a sinc function. The triangle matched filter response is similar to the main lobe of a phase coded waveform, and a sinc matched filter response is similar to that of an LFM waveform, both of which are pulse compression waveforms commonly used in practice. The triangle matched filter response, $q_T(x)$, is given by (47), and the sinc matched filter response, $q_S(x)$, is given by (153) in the Appendix. Since $q_S(x) > q_T(x)$ for $x \in [0, 1]$, detection performance using the sinc matched filter response is expected to outperform the triangle matched filter response.

In many radar tracking applications, Neyman-Pearson detectors are used for target detection. These methods choose a detection threshold that achieves a $P_{fa}$ deemed acceptable to the radar system. The desired $P_{fa}$ may even be coordinated with advanced data association and tracking algorithms for some surveillance radar systems [4]. Threshold values can be found by analytic derivation of the cumulative density function of the test statistic under the null hypothesis, or with numerical approaches.

Under the hypothesis of a target not present, (53) is the maximum of $U$ Erlang distributed random variables that may have correlation between matched filter samples and (55) is a distribution of quadratic forms. Detailed study of these density functions, which become even more complicated for the hypothesis of target presence, will be left for future research. Since the main interest is investigation of detection performance, Neyman-Pearson detection thresholds for the three detectors were found using numerical simulations for $P_{fa}$ values of $10^{-3}$, $10^{-4}$, and $10^{-5}$, and the number of pulses ranging from one to ten. For each Neyman-Pearson threshold calculation, $3000/P_{fa}$ random samples of (55), (56), and (57) were generated under the hypothesis of no target present, and thresholds were found that satisfy the desired $P_{fa}$.

Notice from (46) that under the hypothesis of a target not present, the correlation of noise across samples depends upon the matched filter response of the transmitted waveform. This means that in general, the Neyman-Pearson detector depends upon the functional form of the transmitted waveform. However, sample rates equal to the Rayleigh resolution result in $q\left(\frac{u-v}{U-1}\right) = 0$ in (46), which implies there is no correlation between adjacent noise samples and that thresholds are independent of the transmitted waveform.

### 3.2.2 Discussion of Metrics

Since the statistical distribution of matched filter samples under the hypothesis of target presence depends upon the location of the target, $P_d$ (probability of detection) also depends upon the location of the target as illustrated in Figures 7, 8, and 9.

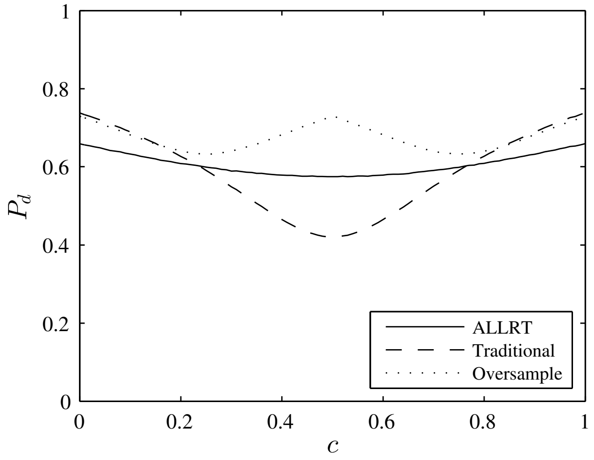

(a) Triangle matched filter response

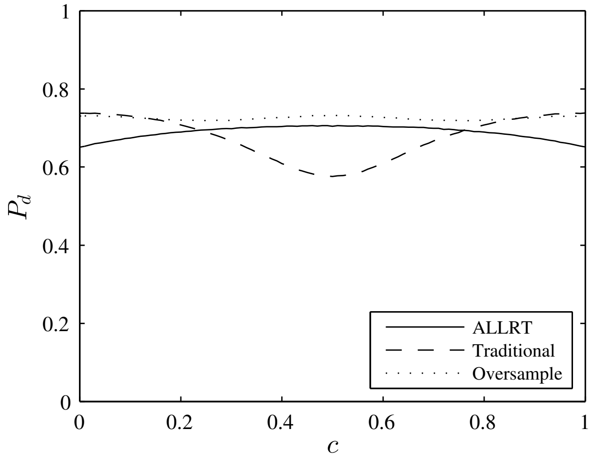

(b) Sinc matched filter response

Figure 7: $P_d$ for various target locations in the region under test for a single pulse with $P_{fa} = 10^{-4}$ and $\Re_t = 15$ dB. For the traditional and ALLRT detectors, matched filter samples occur at 0 and 1 in the region under test, and for the oversample detector, samples occur at 0, 0.5, and 1.

Each figure provides an illustration of $P_d$ for the three detectors discussed above for a given location in the region under test using both triangle and sinc matched filter responses. In each case, $P_{fa} = 10^{-4}$. First notice that for the traditional detector, $P_d$ is minimized

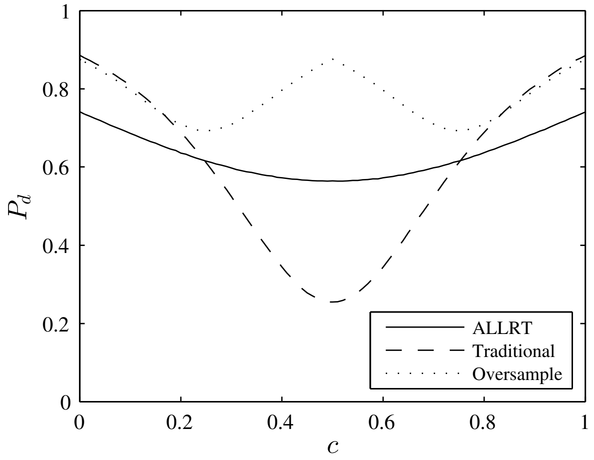

(a) Triangle matched filter response

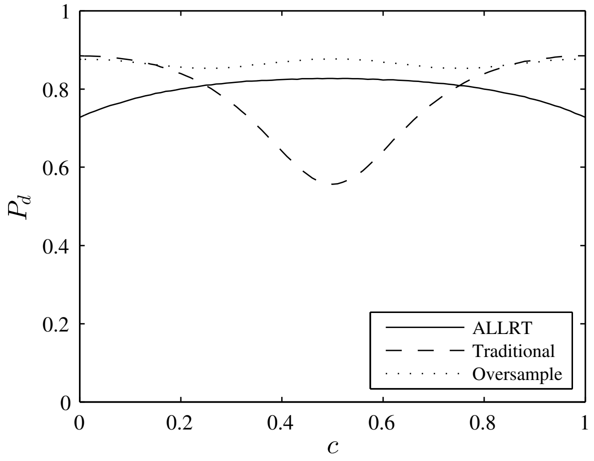

(b) Sinc matched filter response

Figure 8: $P_d$ for various target locations in the region under test for five pulses with $P_{fa} = 10^{-4}$ and $\Re_t = 15$ dB. For the traditional and ALLRT detectors, matched filter samples occur at 0 and 1 in the region under test, and for the oversample detector, samples occur at 0, 0.5, and 1.

when a target is centered between samples and maximized when a target is located directly on a sample. For a single pulse, the difference between the maximum and minimum $P_d$ for the traditional detector using a triangle matched filter response is around 0.3 and gets worse with increasing number of pulses to around 0.8 for ten pulses. Second, notice that the difference in the maximum and minimum $P_d$ is less distinctive for the sinc matched filter response as compared to the triangle matched filter response. These general trends hold for the ALLRT and oversample detectors, but appear less distinctive. However, notice that for

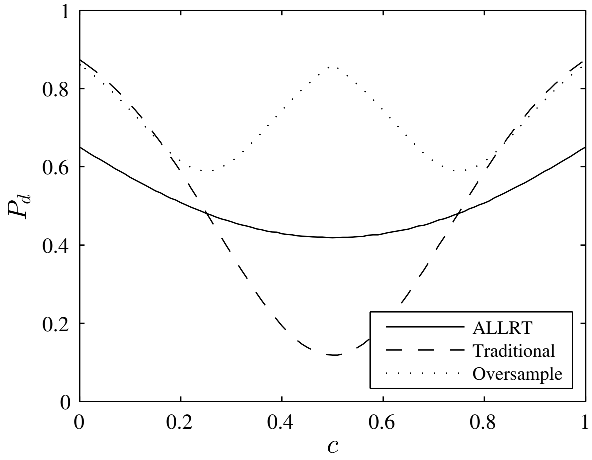

(a) Triangle matched filter response

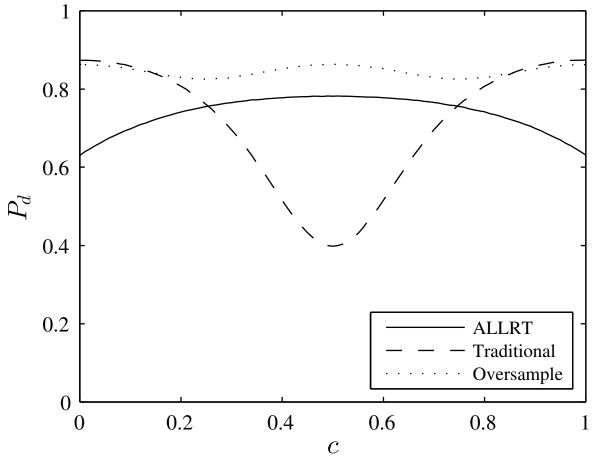

(b) Sinc matched filter response

Figure 9: $P_d$ for various target locations in the region under test for ten pulses with $P_{fa} = 10^{-4}$ and $\Re_t = 15$ dB. For the traditional and ALLRT detectors, matched filter samples occur at 0 and 1 in the region under test, and for the oversample detector, samples occur at 0, 0.5, and 1.

the ALLRT detector using a sinc matched filter response, $P_d$ is maximized when a target is centered between samples and minimized when a target is directly located on a sample, opposite to the traditional and oversample detectors. Assuming the target location within a region under test is not reliably known *a priori*, the following questions arise in the design of a practical surveillance radar detector:

- What is the maximum loss in $P_d$ due to range straddling?
- Given a target SNR estimate, how much increase in transmitted signal strength is

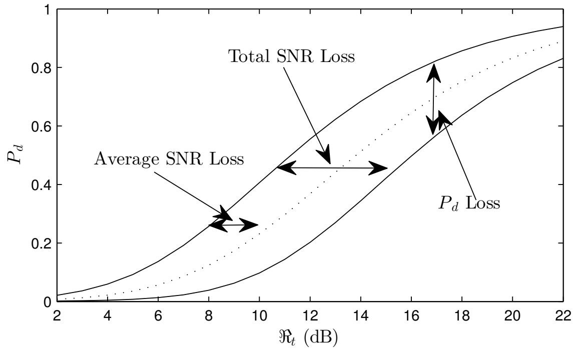

Figure 10: $P_d$ as a function of $\Re_t$ using traditional detector with $P_{fa} = 10^{-4}$, a single pulse, and a triangular matched filter response. Top solid line represents maximum $P_d$, and the bottom solid line represents minimum $P_d$. Dotted line represents detection performance on average, assuming a target is uniformly distributed in the region under test.

needed to guarantee a specified $P_d$?

Detection metrics proposed in this chapter measure performance losses due to the unknown location of a target, as illustrated in Figure 10. $P_d$ loss is defined as the difference between maximum $P_d$ and minimum $P_d$ for a given $\Re_t$ as seen in Figure 10. The $P_d$ loss metric is relevant since it quantifies the worst case $P_d$ loss due to unknown range bin straddling for a given target SNR. Predicted $P_d$'s are used in sophisticated data association and tracking algorithms, for example multiple hypothesis tracking [5] and the probabilistic data association filter [4], emphasizing the importance of a reliably predicted $P_d$. Therefore, inconsistent $P_d$ estimates can have negative effects on overall tracking performance. Total SNR loss is defined as the difference between $\Re_t$ for the maximum $P_d$ and minimum $P_d$. Total SNR loss is relevant since it quantifies the increase in $\Re_t$ needed to ensure a given $P_d$. Note that $\Re_t$ is related to waveform energy (proportional to pulse width) through matched filter gain in (3). For a single pulse, a 3 dB increase in $\Re_t$ is nearly equivalent to doubling the pulsewidth (i.e., increasing waveform energy by a factor of two). Average SNR loss, defined as the difference between target SNR for the maximum $P_d$ and the average $P_d$ (assuming a target is uniformly distributed in the region under test), has appeared in recent literature [17]. In [17], Cann emphasized that the SNR gain required to achieve a specified $P_d$ was more important than the actual loss in SNR that arises due to bin straddling, and thus defined average SNR loss as in Figure 10. This metric is included to facilitate comparison

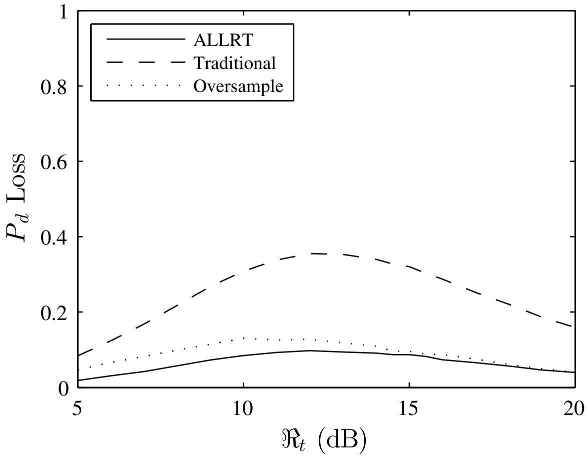

(a) Triangle matched filter response

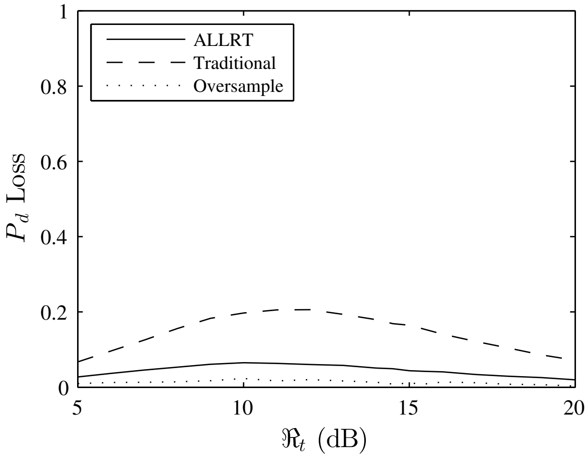

(b) Sinc matched filter response

Figure 11: $P_d$ loss for three detectors with $P_{fa} = 10^{-4}$ and a single pulse.

with the results of Cann's paper.

### 3.2.3 Performance Comparison

The metrics discussed in Section 3.2.2 are calculated using numerical simulations. $P_d$ loss for the three detectors using a single pulse with triangle and sinc matched filter responses are provided in Figure 11. $P_d$ loss for five pulses and ten pulses are shown in Figures 12 and 13, respectively. As shown in Figure 11, $P_d$ loss for the traditional detector using a triangle matched filter response is maximized at around 0.4 near $\Re_t = 12$ dB. Notice that $P_d$ loss using the traditional detector becomes more distinguished with more pulses, increasing to nearly 0.8 for ten pulses using the triangular matched filter response as shown in Figure

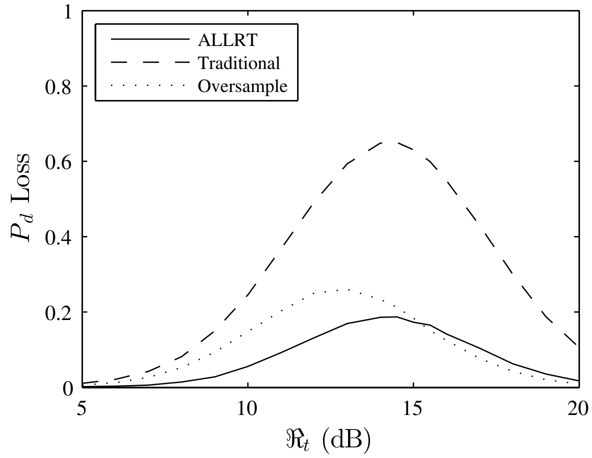

(a) Triangle matched filter response

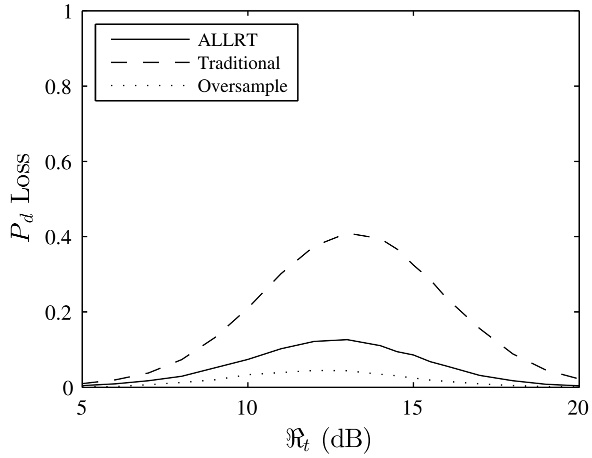

(b) Sinc matched filter response

Figure 12: $P_d$ loss for three detectors with $P_{fa} = 10^{-4}$ and five pulses.

13. Also, the location of maximum $P_d$ loss in total target SNR appears to increase with the number of pulses – 14 dB for five pulses and 15 dB for ten pulses. These general trends hold for the sinc matched filter response, but are less severe. Furthermore, notice that the ALLRT and oversample detectors appear less susceptible to $P_d$ loss. ALLRT and oversample $P_d$ loss are nearly equal for the triangle matched filter response, but the oversample detector slightly outperforms ALLRT for the sinc matched filter response. By inspection of Figures 11, 12, and 13, a region of concern appears to exist in terms of $P_d$ loss at around 10 dB - 18 dB. Unfortunately, as discussed in [48], surveillance radars employing pulsewidth agile waveforms should operate near 16 dB in order to minimize total radar time and energy

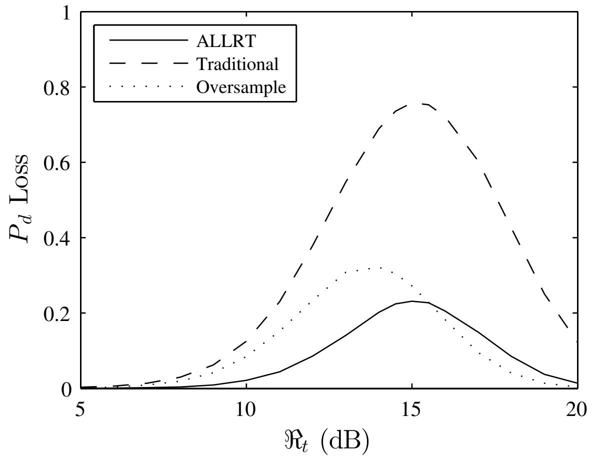

(a) Triangle matched filter response

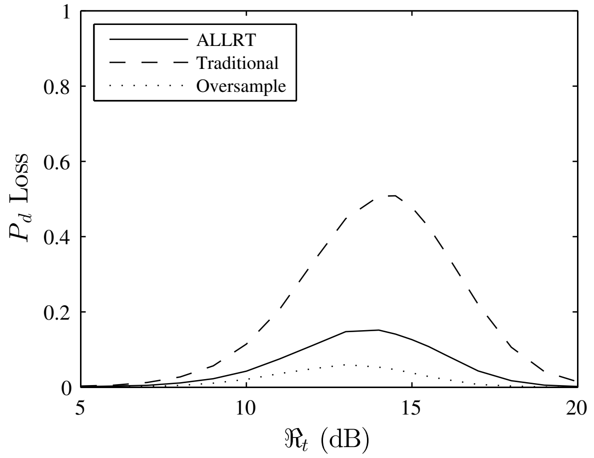

(b) Sinc matched filter response

Figure 13: $P_d$ loss for three detectors with $P_{fa} = 10^{-4}$ and ten pulses.

during track maintenance.

Notice that $P_d$ loss is less dramatic for high and low SNR values. A high value of $P_d$ loss indicates an SNR value that lies in the transition region where $P_d$ is maximally sensitive to changes in SNR. Since the transition region of $P_d$ becomes unboundedly steep as the number of pulses increases for a Swerling 2 target (see [32] for an illustration of this phenomenon), $P_d$ loss becomes more dramatic. We expect different behavior for a Swerling 1 target, since the transition region in $P_d$ does not become unboundedly steep with increasing number of pulses. Finally, note that $P_d$ loss is not unique to range-bin straddling; it is merely a reflection that any lossy phenomenon will have a greatly amplified effect when SNR falls

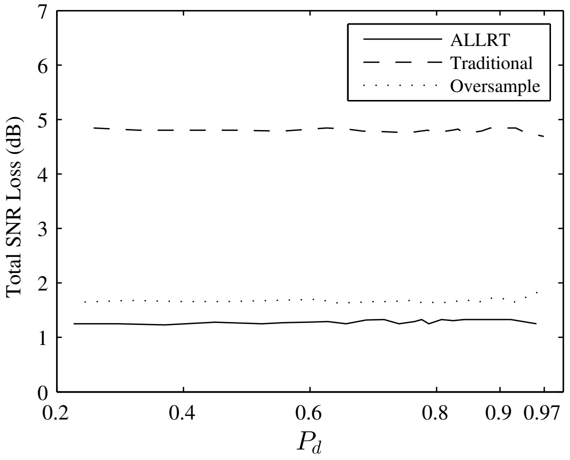

(a) Triangle matched filter response

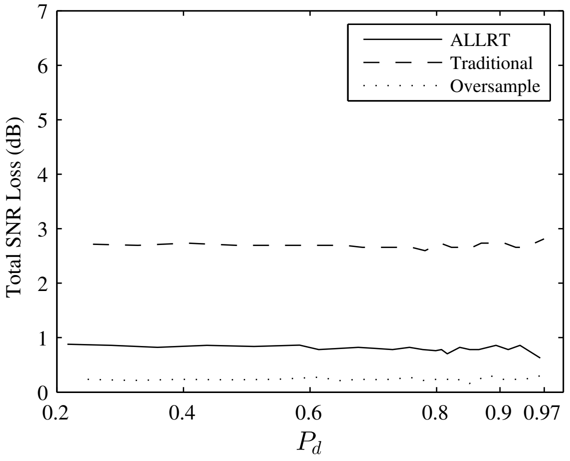

(b) Sinc matched filter response

Figure 14: Total SNR loss for three detectors with $P_{fa} = 10^{-4}$ and a single pulse.

within the steep transition region of a detection curve.

To be consistent with the results of [17], total SNR loss and average SNR loss are shown as a function of $P_d$. To make the calculation for total SNR loss, a maximum $P_d$ for a given $\Re_t$ is found with numerical simulation. Then, $\Re_t$ is slowly increased until the absolute difference between the minimum $P_d$ and the previously calculated maximum $P_d$ is less than 0.001, and total SNR loss is taken as the amount of increase in $\Re_t$. As shown in Figure 14, for a single pulse using the triangle matched filter response, total SNR loss is nearly 5 dB for the traditional detector, around 1.5 dB for the oversample detector, and slightly above 1 dB for the ALLRT detector. If the radar waveform selection algorithm incorrectly

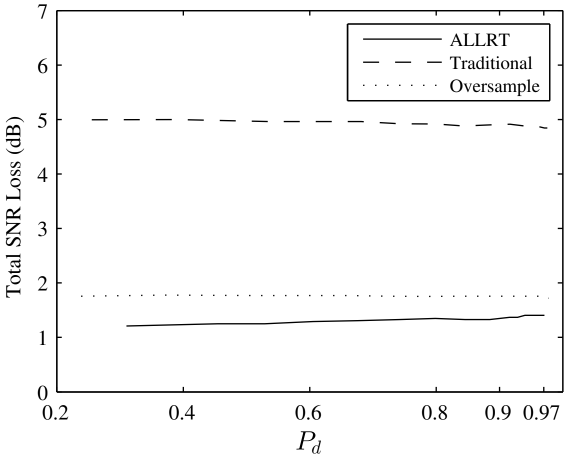

(a) Triangle matched filter response

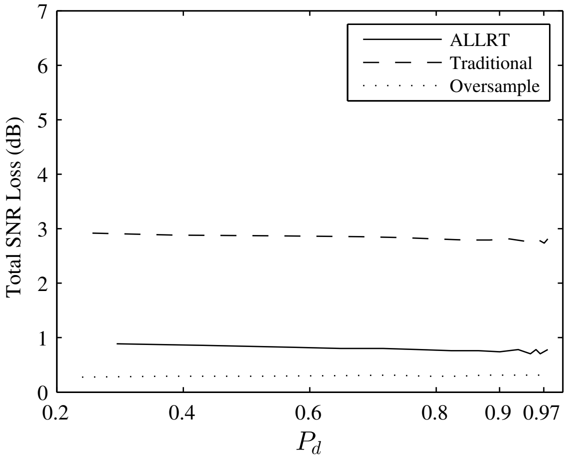

(b) Sinc matched filter response

Figure 15: Total SNR loss for three detectors with $P_{fa} = 10^{-4}$ and five pulses.

assumes a matched filter sample precisely at a target location, an increase of waveform energy by a factor of around $10^{5/10} \approx 3.15$ is required to guarantee a specified $P_d$ when using the traditional detector. For the ALLRT and oversample detectors, the total SNR loss is near 1.5 dB, corresponding to an increase of waveform energy by a factor of around $10^{1.5/10} \approx 1.4$ in order to achieve a specified $P_d$. Also, notice from Figure 14 that total SNR loss is reduced by using a sinc matched filter response. By inspection of Figures 15 and 16, total SNR loss only slightly increases with the number of pulses.

Interestingly, total SNR loss appears nearly independent of the number of pulses and $P_d$ for all detectors. For the traditional detector with the triangular matched filter response, a

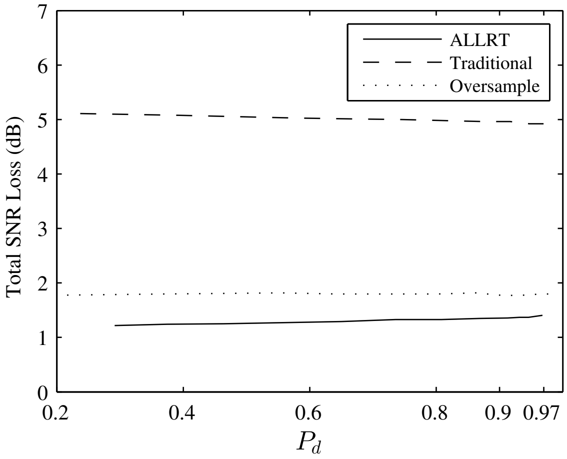

(a) Triangle matched filter response

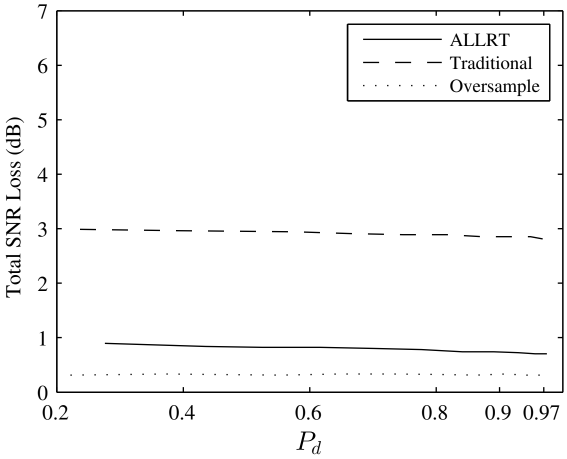

(b) Sinc matched filter response

Figure 16: Total SNR loss for three detectors with $P_{fa} = 10^{-4}$ and ten pulses.

rough back-of-the-envelope estimate gives a loss in observed power as -20log$_{10}\left(\frac{1}{2}\right) \approx 6$ dB, close to the loss of 5 dB shown in Figures 14, 15, and 16 for the traditional detector. For the ALLRT and oversample detectors, we do not have an explanation for the independence of total SNR loss with number of pulses and $P_d$. This is left for future study.

Average SNR loss for a single pulse is provided in Figure 17. The calculation is made using numerical simulations in a similar manner to the total SNR loss calculation. As shown, for a single pulse using a triangle matched filter response, the average SNR loss of the traditional detector slightly increases with increasing $P_d$. As the number of pulses increases, this behavior becomes more pronounced, as shown in Figures 18 and 19. With

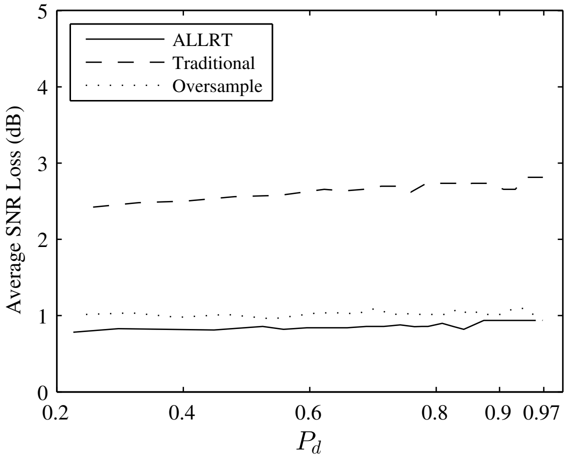

(a) Triangle matched filter response

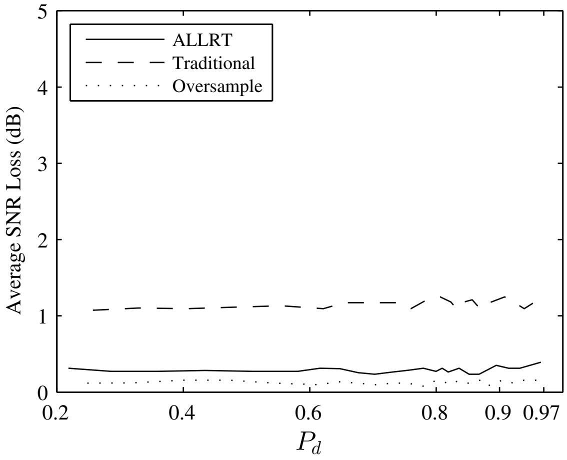

(b) Sinc matched filter response

Figure 17: Average SNR loss for three detectors with $P_{fa} = 10^{-4}$ and a single pulse.

ten pulses, the traditional detector has an average SNR loss of 2 dB at $P_d = 0.2$, and this increases to nearly 3.5 dB at $P_d = 0.97$. While this behavior was seen in the results of Cann in [17], the results are not exactly the same. This is because Cann investigated Swerling 0 and Swerling 1 targets, instead of Swerling 2 targets. Also notice from Figure 17 that average SNR loss decreases with a sinc matched filter response as compared to a triangle matched filter response. By inspection of Figures 17, 18, and 19, average SNR loss does not increase nearly as much with $P_d$ for the ALLRT and oversample detectors as compared to the traditional detector. In fact, for the ALLRT and oversample detectors, average SNR loss is never above 1 dB for the cases considered. Note that the results of the oversample

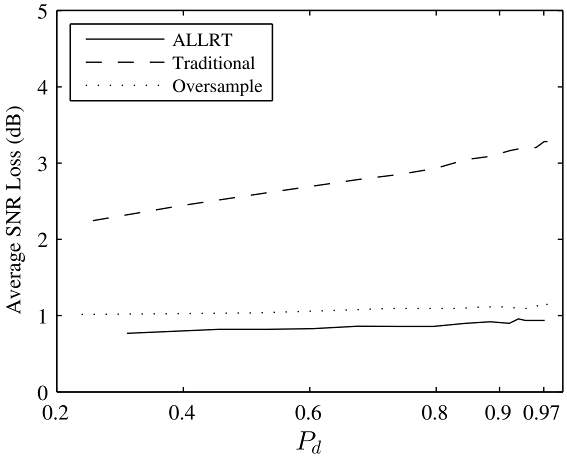

(a) Triangle matched filter response

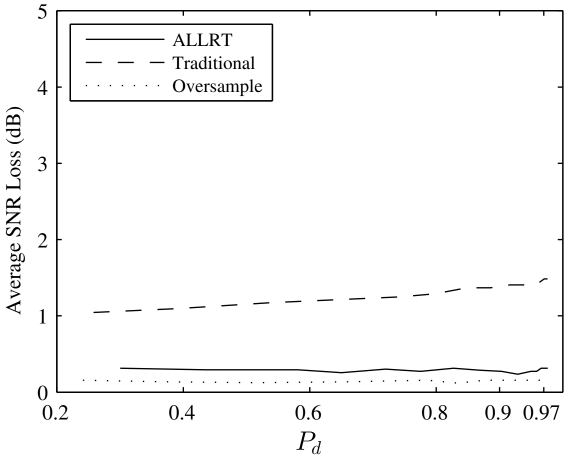

(b) Sinc matched filter response

Figure 18: Average SNR loss for three detectors with $P_{fa} = 10^{-4}$ and five pulses.

detector for average SNR loss agrees with the results of [17].

In general, the ALLRT detector outperforms the traditional detector in terms of all the loss metrics. Surprisingly, the ALLRT detector slightly outperforms the oversample detector in terms of the loss metrics for the triangle matched filter response, but the oversample detector performs slightly better for the sinc matched filter response. Since the oversample detector has the clear advantage of more data, this result may be counterintuitive. Assuming a target is uniformly distributed in the region under test, $P_d$ as a function of $\mathfrak{R}_t$ for a single pulse is provided in Figure 20. As shown, the oversample detector provides the best on-average detection performance in this case. Therefore, since the oversample detector has

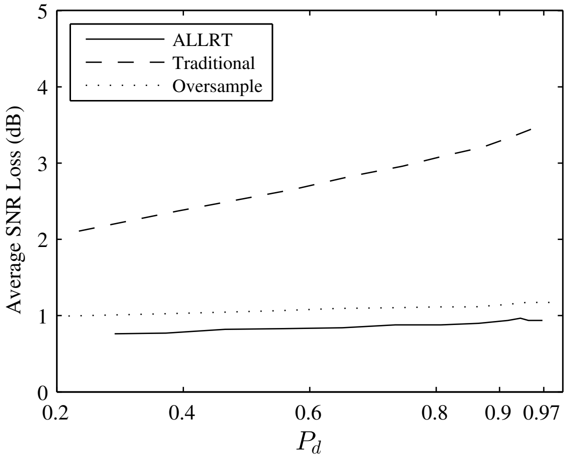

(a) Triangle matched filter response

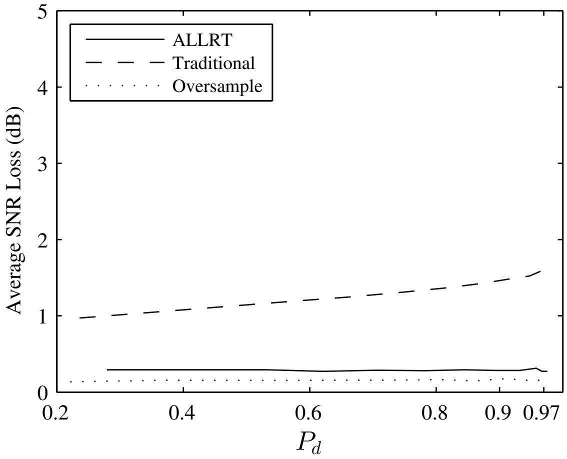

(b) Sinc matched filter response

Figure 19: Average SNR loss for three detectors with $P_{fa} = 10^{-4}$ and ten pulses.

more data, it has a higher average $P_d$. However, as shown in this section, the ALLRT detector has similar robustness against the negative effects of straddling loss.

### 3.2.4 Optimal Number of Pulses

By careful inspection of Figures 7, 8, and 9, an optimal number of pulses that maximizes $P_d$ appears to exist. For a radar dwell providing a specified $\Re_t$, denote $N_{opt}$ as the optimal number of pulses that maximizes $P_d$. This optimization originally appeared in [7] assuming a Swerling 2 target and energy contained in a single matched filter sample, and the results from [7] are reproduced in Table 1a. In Table 1b, results are provided for the traditional detector described in this chapter with a target located on a matched filter sample. As

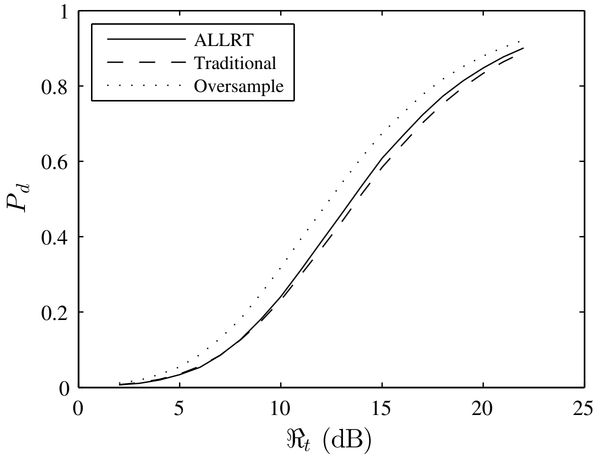

(a) Triangle matched filter response

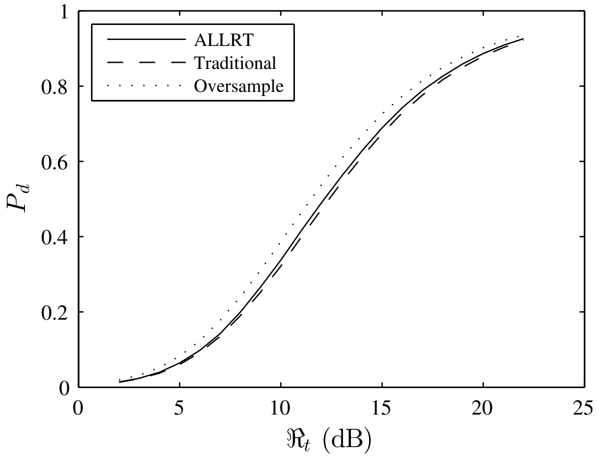

(b) Sinc matched filter response

Figure 20: Average $P_d$, assuming target is uniformly distributed in the region under test. $P_{fa} = 10^{-4}$ and a single pulse is used.

shown, $N_{opt}$ agrees with the results in [7]. However, the difference in $P_d$ arises because the traditional detector in our simulations considers two adjacent matched filter samples, which means the detection threshold must be raised slightly in order to maintain a specified $P_{fa}$ in the region under test. In Table 1c, results are provided with a target uniformly distributed in the region under test. As shown, $N_{opt}$ is quite lower than suggested in previous literature for this case. For $\Re_t = 40$ (reported on linear scale for consistency with [7]), $N_{opt}$ is found to be three pulses instead of nine as reported in [7]. The decrease in $N_{opt}$ is the result of range bin straddling that causes an average SNR loss of around 2-3 dB using the traditional detector, as discussed in Section 3.2.3. Therefore, Table 1c should roughly match Table 1a if $\mathfrak{R}_t$ is decreased by a half. In fact, using numerical simulations, we found $N_{opt} = 6$ for $\mathfrak{R}_t = 60$ using the same setup as in Table 1c, which is the same $N_{opt} = 6$ with $\mathfrak{R}_t = 30$ in Table 1a. $N_{opt}$ for the various detectors described in this work are provided in Tables 3, 4, and 2. In general, $N_{opt}$ is slightly higher for a sinc matched filter response as compared to the triangle matched filter response. Also, $N_{opt}$ tends to be slightly higher for the ALLRT and oversample detectors as compared to the traditional detector.

| Pulses | $\mathfrak{R}_t$ | | |
|---|---|---|---|
| N | 20 | 30 | 40 |
| 1 | 0.645 | 0.743 | 0.799 |
| 2 | 0.710 | 0.831 | 0.891 |
| 3 | **0.725** | 0.864 | 0.924 |
| 4 | 0.724 | 0.879 | 0.941 |
| 5 | 0.714 | 0.885 | 0.949 |
| 6 | 0.699 | **0.887** | 0.954 |
| 7 | 0.681 | 0.886 | 0.957 |
| 8 | 0.662 | 0.882 | 0.958 |
| 9 | 0.641 | 0.878 | **0.958** |
| 10 | 0.620 | 0.872 | 0.958 |

(a) Results from Blair [7]

| Pulses | $\mathfrak{R}_t$ | | |
|---|---|---|---|
| N | 20 | 30 | 40 |
| 1 | 0.623 | 0.727 | 0.785 |
| 2 | 0.686 | 0.816 | 0.880 |
| 3 | **0.699** | 0.849 | 0.915 |
| 4 | 0.693 | 0.862 | 0.931 |
| 5 | 0.681 | 0.868 | 0.941 |
| 6 | 0.664 | **0.869** | 0.946 |
| 7 | 0.645 | 0.867 | 0.948 |
| 8 | 0.622 | 0.862 | 0.949 |
| 9 | 0.602 | 0.857 | **0.950** |
| 10 | 0.577 | 0.850 | 0.949 |

(b) Traditional detector with target on a matched filter sample

| Pulses | $\mathfrak{R}_t$ | | |
|---|---|---|---|
| N | 20 | 30 | 40 |
| 1 | **0.441** | 0.566 | 0.646 |
| 2 | 0.435 | **0.603** | 0.709 |
| 3 | 0.405 | 0.597 | **0.721** |
| 4 | 0.370 | 0.578 | 0.715 |
| 5 | 0.341 | 0.557 | 0.706 |
| 6 | 0.312 | 0.534 | 0.692 |
| 7 | 0.287 | 0.512 | 0.676 |
| 8 | 0.263 | 0.489 | 0.659 |
| 9 | 0.243 | 0.470 | 0.643 |
| 10 | 0.224 | 0.448 | 0.625 |

(c) Traditional detector with target uniformly distributed between samples and a triangular matched filter response

Table 1: $P_d$ for Rayleigh targets with $P_{fa} = 10^{-4}$.

|  | $\mathfrak{R}_t$ |  |  |
|---|---|---|---|
| Detector | 20 (13 dB) | 30 (14.77 dB) | 40 (16 dB) |
| Traditional | 1 | 2 | 3 |
| ALLRT | 1 | 2 | 3 |
| Oversample | 1 | 2 | 3 |

(a) Triangle matched filter response

|  | $\mathfrak{R}_t$ |  |  |
|---|---|---|---|
| Detector | 20 (13 dB) | 30 (14.77 dB) | 40 (16 dB) |
| Traditional | 2 | 3 | 5 |
| ALLRT | 2 | 3 | 5 |
| Oversample | 2 | 3 | 5 |

(b) Sinc matched filter response

Table 2: Optimal number of pulses with a $P_{fa} = 10^{-5}$ and target uniformly distributed in the region under test.

|  | $\mathfrak{R}_t$ |  |  |
|---|---|---|---|
| Detector | 20 (13 dB) | 30 (14.77 dB) | 40 (16 dB) |
| Traditional | 1 | 2 | 3 |
| ALLRT | 1 | 2 | 4 |
| Oversample | 1 | 2 | 4 |

(a) Triangle matched filter response

|  | $\mathfrak{R}_t$ |  |  |
|---|---|---|---|
| Detector | 20 (13 dB) | 30 (14.77 dB) | 40 (16 dB) |
| Traditional | 2 | 3 | 5 |
| ALLRT | 2 | 4 | 6 |
| Oversample | 2 | 4 | 6 |

(b) Sinc matched filter response

Table 3: Optimal number of pulses with $P_{fa} = 10^{-4}$ and target uniformly distributed in the region under test.

## *3.3 Concluding Remarks*

Traditional radar detection compares the observed SNR in a given matched filter sample to a specified threshold. However, target energy is typically spread across multiple adjacent matched filter samples, and traditionally the correlation between matched filter samples is ignored. Using a signal model that jointly considers adjacent matched filter samples, the ALLRT detector that includes the correlation is proposed. The coefficients used in the ALLRT detector are provided for the triangle matched filter response and the sinc matched filter response. As discussed in Appendix A, the ALLRT detector includes knowledge of

|  | $\Re_t$ |  |  |
|---|---|---|---|
| Detector | 20 (13 dB) | 30 (14.77 dB) | 40 (16 dB) |
| Traditional | 2 | 3 | 4 |
| ALLRT | 2 | 3 | 4 |
| Oversample | 2 | 3 | 4 |

(a) Triangle matched filter response

|  | $\Re_t$ |  |  |
|---|---|---|---|
| Detector | 20 (13 dB) | 30 (14.77 dB) | 40 (16 dB) |
| Traditional | 3 | 4 | 6 |
| ALLRT | 3 | 5 | 7 |
| Oversample | 3 | 5 | 7 |

(b) Sinc matched filter response

Table 4: Optimal number of pulses with $P_{fa} = 10^{-3}$ and target uniformly distributed in the region under test.

the functional form of transmitted waveform for multiple adjacent matched filter samples. Detection performance of the ALLRT detector was compared to traditional detection for two types of matched filter outputs, and a Swerling 2 target model. Since the triangle matched filter response is similar to the main lobe of a phase coded waveform and a sinc matched filter response is similar to that of an LFM waveform, we expect similar behavior for waveforms commonly used in practice. Performance metrics employed in this work measure performance losses due to the unknown location of a target between matched filter samples. Interesting findings include:

- Using traditional detection, $P_d$ is minimized if a target is centered between matched filter samples. $P_d$ loss increases with the number of pulses, and for ten pulses the loss can be near an alarming 80% for the traditional detector. This value is not entirely surprising since the transition region of $P_d$ for Swerling II targets becomes steeper as the number of pulses increases.

- $P_d$ loss, average SNR loss, and total SNR loss are less severe with a sinc matched filter response when compared to a triangular matched filter response for the detectors used in this study.

- $P_d$ loss, average SNR loss, and total SNR loss are less severe with the ALLRT detector as compared to the traditional detector. The traditional and ALLRT detectors use the same sample rate.

- Using a triangular matched filter response, ALLRT provides similar performance to the oversample detector in terms of $P_d$ loss, average SNR loss, and total SNR loss. The oversample detector slightly outperforms ALLRT for a sinc matched filter response.
- A region of severity for $P_d$ loss exists in $\mathfrak{R}_t$ for all detectors, around 12-18 dB.
- An optimal number of pulses for a given $\mathfrak{R}_t$ that maximizes $P_d$ is less than previously reported in the literature. For $\mathfrak{R}_t = 16$ dB, nine pulses was previously reported as optimal. Using a triangular matched filter response, the optimal number of pulses were found to be three for traditional detection and four with the ALLRT detector for $\mathfrak{R}_t = 16$dB. For a sinc matched filter response, the optimal number of pulses increases to five and six.

The proposed ALLRT detector can provide stability in terms of $P_d$ that rivals traditional detectors with oversampled matched filter outputs. The radar estimation problem of range and angle is investigated by jointly considering adjacent matched filter samples in the next chapter. Future research includes exploring radar waveform design in the ALLRT detector framework.

# CHAPTER IV

# RANGE AND DIRECTION-OF-ARRIVAL ESTIMATION

The topic of monopulse direction-of-arrival (DOA) estimation is prevalent in the radar literature. In [34], Mosca found the maximum-likelihood (ML) solution for DOA. In [8], Blair proposed a method-of-moments approach to alleviate the bias of the monopulse ratio for off-boresight targets at the cost of inflated error variance. Although often not mentioned in the monopulse literature, radar tracking of off-boresight objects is particularly important when considering energy management considerations of a radar, as in [48], or when tracking groups of objects closely located in angle, as briefly discussed in [52]. In nearly all of the monopulse DOA literature, target energy is assumed to be contained in a single range bin.

As discussed in Section 2.1, radars using pulse compression techniques typically use a sampled version of the matched filter output for detection and estimation purposes. In practice, target energy is contained in multiple adjacent matched filter samples, resulting in correlation between adjacent samples. In the radar literature, this is called range gate straddling, gate-spitting, gate spacing loss, or bin-spreading; it is typically treated as a nuisance and regarded as an undesired loss in signal energy. Practical "centroiding" techniques have been proposed to "fuse" the DOA estimates from adjacent samples as in [45]. A sub-bin range estimate is also provided in [45] by utilizing bin-straddling. However, the approaches in [45] do not employ the correlation between samples, and are therefore suboptimal.

In recent publications, bin spreading has been shown useful for a variety of estimation purposes. For example, resolving multiple unresolved targets was achieved by using the observed correlation between adjacent sum and difference matched filter samples in [56]. Willett explored the CRLBs for target localization using a signal model that jointly considers adjacent matched filter samples and showed that oversampling the output of the matched filter allows for more targets to be resolved [53]. The bounds in [53] were found numerically; they were not expressed in closed-form. In [56], Zhang showed that the observed correlation between matched filter samples can be used to resolve targets spaced closer than the classical interpretation of radar resolution by using an ML approach. Numerical methods were used to arrive at ML estimates of range and angle for multiple targets of type Swerling 2. Zhang further compared estimation performance of the ML estimators to a "centroid" approach similar to [45] and showed performance benefits for the case of two targets. However, in [56], target strength is assumed to be a known parameter and reported variances for target location estimates are not provided.

Data fusion algorithms usually require a reliable error/variance report in order to determine the relative value of the estimate. In much of the classical radar literature, DOA estimator variance is typically straightforward to compute. However, incorporating additional modeling complexities, such as matched filter sampling in the work of Zhang in [56], often results in complex numerical techniques for a solution, in which case error variance reporting is far from straightforward. A reasonable approach for the ML technique of [56] is to use the CRLBs from [53] as an error variance report. However, CRLBs are often functions of unknown parameters, as is the case in [53].

In this Chapter, we explicitly incorporate sampling into the statistical model for sum and difference channel signal samples, and derive ML estimators. This work may be viewed as an elaboration of [56] and [53] for the case of a single Rayleigh target, with emphasis on obtaining simple expressions that might be used in a real-time system. Furthermore, we derive closed-form CRLBs for the unknown localization parameters, and propose the generalized Cramér-Rao lower bound (GCRLB), which is the CRLB evaluated at estimated quantities (rather than true values), as an error variance report. Much of this chapter follows our expositions in [26], [24], and [23].

## *4.1 Signal and Target Modeling*

Following the assumptions in Section 2.1, the sum and difference channel samples of a monopulse system can be expressed as

$$s(b) = xr(b\Delta t - \tau) + n_s(b\Delta t), \tag{58}$$

$$d(b) = x\eta r(b\Delta t - \tau) + n_d(b\Delta t). \tag{59}$$

Note that a single pulse corresponds to two (i.i.d.) observations of both (58) and (59).

In this chapter, a sample rate equal to the Rayleigh resolution is assumed, resulting in a maximum of two adjacent samples in the main lobe of the matched filter response.[1] Furthermore, denote the variance of sum and difference channel noise samples as $\sigma_s^2$ and $\sigma_d^2$, respectively. Denoting the sub-bin location of a target as

$$c = \frac{\tau - b\Delta t}{\Delta t}, \tag{60}$$

the two samples of the main lobe of the matched filter response can be expressed as

$$r_1(c) = r(c\Delta t), \tag{61}$$

$$r_2(c) = r((c-1)\Delta t). \tag{62}$$

Note that $c \in [0, 1]$. The resulting signal vector for $N$ pulses is written exfplicitly as

$$\mathbf{s}_l = \left[s_l(0) \;\; s_l(1) \;\; d_l(0) \;\; d_l(1)\right]^T, \qquad 1 \leq l \leq 2N, \tag{63}$$

with

$$s_l(0) = xr_1 + n_s(0), \tag{64}$$

$$s_l(1) = xr_2 + n_s(1), \tag{65}$$

$$d_l(0) = x\eta r_1 + n_d(0), \tag{66}$$

$$d_l(1) = x\eta r_2 + n_d(1). \tag{67}$$

Here, $E[\mathbf{s}_l]$=0, and resulting covariance matrix for (63) can be written as

$$\mathbf{K} = E\left[\mathbf{s}_l\mathbf{s}_l^T\right] = \begin{bmatrix} \beta^2 r_1^2 + \sigma_s^2 & \beta^2 r_1 r_2 & \beta^2 \eta r_1^2 & \beta^2 \eta r_1 r_2 \\ \beta^2 r_1 r_2 & \beta^2 r_2^2 + \sigma_s^2 & \beta^2 \eta r_1 r_2 & \beta^2 \eta r_2^2 \\ \beta^2 \eta r_1^2 & \beta^2 \eta r_1 r_2 & \beta^2 \eta^2 r_1^2 + \sigma_d^2 & \beta^2 \eta^2 r_1 r_2 \\ \beta^2 \eta r_1 r_2 & \beta^2 \eta r_2^2 & \beta^2 \eta^2 r_1 r_2 & \beta^2 \eta^2 r_2^2 + \sigma_d^2 \end{bmatrix}. \tag{68}$$

Estimators for the unknown parameters $\eta$ and $c$ (which appear in functions of the $r_1$ and $r_2$ in (68)), along with statistically consistent variance reports for each parameter estimate,

---

[1] This assumption can be found extensively in the literature. For examples, see [45], [56], [15], [17].

are the focus of this chapter. In this work, $\beta^2$ is treated as a nuisance parameter, and its estimation is not studied in depth. Monopulse processing proposed in this thesis requires calculation of the sample covariance matrix. Imposing the zero-mean assumption on $\mathbf{s}_l$, the sample covariance is written explicitly as

$$\bar{\mathbf{K}} = \frac{1}{2N}\sum_{l=1}^{2N} \mathbf{s}_l \mathbf{s}_l^T = \begin{bmatrix} k_{11} & k_{12} & k_{13} & k_{14} \\ k_{12} & k_{22} & k_{23} & k_{24} \\ k_{13} & k_{23} & k_{33} & k_{34} \\ k_{14} & k_{24} & k_{34} & k_{44} \end{bmatrix}, \tag{69}$$

where $N$ is the total number of pulses.

## 4.2 Detection and Estimation

This section presents estimators for the unknown $\beta^2$, $c$. Derivations of these estimators are provided in the Appendix. The estimators for $\beta^2$ and $c$ use the sum channel samples, whereas the estimator for $\eta$ uses both the sum and difference channel samples. CRLBs for each unknown parameter are also provided in closed form. The new estimators are compared with the approaches of [56] and [45].

### 4.2.1 Detection of Target Presence

In Chapter 3, the average loglikelihood ratio test (ALLRT) was proposed as a detector. Although not explicitly mentioned in [25], the ALLRT is derived using statistical descriptions of only the sum channel of a monopulse system; the difference channel is ignored. In the derivation of the ALLRT, the test statistic in the loglikelihood ratio test (LLRT) is shown to involve the unknown parameter $c$. To handle the unknown $c$, a uniform distribution between zero and one is assumed and integrated through the LLRT, thus providing the *average* loglikelihood ratio test. In terms of the sample covariance of (69), the ALLRT detector can be written as

$$\frac{d_1}{\sigma_s^2}\left(k_{11} + k_{22}\right) + \frac{d_2}{\sigma_s^2} k_{12} \quad \overset{H_1}{\underset{H_0}{\gtrless}} \gamma_a. \tag{70}$$

The coefficients $d_1$ and $d_2$ in (70) depend upon the matched filter response of the transmitted waveform, and $\gamma_a$ denotes the ALLRT threshold. For a triangle matched filter response, the coefficients are simple, $d_1 = d_2 = 1$, and extension to any matched filter response is straightforward, as shown in Chapter 3. For a sinc matched filter response, the coefficients are $d_1 \approx 0.4514$ and $d_2 \approx 0.494$. In Chapter 3, the ALLRT detector is shown to provide benefits over traditional detection schemes that isolate detection to each individual sample. In particular, the ALLRT can be seen as an alternative to oversampling the output of the matched filter to alleviate bin-straddling detection issues.

Investigation into the use of the difference channel in the detection process is left for future work. However, notice that for targets located on boresight (i.e., $\eta = 0$), the difference channel samples contain only noise. Thus, we expect detection benefits with the use of the difference channel only for off-boresight (i.e. $|\eta| \geq 0.5$) targets.

### 4.2.2 Range and Target Strength Estimation

As shown in Appendix B, estimating $c$ is equivalent to solving

$$\frac{k_{11} - k_{22}}{k_{12}} = \frac{r_1(\hat{c})^2 - r_2(\hat{c})^2}{r_1(\hat{c}) r_2(\hat{c})}, \tag{71}$$

for $\hat{c}$, where $r_1$ and $r_2$ are given as (61) and (62), respectively, and $k_{11}$, $k_{22}$, and $k_{12}$ are elements of the sample covariance of (69). Clearly, $\hat{c}$ depends upon the matched filter response of the transmitted waveform. However, given a known matched filter response and measured data, simple search strategies can be devised using (71). For example, several candidate $\hat{c}$ values can be generated, perhaps one-hundred values between zero and one, and tested to determine where (71) is achieved. Assuming a triangle matched filter response, a closed-form expression for $\hat{c}$ is developed in Appendix B:

$$\hat{c} = \frac{k_{11} - k_{22} + 2k_{12} - \sqrt{(k_{11} - k_{22})^2 + 4k_{12}^2}}{2(k_{11} - k_{22})}. \tag{72}$$

The CRLB for $\hat{c}$ is shown to be equivalent to

$$CRLB_{\hat{c}} = \frac{(r_1^2 + r_2^2) + \frac{1}{\Re_r}}{2\Re_t \left( r_1 \frac{\partial r_2}{\partial c} - r_2 \frac{\partial r_1}{\partial c} \right)^2}. \tag{73}$$

Notice that the CRLB depends upon the transmitted waveform through the true values of the samples and the partial derivative of the matched filter response with respect to the target location. Clearly, the selection of a transmitted waveform, along with the target location, effects the CRLB for $\hat{c}$. In Appendix B, an estimate for $\beta^2$ is shown to be

$$\hat{\beta}^2 = \frac{k_{11}\hat{r}_1^2 + k_{22}\hat{r}_2^2 - (\hat{r}_1^2 + \hat{r}_2^2)\sigma_s^2 + 2k_{12}\hat{r}_1\hat{r}_2}{(\hat{r}_1^2 + \hat{r}_2^2)^2}, \tag{74}$$

with $\hat{r}_1 = r_1(\hat{c})$ and $\hat{r}_2 = r_2(\hat{c})$. Note that a $\hat{c}$ is required for (74). To our knowledge, (74) is the first appearance of a target strength estimator that jointly considers adjacent samples.

A common technique, in practice, for sub-bin range estimation is the centroid approach of [45], in which the range estimate is an SNR weighted centroid of adjacent samples. In terms of the sample covariance, the centroid estimator for $c$ is

$$\hat{c}_{centroid} = \frac{k_{22}}{k_{11} + k_{22}}. \tag{75}$$

To compare performance of the ML and centroid range estimators, MSE is calculated for various values of target SNR and number of pulses. For each case of target SNR and number of pulses, 1,000,000 target locations are generated from a uniform distribution between two range bins. MSE is calculated on trials that pass the ALLRT detection threshold for a given probability of false alarm. The ratio of MSEs on the MLE and centroid range estimators for $P_{fa}$=$10^{-4}$ are shown in Table 5. In this table, a value less than one corresponds to a case where centroiding performs better than the MLE. As shown, the MLE outperforms centroiding for nearly every case considered. Centroiding only slightly outperforms the MLE for a few very low SNR targets.

To see more detailed behavior of these estimators, the two components of MSE, bias and variance, were investigated as $c$ is swept from zero to one. The bias and standard deviation (square root of variance) of the estimators for the case of $\mathfrak{R}_r = 10$ dB with 10 pulses are shown in Figures 21 and 22. Centroiding displays strange bias behavior, which contributes to the high MSE as compared to the MLE. Note that the MLE is biased near the edges because the estimate is constrained to be between zero and one. Values outside zero and one do not make sense under the hypothesis of target presence within the two samples.

Table 5: Ratio of MSE (centroiding to MLE), $P_{fa} = 10^{-4}$.

| $\Re_r$ (dB) | Number of Pulses | | | | | | | | | |
|---|---|---|---|---|---|---|---|---|---|---|
| | 1 | 2 | 3 | 4 | 5 | 6 | 7 | 8 | 9 | 10 |
| 5 | 1.01 | 0.94 | 0.98 | 1.05 | 1.14 | 1.21 | 1.27 | 1.34 | 1.42 | 1.47 |
| 6 | 1.06 | 0.99 | 0.99 | 1.04 | 1.09 | 1.14 | 1.19 | 1.24 | 1.28 | 1.33 |
| 7 | 1.12 | 1.02 | 1.01 | 1.04 | 1.07 | 1.10 | 1.14 | 1.16 | 1.19 | 1.21 |
| 8 | 1.18 | 1.07 | 1.06 | 1.05 | 1.08 | 1.10 | 1.11 | 1.14 | 1.16 | 1.17 |
| 9 | 1.25 | 1.15 | 1.12 | 1.12 | 1.13 | 1.14 | 1.16 | 1.18 | 1.20 | 1.22 |
| 10 | 1.33 | 1.24 | 1.21 | 1.21 | 1.23 | 1.26 | 1.28 | 1.31 | 1.35 | 1.39 |
| 11 | 1.42 | 1.34 | 1.34 | 1.36 | 1.40 | 1.45 | 1.51 | 1.58 | 1.65 | 1.73 |
| 12 | 1.53 | 1.47 | 1.50 | 1.56 | 1.66 | 1.77 | 1.89 | 2.02 | 2.16 | 2.30 |
| 13 | 1.64 | 1.64 | 1.73 | 1.87 | 2.04 | 2.24 | 2.47 | 2.70 | 2.93 | 3.18 |
| 14 | 1.76 | 1.83 | 2.01 | 2.27 | 2.59 | 2.92 | 3.28 | 3.66 | 4.05 | 4.43 |
| 15 | 1.89 | 2.07 | 2.39 | 2.84 | 3.33 | 3.88 | 4.43 | 5.02 | 5.58 | 6.18 |

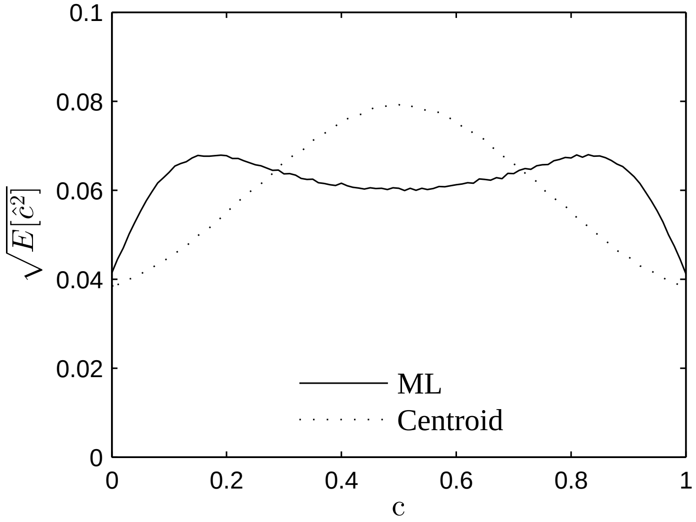

Figure 21: Standard deviation in $\hat{c}$ for the range estimators using 10 pulses at $\Re_r = 10$ dB.

### 4.2.3 DOA Estimation

In Appendix B, estimating $\eta$ is shown to be equivalent to solving

$$a_1\hat{\eta}^3 + a_2\hat{\eta}^2 + a_3\hat{\eta} + a_4 = 0 \tag{76}$$

for $\hat{\eta}$. The polynomial coefficients in (76) are rather complicated and can be found in Appendix B. Note that in the derivation of $\hat{\eta}$, the estimator is a ML solution with $\beta^2$ and $c$ assumed as known parameters. However, replacing $\beta^2$ and $c$ with estimates $\hat{\beta}^2$ and $\hat{c}$ from Section 4.2.2 gives (76) as a generalized maximum-likelihood (GML) solution. Note that all elements of the sample covariance appear in the polynomial coefficients of (76). Assuming

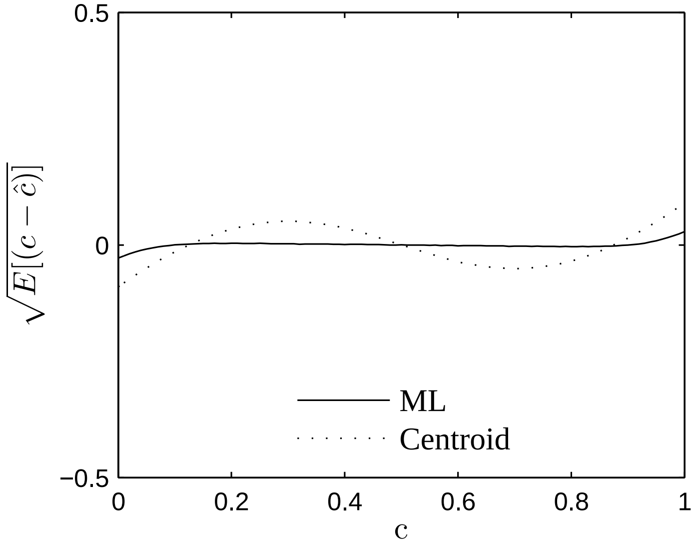

Figure 22: Estimator bias in $\hat{c}$ for the range estimators using 10 pulses at $\mathfrak{R}_r = 10$ dB.

$c$ and $\beta^2$ are unknown parameters, the CRLB for $\hat{\eta}$ is given in Appendix B as

$$CRLB_\eta = \frac{(r_1^2 + r_2^2)\left(\eta^2 + \frac{\sigma_d^2}{\sigma_s^2}\right) + \frac{\sigma_d^2}{\beta^2}}{2\mathfrak{R}_t(r_1^2 + r_2^2)^2}. \tag{77}$$

Notice that the matched filter sampling process affects $\eta$ estimation performance through $(r_1^2 + r_2^2)$, and for many waveforms, the CRLB is maximized when target energy is split evenly across adjacent matched filter samples. For a specified matched filter response, (77) can be used to determine the maximum amount of information about $\eta$ that is "lost" in the matched filter sampling process as shown below. Finally, notice that the CRLB increases with increasing $\eta^2$, thus off-boresight targets result in less accurate estimation.

Assuming $\sigma_d^2 = \sigma_s^2$, followed by algebraic manipulation, of (77) gives

$$CRLB_\eta = \frac{\left(\eta^2 + 1\right) + \frac{1}{\mathfrak{R}_r(r_1^2 + r_2^2)}}{2N\mathfrak{R}_r(r_1^2 + r_2^2)}, \tag{78}$$

in which a critical observation is made: in terms of $\eta$ estimation, bin-spreading can be seen as a direct loss in target SNR through the term $(r_1^2 + r_2^2)$. Assuming a triangle matched filter response, worst-case loss results from target energy split evenly across two matched filter samples. In this case, the loss is written explicitly as $(r_1^2 + r_2^2) = 1/2$. Note that for suboptimal monopulse processing, the loss is guaranteed to be more than 1/2, in general.

In conventional monopulse radar systems, the in-phase part of the monopulse ratio is used as the angle of arrival estimate [43]. In view of (8)-(9), the in-phase part of the monopulse ratio for matched filter sample $b$ is expressed as,

$$y_i(b) = \frac{d_i(b)s_i(b) + d_q(b)s_q(b)}{s_i^2(b) + s_q^2(b)}, \tag{79}$$

where

$$s_i(b) = Re\left\{s_c(b)\right\}, \tag{80}$$

$$s_q(b) = Im\left\{s_c(b)\right\}, \tag{81}$$

$$d_i(b) = Re\left\{d_c(b)\right\}, \tag{82}$$

$$d_q(b) = Im\left\{d_c(b)\right\}. \tag{83}$$

For the case of multiple pulses, the monopulse ratio for matched filter sample $b$ is an SNR weighted average of the individual monopulse ratios using the observed SNR for each matched filter sample [7]. It is well known for low and moderate SNR values, that (79) is a notably biased estimate of $\eta$.

Conventional DOA estimation is compared to the ML estimator of (76) using the Cramér-Rao normalized root mean square error (CNRMSE) and estimator bias. For each specific selection of $\Re_r$, $\eta$, $c$, and number of pulses, $50/P_{fa}$ samples of (8)-(9) were generated, and the root mean square error (RMSE) of each estimator is computed. This RMSE is further divided by the square root of the CRLB, giving the CNRMSE. The CNRMSE provides a general idea of the efficiency of the estimator, along with a justification of a reported CRLB to "cover" errors.

CNRMSE and estimator bias are provided in Figures 23 and 24 for the traditionally assumed case of target energy contained in a single matched filter sample. As shown, the centroid estimator that uses the in-phase part of the monopulse ratio displays bias behavior, around 10% of the true value of $\eta$, whereas the ML estimator provided in this work has nearly zero bias. The ML estimator is nearly efficient as shown in Figure 24 as the errors are around 1.1 times the square root of the Cramér-Rao lower bound. Also notice that, as expected from traditional DOA literature, the monopulse ratio is superior for -0.5$\geq \eta \geq$0.5.

CNRMSE and estimator bias are provided in Figures 25 and 24 for the case of target energy contained equally among adjacent matched filter samples (i.e., $c = 1/2$). As shown, performance of the centroid estimator begins to drastically break down in this case, as the estimator is notably biased and errors approach 2.5 times the CRLB, in terms of error standard deviation. Regardless, even in this case, the monopulse ratio is difficult to beat for targets close to boresight, -0.25$\leq \eta \leq$0.25. The ML estimator is the superior estimator for targets off-boresight, as it has nearly zero bias and is reasonably close to the CRLB.

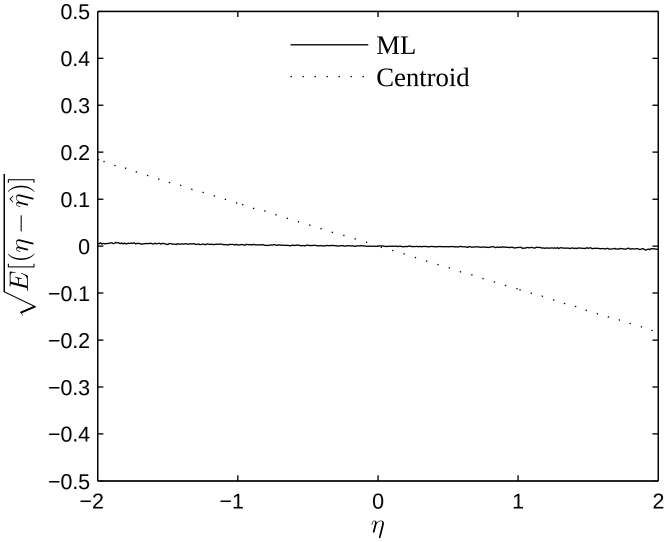

Figure 23: Estimator bias in $\hat{\eta}$ for $\mathfrak{R}_r = 10$ dB, eight pulses, triangle matched filter response, and $P_{fa} = 10^{-3}$. Target energy is contained in a single matched filter sample.

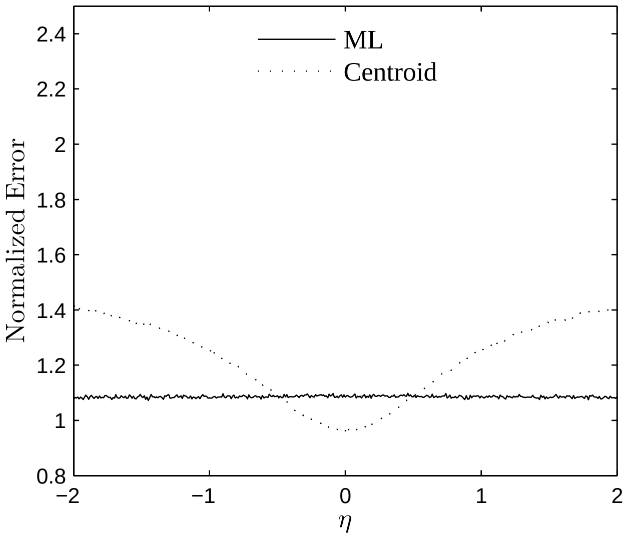

Figure 24: CNRMSE in $\hat{\eta}$ for $\mathfrak{R}_r = 10$ dB, eight pulses, triangle matched filter response, and $P_{fa} = 10^{-3}$. Target energy is contained in a single matched filter sample.

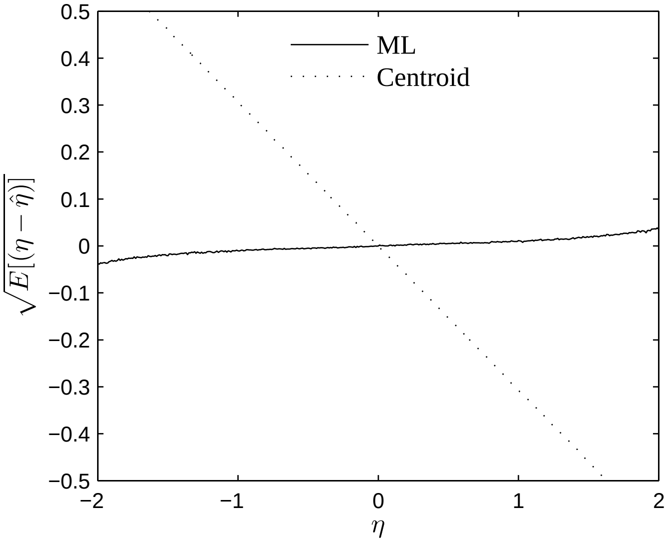

Figure 25: Estimator bias in $\hat{\eta}$ for $\mathfrak{R}_r = 10$ dB, eight pulses, triangle matched filter response, and $P_{fa} = 10^{-3}$. Target energy is distributed equally in adjacent matched filter samples.

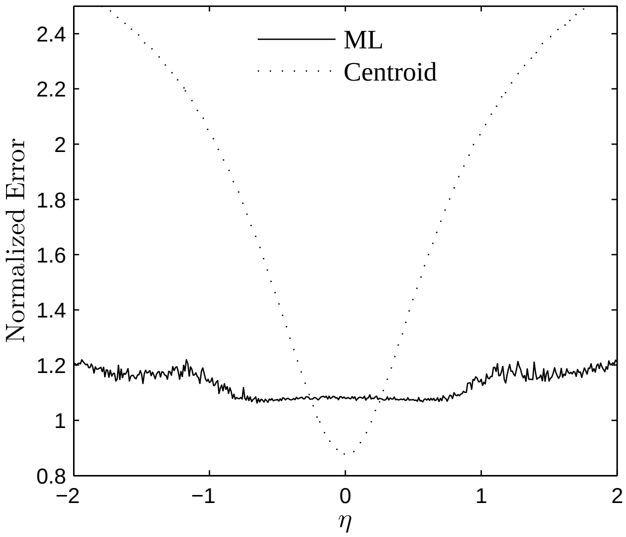

Figure 26: CNRMSE in $\hat{\eta}$ for $\mathfrak{R}_r = 10$ dB, eight pulses, triangle matched filter response, and $P_{fa} = 10^{-3}$. Target energy is distributed equally in adjacent matched filter samples.

### 4.2.4 Comparison with Centroiding and Full ML Approaches

Since the derived $c$ and $\beta^2$ estimators use only the sum channel and $\hat{\eta}$ is a GML solution, the estimators are approximations to the full ML solution (i.e., jointly solving for the unknown parameters using the full probability distribution). Performance losses due to approximations may be significant. Here, a comparison of the proposed estimators is made with a

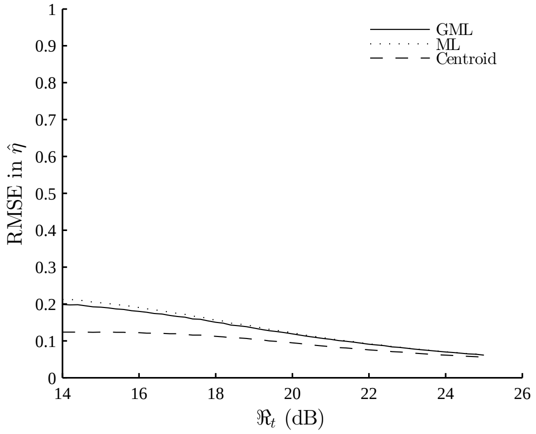

Figure 27: RMSE for $\hat{\eta}$ using the GML and ML solutions. The values $c$=0.5, $\eta$=0, $N$=10, $\sigma_s^2$=$\sigma_d^2$=1, and $P_{fa}$=$10^{-3}$ were used in all Monte Carlo trials. A triangle matched filter response is used.

full ML solution. The estimators described in Sections 4.2.2 and 4.2.3 will be denoted as GML solutions. A comparison with the $c$ and $\eta$ centroid estimators of [45], which uses the in-phase part sof the monopulse ratios, is also provided.

For a given set of parameters, 40,000 samples of (8)-(9) were generated using a triangular matched filter response, and the (RMSE) of the GML, ML, and centroid solutions for $\hat{\eta}$ and $\hat{c}$ were calculated. Samples that did not pass the ALLRT threshold of Section 4.2.1 were discarded. Newton's method was used to solve for $\hat{\eta}$ in the GML solution, with the initial starting point as the centroid solution of [45]. A Gauss-Newton approach was used to solve for the full ML solution, with a starting point as the GML solution. The full ML solution here assumes $\beta^2$ as an unknown parameter, which differs from the solution of [56] where $\beta^2$ is assumed to be a known parameter. RMSE for the $\hat{\eta}$ and $\hat{c}$ estimators is shown in Figures 27 and 28 for a target located at $\eta = 0$ (i.e., on-boresight) and $c = 0.5$ (i.e. target energy contained equally in adjacent samples). Notice that for the on-boresight target, the full ML solution provides no performance gains over the GML solution. In fact, the GML solution appears to slightly outperform the GML solution in this case. Also notice that the centroid estimator provides the best $\hat{\eta}$ performance for $\eta$=0; hence, the monopulse ratio provides excellent DOA estimation for targets near boresight. This result agrees with existing DOA estimation literature [8].

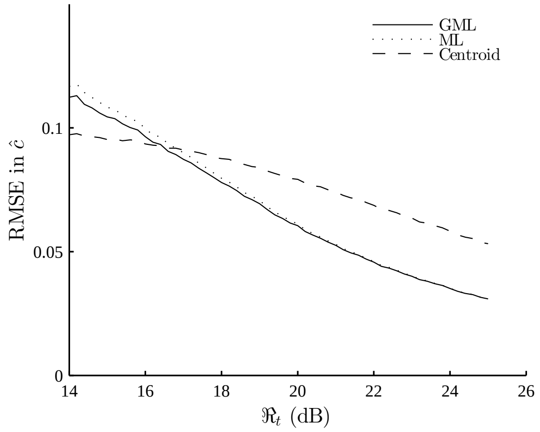

Figure 28: RMSE for $\hat{c}$ using the GML and ML solutions. The values $c$=0.5, $\eta$=0, $N$=10, $\sigma_s^2$=$\sigma_d^2$=1, and $P_{fa}$=$10^{-3}$ were used in all Monte Carlo trials. A triangle matched filter response is used.

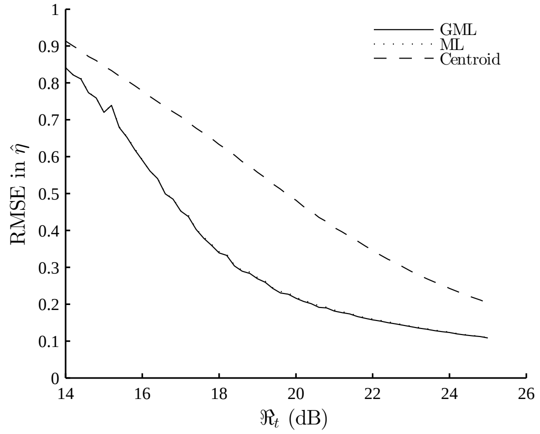

Figure 29: RMSE for $\hat{\eta}$ using the GML and ML solutions. The values $c$=0.5, $\eta$=1.5, $N$=10, $\sigma_s^2$=$\sigma_d^2$=1, and $P_{fa}$=$10^{-3}$ were used in all Monte Carlo trials. A triangle matched filter response is used.

RMSE for the $\hat{\eta}$ and $\hat{c}$ estimators is shown in Figures 29 and 30 for a target located at $\eta = 1.5$ (i.e., off-boresight) and $c = 0.5$. For a target located off-boresight, the ML solution provides notable performance gains over the GML solution only for $\hat{c}$. This result shows that target range information exists by jointly considering the sum *and* difference channel for off-foresight targets. Also, notice that $\hat{c}$ performance of the GML and centroid solutions are independent of the target location in $\eta$. This is expected since the AML and centroid estimator $\hat{c}$ only use the sum channel for estimation. Finally, the centroid estimator provides poor $\hat{\eta}$ performance compared to the GML and ML solutions for off-boresight targets.

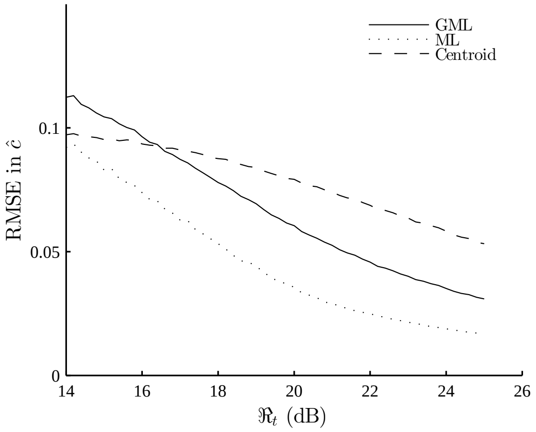

Figure 30: RMSE for $\hat{c}$ using the GML and ML solutions. The values $c$=0.5, $\eta$=1.5, $N$=10, $\sigma_s^2$=$\sigma_d^2$=1, and $P_{fa}$=$10^{-3}$ were used in all Monte Carlo trials. A triangle matched filter response is used.

The Gauss-Newton procedure used for the full ML solution had divergence problems for off-boresight, low SNR cases. With $\Re_t$ = 14 dB and $\eta$=1.5, a divergence rate of 14 percent was observed. At $\Re_t$ = 20 dB, this divergence rate decreased to 1 percent and continued decreasing with increasing $\Re_t$. For the on-boresight case, no divergence issues were observed. Also, with $c$ = 0,1, no divergence issues were observed. No divergence issues were observed with the GML solution.

Recalling that $c$ has a value between zero and one, a sub-bin $\hat{c}$ can provide range estimation accuracy of less than one-tenth of a range bin, as shown in Figure 28. The value of this precision range estimation depends upon the application of such processing. For instance, as shown in [46], overly precise range estimates can lead to complications with the tracking algorithms. Since the main focus of monopulse systems is DOA estimation, we proceed with the GML solution.

## *4.3 Variance Reporting*

Estimators and their associated CRLBs are provided in Section 4.2. In this Section, the generalized Cramér-Rao lower bound (GCRLB), which is the CRLB (i.e., (73) and (77)) evaluated at estimated parameters, is investigated as a variance report for the estimators provided in Section 4.2. Error variance reporting is particularly important in order to facilitate the use by data fusion algorithms such as the Kalman filter. In order to determine the usefulness of the GCRLB as a variance report, the average normalized estimation error squared (ANEES) is defined as

$$ANEES_{\hat{\theta}} = E\left[\frac{(\hat{\theta}-\theta)^2}{\sigma_{\theta}^2}\right], \tag{84}$$

where $\hat{\theta}$ is the estimator of interest. As discussed in [3], ANEES is used to study the variance consistency and statistical efficiency of an estimator. Statistical efficiency of an unbiased estimator is achieved when the actual errors achieve the CRLB. Variance consistency of a parameter estimate $\hat{\theta}$ and variance report is achieved when the reported error variance of an estimator accurately reflect the actual error variance. In terms of this work, variance consistency is investigated using (84) with $\sigma_{\theta}^2$ = GCRLB (CRLB evaluated at parameter estimates), and statistical efficiency with $\sigma_{\theta}^2$ = CRLB (evaluated at the true parameter values). ANEES values near one are desired since they correspond to statistically efficient and consistent estimators.

ANEES for the GML estimators of $c$ and $\eta$ were computed using Monte Carlo simulations. For a given set of parameters, 100,000 samples of (8)-(9) were generated using a triangular matched filter response, and the ANEES were were calculated using the CRLBs given by (73) and (77). True parameter values were used to evaluate statistical efficiency and estimated parameter values were used to evaluate variance consistency.[2] Samples that did not pass the ALLRT threshold of Section 4.2.1 were discarded. For all Monte Carlo simulations, $P_{fa} = 10^{-3}$ and $\sigma_s^2 = \sigma_d^2 = 1$.

ANEES for $\hat{c}$ are provided in Figures 31 and 32 for $c$=0.5 and $c$=1, respectively. For slightly easier interpretation, the square root of ANEES is shown to provide normalized errors in a “standard deviation” scale instead of “variance” scale. Notice that the GCRLB provides a good variance report for all values of $\mathfrak{R}_t$ and $c$=0.5. However, for $c$=1, the GCRLB requires $\mathfrak{R}_t \geq 15$ dB to achieve variance consistency. For low $\mathfrak{R}_t$, the $\hat{c}$ appears to provide estimation errors lower than the CRLB. This is because the CRLB is derived

---

[2] For (73) to exist, $\frac{\partial r_1}{\partial c}$ and $\frac{\partial r_2}{\partial c}$ must also exist. For waveforms used in practice, these partials will always exist otherwise the waveform is not physically realizable. However, for the triangular matched filter response often used in the literature and in our analysis, $\frac{\partial r_1}{\partial c}$ and $\frac{\partial r_2}{\partial c}$ are undefined for $c$=0 and 1. This was also noted in [56]. For simulation purposes in this work, the values $\frac{\partial r_1}{\partial c}$=-1 and $\frac{\partial r_2}{\partial c}$=1 are used with the triangle matched filter response, regardless of the estimated or actual value of $c$.

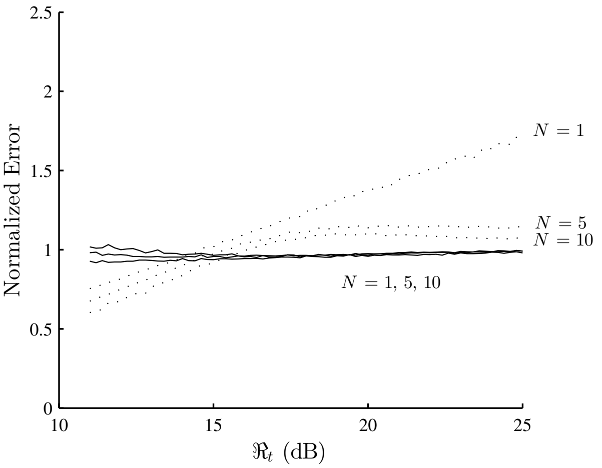

Figure 31: Square root of ANEES for $\hat{c}$. Solid lines represent ANEES calculated with the GCRLB (for variance consistency) and dotted lines represent ANEES calculated with the CRLB (for statistical efficiency). For the Monte Carlo trials, $c = 0.5$ and number of pulses is equal to 1, 5, and 10.

using the full distribution of the observations, while the results shown in Figures 31 and 32 are conditioned on an ALLRT detection. The detection process changes the support of the distribution function, which is significant in situations with low probability of detection (i.e., low $\Re_t$). For a single pulse, the estimators do not approach efficiency with increasing $\Re_t$. In fact, the ANEES appears go grow unboundedly with $\Re_t$. This is an expected result, since many properties of ML estimation are asymptotic in nature. Interestingly, the GCRLB approaches variance consistency for a single pulse. However, with five and ten pulses, the statistical efficienty appears to "level off" with increasing $\Re_t$.

ANEES for $\hat{\eta}$ are provided in Figures 33, 34, and 35 for $\eta = 0$, 1, and 1.5, respectively. In each figure, target energy is contained equally across adjacent samples. For targets located near $\eta = 0$, the GCRLB appears to be a consistent estimator. However, increasing $\eta$ results in a higher $\Re_t$ required for consistency of the GCRLB. For $\eta = 1$, $\Re_t \approx 17$ dB is required for consistency, and for $\eta = 1.5$, $\Re_t \approx 20$ dB is required. For off-boresight targets, the consistency of the error report gets worse with a higher number of pulses and low $\Re_t$. Similar to $\hat{c}$, $\hat{\eta}$ does not appear to approach statistical efficiency for a single pulse; the ANEES grows unboundedly in this case. However, for five and ten pulses the ANEES for $\hat{\eta}$ appears to "level off" around $\Re_t = 20$ dB, and approach efficiency as the number of pulses

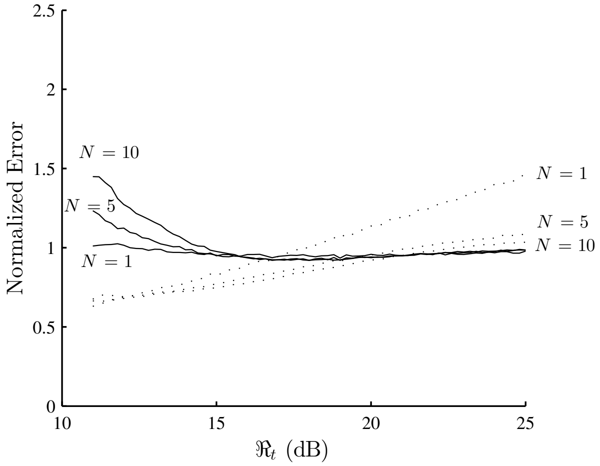

Figure 32: Square root of ANEES for $\hat{c}$. Solid lines represent ANEES calculated with the GCLRB (for variance consistency) and dotted lines represent ANEES calculated with the CRLB (for statistical efficiency). For the Monte Carlo trials, $c = 1$ and number of pulses is equal to 1, 5, and 10.

increases.

Figure 36 provides ANEES for $\eta = 1.5$, with target energy completely contained in a single sample. As shown, with target energy contained in a single matched filter sample the required $\Re_t$ for a consistent estimator is decreased to 16 dB as opposed to 20 dB. With target energy contained in a single sample, the variance consistency and efficiency of $\hat{\eta}$ becomes more desirable.

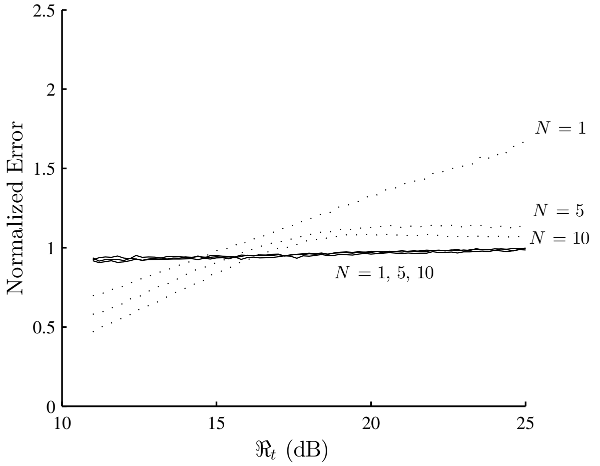

Figure 33: Square root of ANEES for $\hat{\eta}$. Solid lines represent ANEES calculated with the GCRLB (for variance consistency) and dotted lines represent ANEES calculated with the CRLB (for statistical efficiency). For the Monte Carlo trials, $c = 0.5$, $\eta$=0, and number of pulses is equal to 1, 5, and 10.

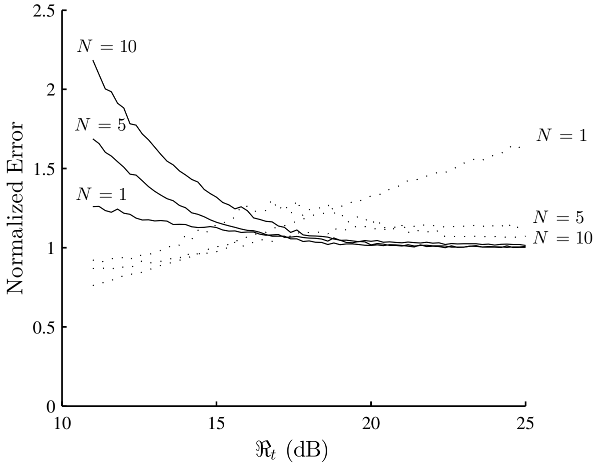

Figure 34: Square root of ANEES for $\hat{\eta}$. Solid lines represent ANEES calculated with the GCRLB (for variance consistency) and dotted lines represent ANEES calculated with the CRLB (for statistical efficiency). For the Monte Carlo trials, $c = 0.5$, $\eta$=1, and number of pulses is equal to 1, 5, and 10.

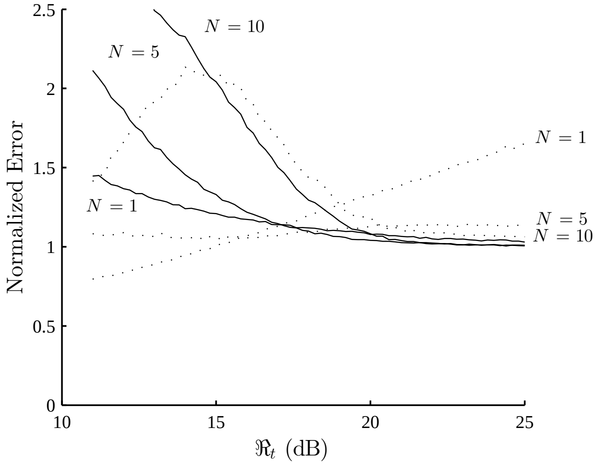

Figure 35: Square root of ANEES for $\hat{\eta}$. Solid lines represent ANEES calculated with the GCRLB (for variance consistency) and dotted lines represent ANEES calculated with the CRLB (for statistical efficiency). For the Monte Carlo trials, $c = 0.5$, $\eta$=1.5, and number of pulses is equal to 1, 5, and 10.

Of practical importance is the accuracy benefit of the processing described in this work as it relates to existing approaches. By inspection of Figure 35, with ten pulses, $\Re_t = 20$ dB, and $c = 0.5$, the proposed $\hat{\eta}$ is near statistical efficiency and consistency. By inspection of Figure 27, near $\Re_t$=20 dB the estimators described in this chapter outperform the centroiding technique of [45] by a factor close to two in RMSE of $\hat{\eta}$. Although the analysis in

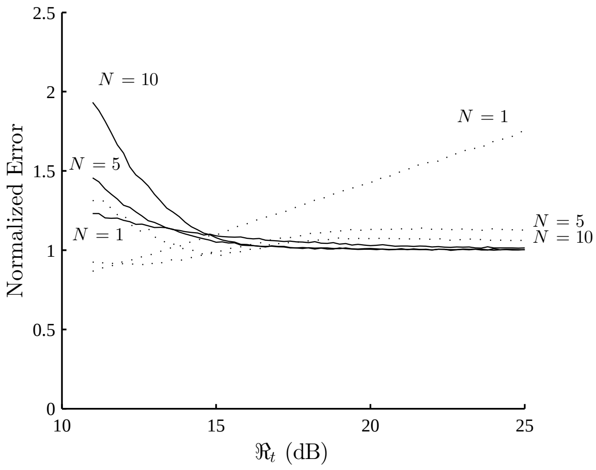

Figure 36: Square root of ANEES for $\hat{\eta}$. Solid lines represent ANEES calculated with the GCRLB (for variance consistency) and dotted lines represent ANEES calculated with the CRLB (for statistical efficiency). For the Monte Carlo trials, $c = 1$, $\eta$=1.5, and number of pulses is equal to 1, 5, and 10.

Figure 27 for $c$=0,1 is not provided in the manuscript, a performance increase of 25 percent was found for this case.

The same Monte Carlo simulations were performed using a sinc matched filter response instead of a triangle matched filter response. Similar results were found for the sinc matched filter response, but are not provided in the manuscript.

## *4.4 Concluding Remarks*

Amplitude comparison monopulse systems use a simultaneous lobing technique to provide sub beam-width localization of a target. In practice, sampled versions of monopulse signals are used for processing, and bin-straddling is an unavoidable consequence. Traditional radar literature treats bin-straddling as an undesired loss in SNR, and treats each sample individually. However, sample rates often used in practice result in multiple adjacent samples with target energy. Those samples are correlated and, by treating each sample individually, traditional monopulse processing ignores the correlation.

Here, we systematically incorporated sampling into the monopulse signal model, and derived GML estimates of target range and DOA. Since data fusion algorithms, such as the Kalman filter, require an estimated error variance on parameter estimates, we proposed the GCRLB, CRLB evaluated at parameter estimates, as an error report. CRLBs for the unknown target localization parameters were provided in closed form. The statistical efficiency and consistency of the estimators were shown through Monte Carlo simulations, and required target SNR levels were provided. Interesting findings include:

- The proposed estimators require knowledge of the transmitted waveform. Given an estimate for target range, target strength estimation is a closed-form expression. For a triangular matched filter response, a closed-form expression for range estimation was provided. For more complex waveforms, numerical approaches are likely needed to arrive at range estimates. Given target range and strength estimates, DOA estimation is equivalent to solving a third order polynomial.

- A new closed-form CRLB for target DOA, which assumes target strength and target range as unknown parameters, was provided. Using the CRLB for target DOA, bin-spreading was shown to result in a direct loss in $\mathfrak{R}_r$. For a triangle matched filter response, worst case loss is 0.5.

- The proposed estimators are an approximation to a full ML solution. A comparison was made with the full ML solution, and no performance losses were found for target DOA estimation. However, target range estimation can be improved with the full ML solution. Using a Gauss-Newton approach, the full ML solution had divergence issues in some situations.

- ANEES was used to evaluate variance consistency and efficiency of the estimators. In general, statistical efficiency and consistency of the estimators improved with an increasing number of pulses and increasing $\mathfrak{R}_t$. Considering all the cases described in this work, variance consistency of the estimators are guaranteed for $\mathfrak{R}_t$ greater than 19 dB. For some easy situations, lower values of $\mathfrak{R}_t$ are required. The estimators approach statistical efficency with an increasing number of pulses, and $\mathfrak{R}_t \geq 20$ dB.

- For off-boresight targets, the proposed target DOA estimator improves upon the approach of [45] by up to a factor of two in RMSE.

Future work includes extension to joint estimation of both horizontal and azimuth DOAs.

Such work may prove fruitful since, as discussed in [52], horizontal and vertical DOA estimates can be correlated. In-depth studies into the properties of $\hat{\beta}^2$ and the statistical efficiency/consistency of the estimator are left for future work. Of practical interest is the amount of performance degradation in the presence of unmodeled disturbances. Examples of unmodeled disturbances include multiple targets in the same resolution cell, and clutter. Investigation into these potential performance degradations is left for future work. Finally, a formal study of the GCRLB, in which parameter estimates are used in the functional form of the CRLB, is left for future work.

# CHAPTER V

# RADAR TRACKING OF MANEUVERING TARGETS

The problem of tracking maneuvering targets has been studied extensively. The interacting multiple model (IMM) algorithm is considered to be a best in-class technique for tracking maneuvering targets, when computational aspects are considered [4]. The IMM estimator assumes that target motion follows one of a finite set of motion models, and that the transitioning between models behaves as a Markov process. These models interact in the IMM estimator through a process called "mixing," which is governed by the mode probabilities and the mode switching probabilities. However, in order to have reliable tracking, motion models that accurately represent target maneuvers must be used [40]. Furthermore, an appropriate set of motion models is needed to prevent unneccessary "competition" among models [31].

Using track state estimates, agile beam radars are able to adaptively schedule track revisits once positional uncertainty reaches a specified fraction of the main beam. It is well accepted that the use of adaptive revisit calculations along with an IMM estimator achieves significant reductions in total radar time, while maintaining a maximum allowed track loss ([6, 11]). An IMM estimator that includes adaptive revisit calculations is able to achieve longer average revisit periods through kinematic modeling represenative of target motion, thus reducing radar time and energy. A reduction in radar time and energy for each track is valuable since more objects can be tracked, and more resources are available for search and acquisition modes.

In practice, radars choose from multiple waveforms so that the waveform energy can be coordinated with the tracking algorithm. With a target strength estimate in hand, a reasonable criterion for selection of a waveform is a desired signal-to-noise (SNR) level; this is referred to as the nominal tracking SNR. Typically, a radar will transmit at peak power for a certain pulsewidth and number of pulses. Therefore, higher energy waveforms equate to longer pulsewidths or more pulses. In general, a higher energy waveform will have higher detection probability and more accurate measurements, facilitating more accurate estimation and longer revisit times. However, these higher energy waveforms cost more energy, potentially impacting duty cycle considerations. Therefore, a tradeoff exists between radar time and radar energy in the selection of a radar waveform and an overall nominal tracking SNR level.

The first and second Benchmark tracking problems developed by Blair et. al. ([12, 13]) provided a standard problem for comparing radar tracker and scheduler algorithms for typical ship defense applications. Nearly all solutions used adaptive waveform selection, adaptive revisit calculations, and multiple model filtering methods ([6, 30]). Many solutions to the second Benchmark problem choose to operate at an arbitrary SNR level, usually around 14.5-16 dB, with little attention devoted to the question of an optimal tracking SNR level [6, 30]. The authors in [48] investigated optimal tracking SNR levels using a simple phased array radar model. The authors claim that minimizing an optimization function called "radar load" maximizes the total number of possible maintained tracks, and they found an optimal tracking SNR level of 16 dB. However, the authors of [48] use a single kinematic model Kalman filter; the effect of an IMM estimator on optimal tracking SNR was not investigated. Furthermore, their algorithms were not implemented for the first or second Benchmark tracking problems.

In this chapter, optimal SNR levels for tracking with an IMM estimator are investigated using a high-fidelity radar tracking simulation similar to that of the first and second Benchmark problems, and those results are compared to results in existing literature. Upon selection of an IMM for tracking highly maneuverable targets, tradeoffs in the nominal tracking SNR levels are studied in more depth than in the existing literature In this chapter, the radar management operating curve (RMOC) is developed and can be used to characterize the fundamental tradeoff of radar time and energy, as it relates to the selection of an operating SNR. Some of this chapter follows our expositions in [21] and [22].

## *5.1 Target and Radar Models*

Before the discussion of IMM estimators, a description of the testing environment is provided. Testing was performed using the MIMO Radar Benchmark [18]. The simulation software includes a 1 MW maximum power, 4 GHz phased array (*i.e.*, agile beam) radar using amplitude comparison monopulse. Radar detection and signal processing is performed on simulation-generated I&Q voltages in the sum, azimuth difference, and elevation difference channels, corrupted by white Gaussian noise errors. The radar model of the simulation program accepts time, range, angles, pulsewidth, and a detection threshold on observed SNR for a scheduled radar track dwell. Pulsewidths available to the sceduling algorithm are arranged in 3 dB steps with a total dynamic range of 54 dB. The largest pulsewidth is 1 ms and the smallest pulsewidth is 7 ns.[1] A probability of a false alarm equal to $10^{-5}$ in a bin (range resolution cell) was used to set the detection threshold for all waveforms in this study.

Upon detection of target presence using conventional single-bin detection processing, range and sine space angles (r-u-v coordinates) are reported for each range bin detection

$$r = \sqrt{x^2 + y^2 + z^2}, \tag{85}$$

$$u = \frac{x}{r}, \tag{86}$$

$$v = \frac{y}{r}, \tag{87}$$

where DOA is computed with conventional monopulse processing (i.e., the in-phase part of the monopulse ratio), and then converted into $u$ and $v$ space through the monopulse error slope. In practice, the reported error variances for sine space estimates at each detected range bin are functions of observed SNR and the monopulse error slope

$$\sigma_{\hat{u}}^2 = \frac{\theta_B^2}{k_x^2} \frac{1}{2\mathfrak{R}_o} \left[ \frac{\sigma_{du}^2}{\sigma_s^2} + y_{Iu}^2 \right], \tag{88}$$

$$\sigma_{\hat{v}}^2 = \frac{\theta_B^2}{k_y^2} \frac{1}{2\mathfrak{R}_o} \left[ \frac{\sigma_{dv}^2}{\sigma_s^2} + y_{Iv}^2 \right], \tag{89}$$

---

[1] Pulse widths in the range of nanoseconds are probably not feasible in a real radar system. However, for the purposes of this study, we needed a large dynamic range to ensure a desired SNR level can be achieved.

where $k_x$ and $k_y$ are the monopulse error slopes for azimuth and vertical, respectively, $\mathfrak{R}_o$ is the observed signal-to-noise ratio, $\theta_B$ is the 3 dB beamwidth of the main beam, $\sigma_s^2$ is the noise power in the sum channel, $\sigma_{du}^2$ and $\sigma_{dv}^2$ are noise powers in the difference channels, and $y_{Iu}$ and $y_{Iv}$ are the in-phase parts of the observed monopulse ratios. The main beam in the radar model has a 3 dB beamwidth of 1.9 degrees at broadside of the array face. Finally, in the simulation, range bin straddling is modeled as being across a maximum of two range bins per target. For detections in two adjacent range bins, centroid processing as in [45] was used to create a single measurement. The reported sub-bin range is an observed-SNR weighted centroid of two adjacent range bins, and the reported variance is given by

$$\sigma_{\hat{r}}^2 = \frac{(\Delta r)^2}{2\mathfrak{R}_{om}}, \tag{90}$$

where $\mathfrak{R}_{om}$ is the maximum SNR of the two adjacent range bins and $\Delta r$ is the range resolution of the transmitted waveform. If a single range bin exceeds a threshold, then the reported range variance is the variance of a uniform distribution corresponding to the size of a range bin. All track waveforms available to the radar have a range resolution of 15 meters, and a range window of 3000 meters. For detections in two adjacent range bins, the reported angle measurement is also an observed SNR weighted centroid of the two adjacent angle measurements. Notice that reported variances of the range and angle measurements decrease with increasing observed SNR.

The target trajectory is depicted in Figure 37. The trajectory is shown in the East-North-Up coordinate frame relative to the sensor. The target depicted in Figure 37 makes three coordinated turns at a constant speed of 250 m/s: two $2g$ (i.e., two times gravity) turns and one $4g$ turn. After the turns, the target throttles to a speed of 400 m/s and performs a $6g$ vertical maneuver to reach an altitude of 9188 meters (about 30000 ft). The vertical maneuvers were generated using high fidelity trajectory generation software for manned aircraft.

## *5.2 Selection of an IMM Estimator*

Nearly coordinated turn (NCT) models are commonly used in the tracking of air targets. These models assume a target is moving with nearly constant speed, and a constant turn

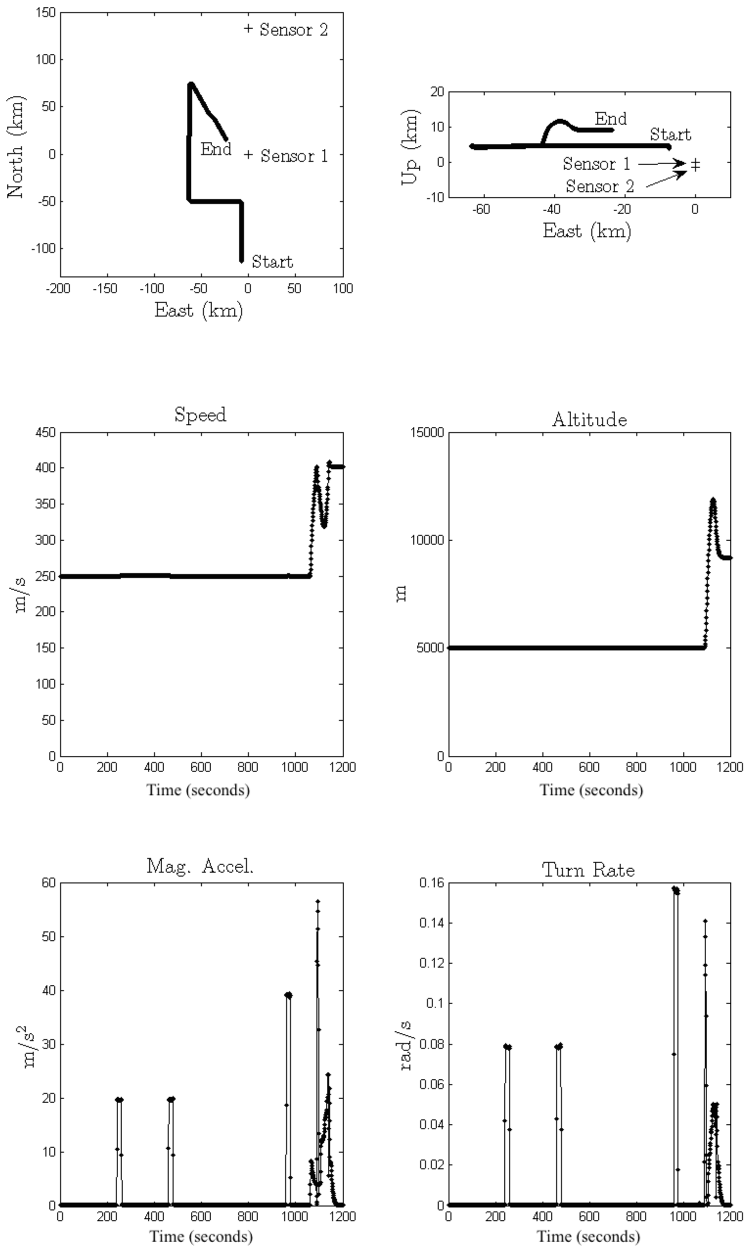

Figure 37: Target trajectory.

rate. A specific type of NCT model is the horizontal nearly coordinated turn model, which assumes that targets perform coordinated turns in the x-y horizontal plane. Typically, in conjunction with NCT, motion in the z-axis is decoupled from this horizontal motion and modeled with nearly constant velocity, resulting in a seven element state vector. This kinematic model has been successfully utilized in an IMM estimator for the application of civilian air traffic surveillance [49]. As an alternative, 3D turn models can be used.

These models relax the assumption that coordinated turns are constrained to the horizontal plane. Using a 3D turn model, the turn rate vector is typically assumed to be orthogonal to the velocity vector. As a result, the acceleration vector is also orthogonal to the velocity vector, which defines the "turn plane" of the maneuver. This model has been sucessfully used in an IMM estimator for the Benchmark problem of tracking agile targets [11]. This model has also been used with a kinematic constraint as a pseudomeasurement to enhance tracking performance during coordinated turns [51, 1]. Although the authors in [51] compare performance of the 3D turn model with the horizontal maneuver model of [20], a comparson with the NCT model of [49] is not provided.

Many useful kinematic models that describe target motion have state vectors of differing dimension. A conventional approach addressing the state vectors of differing dimension in the mixing is augmenting extra elements with zeros and perform the standard mixing. However, this approach introduces a bias in the mixed estimate [4]. Recently, an unbiased mixing procedure was developed for the case of two modes [55], which was used in an IMM estimator to predict the impact point of ballistic missiles. For the case of an IMM estimator with NCT and NCV models, the unbiased mixing procedure can be useful since the turn rate is an extra element in the state vector of the NCT model. However, for this investigation three models are used in the IMM estimator.

In this section, two IMM filters with three kinematic models for tracking maneuvering air targets are designed and their performances compared. One IMM estimator includes a horizontal coordinated turn model similar to [49], and the other IMM estimator includes a 3D coordinated turn mode [51]. An extension of the unbiased mixing procedure described in [55] is used for the case of a three model IMM. The MIMO Radar Benchmark [18] was used to compare the performance of these filters. This section closely follows our description in [21].

### 5.2.1 Kinematic Modeling

As discussed in Section 2.2.1, the discrete Kalman filtering equations require state dynamic equations in the form of (14). This section discusses kinematic models to be used in candidate IMM estimators. To describe the kinematic models, the discrete time state dynamic equations are presented along with process noise parameters. For each of these descriptions, let $\Delta t$ denote the time between observations, and $k$ denote the time index.

#### *5.2.1.1 Nearly Constant Velocity Model*

The Nearly Constant Velocity (NCV) model uses a six-dimensional state vector with position and velocity elements. The discrete time state equations for the NCV model can be written as

$$\mathbf{x}(k+1) = \mathbf{F}(k)\mathbf{x}(k) + \mathbf{w}(k), \tag{91}$$

where

$$\mathbf{x}(k) = \begin{bmatrix} x(k) & \dot{x}(k) & y(k) & \dot{y}(k) & z(k) & \dot{z}(k) \end{bmatrix}^T, \tag{92}$$

$$\mathbf{F}(k) = \begin{bmatrix} 1 & \Delta t(k) & 0 & 0 & 0 & 0 \\ 0 & 1 & 0 & 0 & 0 & 0 \\ 0 & 0 & 1 & \Delta t(k) & 0 & 0 \\ 0 & 0 & 0 & 1 & 0 & 0 \\ 0 & 0 & 0 & 0 & 1 & \Delta t(k) \\ 0 & 0 & 0 & 0 & 0 & 1 \end{bmatrix}, \tag{93}$$

$$\mathbf{w}(k) \sim \mathscr{N}\left(\mathbf{0}, \mathbf{G}(k) \begin{bmatrix} \sigma_{a_x}^2 & 0 & 0 \\ 0 & \sigma_{a_y}^2 & 0 \\ 0 & 0 & \sigma_{a_z}^2 \end{bmatrix} \mathbf{G}(k)^T \right), \tag{94}$$

with

$$\mathbf{G}(k) = \begin{bmatrix} 0.5\Delta t(k)^2 & 0 & 0 \\ \Delta t(k) & 0 & 0 \\ 0 & 0.5\Delta t(k)^2 & 0 \\ 0 & \Delta t(k) & 0 \\ 0 & 0 & 0.5\Delta t(k)^2 \\ 0 & 0 & \Delta t(k) \end{bmatrix}. \tag{95}$$

The $\sigma_{a_x}$, $\sigma_{a_y}$, and $\sigma_{a_z}$ are design parameters, which have the units of acceleration. Notice that the DWN process noise model, as described in Section 2.2.1, is used.

#### *5.2.1.2 Horizontal Nearly Coordinated Turn Model*

The Horizontal Nearly Coordinated Turn (HNCT) model uses a seven dimensional state vector with position elements, velocity elements, and an element for turn rate, $\Omega$. An additive DWN process noise model is assumed. The nonlinear state equations for the HNCT model can be written as

$$\mathbf{x}(k+1) = \mathbf{f}\left[\mathbf{x}(k)\right] + \mathbf{w}(k), \tag{96}$$

or, with the terms written out explicitly for sampling interval $\Delta t_k$,

$$\mathbf{x}(k) = \begin{bmatrix} x(k) & \dot{x}(k) & y(k) & \dot{y}(k) & z(k) & \dot{z}(k) & \Omega(k) \end{bmatrix}^T, \tag{97}$$

$$\mathbf{f}\left[\mathbf{x}(k)\right] = \left[\begin{array}{c|ccc} \mathbf{A}(k) & & \mathbf{0} & \\ \hline & 1 & \Delta t(k) & 0 \\ \mathbf{0} & 0 & 1 & 0 \\ & 0 & 0 & 1 \end{array}\right] \mathbf{x}(k), \tag{98}$$

with

$$\mathbf{A}(k) = \begin{bmatrix} 1 & \frac{\sin(\Omega(k)\Delta t(k))}{\Omega(k)} & 0 & -\frac{1-\cos(\Omega(k)\Delta t(k))}{\Omega(k)} \\ 0 & \cos(\Omega(k)\Delta t(k)) & 0 & -\sin(\Omega(k)\Delta t(k)) \\ 0 & \frac{1-\cos(\Omega(k)\Delta t(k))}{\Omega(k)} & 1 & \frac{\sin(\Omega(k)\Delta t(k))}{\Omega(k)} \\ 0 & \sin(\Omega(k)\Delta t(k)) & 0 & \cos(\Omega(k)\Delta t(k)), \end{bmatrix} \tag{99}$$

where $\mathbf{w}(k)$ is a seven-dimensional zero mean Gaussian random variable

$$\mathbf{w}(k) \sim \mathscr{N}\left(\mathbf{0}, \mathbf{G}(k)\begin{bmatrix} \sigma_{a_x}^2 & 0 & 0 & 0 \\ 0 & \sigma_{a_y}^2 & 0 & 0 \\ 0 & 0 & \sigma_{a_z}^2 & 0 \\ 0 & 0 & 0 & \sigma_{\Omega}^2 \end{bmatrix}\mathbf{G}(k)^T\right), \tag{100}$$

with

$$\mathbf{G}(k) = \begin{bmatrix} \frac{\Delta t(k)^2}{2} & 0 & 0 & 0 \\ \Delta t(k) & 0 & 0 & 0 \\ 0 & \frac{\Delta t(k)^2}{2} & 0 & 0 \\ 0 & \Delta t(k) & 0 & 0 \\ 0 & 0 & \frac{\Delta t(k)^2}{2} & 0 \\ 0 & 0 & \Delta t(k) & 0 \\ 0 & 0 & 0 & \Delta t(k) \end{bmatrix}. \tag{101}$$

The $\sigma_{a_x}$, $\sigma_{a_y}$, and $\sigma_{a_z}$ are design parameters, which have units of acceleration. The process noise standard deviation for $\Omega$, $\sigma_{\Omega}$, is also a design parameter and has units of rad/s$^2$. Notice that the coordinated turn is expected to occur in the x-y plane.[1]

#### *5.2.1.3 3D Nearly Coordinated Turn Model*

The 3D Nearly Coordinated Turn (3DNCT) model uses a nine-dimensional state vector with position, velocity, and acceleration elements [51, 40]. An additive discrete-time white process noise model is assumed in the position and velocity components. The state equations for the 3DNCT model can be written as

$$\mathbf{x}(k+1) = \mathbf{F}(k)\mathbf{x}(k) + \mathbf{w}(k), \tag{102}$$

---

[1] According to [35] even high performance fighters execute maneuvers that are NCT in the horizontal plane and these can be decoupled from their vertical maneuvers.

or, with the terms written out explicitly for sampling interval $\Delta t(k)$,

$$\mathbf{x}(k) = [x(k) \quad \dot{x}(k) \quad \ddot{x}(k) \quad y(k) \quad \dot{y}(k) \quad \ddot{y}(k) \quad z(k) \quad \dot{z}(k) \quad \ddot{z}(k)]^T, \tag{103}$$

$$\mathbf{F}(k) = \begin{bmatrix} \mathbf{B}(k) & \mathbf{0} & \mathbf{0} \\ \mathbf{0} & \mathbf{B}(k) & \mathbf{0} \\ \mathbf{0} & \mathbf{0} & \mathbf{B}(k) \end{bmatrix}, \tag{104}$$

with

$$\mathbf{B}(k) = \begin{bmatrix} 1 & \frac{\sin(\omega(k)\Delta t(k))}{\omega(k)} & \frac{1-\cos(\omega(k)\Delta t(k))}{\omega(k)^2} \\ 0 & \cos(\omega(k)\Delta t(k)) & \frac{\sin(\omega(k)\Delta t(k))}{\omega(k)} \\ 0 & -\frac{\sin(\omega(k)\Delta t(k))}{\omega(k)} & \cos(\omega(k)\Delta t(k)) \end{bmatrix}, \tag{105}$$

where $\omega(k)$ is the magnitude of the turn rate assumed to be given by

$$\omega(k) = \frac{\sqrt{\ddot{x}(k)^2 + \ddot{y}(k)^2 + \ddot{z}(k)^2}}{\sqrt{\dot{x}(k)^2 + \dot{y}(k)^2 + \dot{z}(k)^2}}. \tag{106}$$

The process noise, $\mathbf{w}(k)$ is a nine-dimensional zero mean Gaussian random vector

$$\mathbf{w}(k) \sim \mathscr{N}\left(\mathbf{0}, \mathbf{G}(k) \begin{bmatrix} \sigma_{j_x}^2 & 0 & 0 \\ 0 & \sigma_{j_y}^2 & 0 \\ 0 & 0 & \sigma_{j_z}^2 \end{bmatrix} \mathbf{G}(k)^T\right), \tag{107}$$

with

$$\mathbf{G}(k) = \begin{bmatrix} \frac{\Delta t(k)^3}{6} & 0 & 0 \\ \frac{\Delta t(k)^2}{2} & 0 & 0 \\ \Delta t(k) & 0 & 0 \\ 0 & \frac{\Delta t(k)^3}{6} & 0 \\ 0 & \frac{\Delta t(k)^2}{2} & 0 \\ 0 & \Delta t(k) & 0 \\ 0 & 0 & \frac{\Delta t(k)^3}{6} \\ 0 & 0 & \frac{\Delta t(k)^2}{2} \\ 0 & 0 & \Delta t(k) \end{bmatrix}, \tag{108}$$

where $\sigma_{j_x}$, $\sigma_{j_y}$, and $\sigma_{j_z}$ are design parameters, which have units of jerk, m/s$^3$.

#### *5.2.1.4 Kinematic Constraint for Constant Speed Targets*

During a coordinated turn, aircraft speed can be modeled as nearly constant, since the acceleration vector is almost orthogonal to the velocity vector. As a result, a kinematic constraint (KC) for constant speed maneuvers can be utilized as additional information to reduce the estimation errors due to time-varying accelerations [51, 1]. If the tracking filter has velocity and acceleration estimates, the KC can be incorporated as a pseudomeasurement. The pseudomeasurement equation can be written as

$$\frac{\mathbf{v}^T\mathbf{a}}{||\mathbf{v}||_2} + \mu(k) = 0, \tag{109}$$

where

$$\mathbf{v} = \left[\begin{array}{ccc} \hat{\dot{x}} & \hat{\dot{y}} & \hat{\dot{z}} \end{array}\right]^T \quad \text{and} \quad \mathbf{a} = \left[\begin{array}{ccc} \hat{\ddot{x}} & \hat{\ddot{y}} & \hat{\ddot{z}} \end{array}\right]^T, \tag{110}$$

and $\mu(k) \sim \mathscr{N}(0, r(k))$ is a pseudomeasurement noise term to account for uncertainty in both the velocity estimate and the KC. Since initial velocity estimates may be poor, the variance for the pseudomeasurement noise term is chosen to have the form

$$r(k) = r_1(\delta)^k + r_0, \tag{111}$$

where $0<\delta<1$, $r_1$ is chosen large for initialization, and $r_0$ is chosen for steady state conditions. Given a state vector estimate of the form

$$\hat{\mathbf{x}} = \left[\begin{array}{ccccccccc} \hat{x} & \hat{\dot{x}} & \hat{\ddot{x}} & \hat{y} & \hat{\dot{y}} & \hat{\ddot{y}} & \hat{z} & \hat{\dot{z}} & \hat{\ddot{z}} \end{array}\right]^T, \tag{112}$$

with an associated error covariance matrix, $\mathbf{P}$, then the filtering equations employing the KC are given by [51]

$$\hat{\mathbf{x}}^c = [\mathbf{I} - \mathbf{k}\mathbf{c}^T]\hat{\mathbf{x}} \quad \text{and} \quad \mathbf{P}^c = [\mathbf{I} - \mathbf{k}\mathbf{c}^T]\mathbf{P}, \tag{113}$$

where

$$\mathbf{k} = \mathbf{P}\mathbf{c}[\mathbf{c}^T\mathbf{P}\mathbf{c} + r]^{-1}, \tag{114}$$

$$\mathbf{c} = \frac{1}{||\mathbf{v}||^2}\left[\begin{array}{ccccccccc} 0 & 0 & \hat{\dot{x}} & 0 & 0 & \hat{\dot{y}} & 0 & 0 & \hat{\dot{z}} \end{array}\right]^T. \tag{115}$$

| **IMM-CVCV** | |
|---|---|
| $\pi_{ij} = \begin{bmatrix} 0.75 & 0.25 \\ 0.25 & 0.75 \end{bmatrix}$ | |
| $\mu_j(0) = \begin{bmatrix} 0.9 & 0.1 \end{bmatrix}^T$ | |
| **CV1** | **CV2** |
| $\sigma_x = 3$ m/s$^2$ | $\sigma_x = 30$ m/s$^2$ |
| $\sigma_y = 3$ m/s$^2$ | $\sigma_y = 30$ m/s$^2$ |
| $\sigma_z = 3$ m/s$^2$ | $\sigma_z = 30$ m/s$^2$ |

Table 6: Design parameters for IMM-CVCV.

### 5.2.2 Candidate IMM Filters

In this section, three candidate IMM filters are designed using the kinematic models described in the previous section. For the IMM design parameters, recall from Section 2.2 that $p_{ij}$ are the Markov transition probabilities from (29), and $\mu_0$ are the initial mode probabilities. In some IMM filters, the unbiased mixing procedure described in [55] is needed. The approach of [55] was extended from a two mode IMM to a three mode IMM, and the description is provided in Appendix C.

#### *5.2.2.1 IMM-CVCV*

This section describes an IMM estimator that is used as a performance "baseline" since it does not include a coordinated turn model. Unmodeled dynamics are instead included in process noise. This IMM estimator includes two models: two CV models (actually NCV but the N is dropped for the sake of shorter acronyms). The first CV model, CV1, has small process noise and should accurately estimate the target state when the target is not maneuvering. The second CV model, CV2, has large process noise and should accurately estimate the target state at the onset/termination of maneuvers. Design parameters for this IMM estimator are provided in Table 6.

#### *5.2.2.2 IMM-CVCVHCT*

The second IMM filter is similar to the IMM used in [49]. This IMM is designed with three models: two CV models and an HCT model. The first CV model, CV1, will have small process noise and should be able to accurately estimate the target state when the target is not maneuvering. The second CV model, CV2, has large process noise and should accurately estimate the target state at the onset/termination of a horizontal turn and during a vertical maneuver. The HCT model has low process noise and should accurately estimate the target state during a horizontal turn. The HCT model assumes that coordinated turns are performed in the horizontal plane relative to the target. Therefore, the state extrapolation and update equations in (16) and (17) are performed in a local East-North-Up (ENU) frame relative to the previous track state.

The state equations for the HCT model are nonlinear (see Section 5.2.1.2) because elements in the state transition matrix include $\Omega$. These nonlinearities are handled by approximating the state equations via a first-order Taylor expansion, as discussed in Section 2.2.1. The Jacobian of the state equation is given by

$$\tilde{\mathbf{F}} = \begin{bmatrix} 1 & \frac{\sin(\Omega(k)\Delta t(k))}{\Omega(k)} & 0 & -\frac{1-\cos(\Omega(k)\Delta t(k))}{\Omega(k)} & 0 & 0 & f_{\Omega,1}(k) \\ 0 & \cos(\Omega(k)\Delta t(k)) & 0 & -\sin(\Omega(k)\Delta t(k)) & 0 & 0 & f_{\Omega,2}(k) \\ 0 & \frac{1-\cos(\Omega(k)\Delta t(k))}{\Omega(k)} & 1 & \frac{\sin(\Omega(k)\Delta t(k))}{\Omega(k)} & 0 & 0 & f_{\Omega,3}(k) \\ 0 & \sin(\Omega(k)\Delta t(k)) & 0 & \cos(\Omega(k)\Delta t(k)) & 0 & 0 & f_{\Omega,4}(k) \\ 0 & 0 & 0 & 0 & 1 & \Delta t(k) & 0 \\ 0 & 0 & 0 & 0 & 0 & 1 & 0 \\ 0 & 0 & 0 & 0 & 0 & 0 & 1 \end{bmatrix}, \tag{116}$$

with

$$\begin{aligned} f_{\Omega,1}(k) = {} & \frac{\cos(\Omega(k)\Delta t(k))\Delta t(k)\dot{x}(k)}{\Omega(k)} - \frac{\sin(\Omega(k)\Delta t(k))\dot{x}(k)}{\Omega(k)^2} \\ & - \frac{\sin(\Omega(k)\Delta t(k))\Delta t(k)\dot{y}(k)}{\Omega(k)} - \frac{\left(-1+\cos(\Omega(k)\Delta t(k))\right)\dot{y}(k)}{\Omega(k)^2}, \end{aligned} \tag{117}$$

$$f_{\Omega,2}(k) = -\sin(\Omega(k)\Delta t(k))\Delta t(k)\dot{x}(k) - \cos(\Omega(k)\Delta t(k))\Delta t(k)\dot{y}(k), \tag{118}$$

$$\begin{aligned} f_{\Omega,3}(k) = {} & \frac{\sin(\Omega(k)\Delta t(k))\Delta t(k)\dot{x}(k)}{\Omega(k)} - \frac{\left(1-\cos(\Omega(k)\Delta t(k))\right)\dot{x}(k)}{\Omega(k)^2} \\ & + \frac{\cos(\Omega(k)\Delta t(k))\Delta t(k)\dot{y}(k)}{\Omega(k)} - \frac{\sin(\Omega(k)\Delta t(k))\dot{y}(k)}{\Omega(k)^2}, \end{aligned} \tag{119}$$

$$f_{\Omega,4}(k) = \cos(\Omega(k)\Delta t(k))\Delta t(k)\dot{x}(k) - \sin(\Omega(k)\Delta t(k))\Delta t(k)\dot{y}(k). \tag{120}$$

Since the HCT model includes an extra dimension for $\Omega$, the unbiased mixing procedure described in Appendix C will be used during the mixing stage. Notice that when $\Omega$ is close

<table>
<tr><th colspan="3">IMM-CVCVHCT</th></tr>
<tr><td colspan="3">$\mathbf{\Pi} = \begin{bmatrix} 0.92 & 0.05 & 0.03 \\ 0.10 & 0.70 & 0.20 \\ 0.15 & 0.03 & 0.82 \end{bmatrix}$</td></tr>
<tr><td colspan="3">$\boldsymbol{\mu}_0 = \begin{bmatrix} 0.8 & 0.1 & 0.1 \end{bmatrix}^T$</td></tr>
<tr><td><b>CV1</b></td><td><b>CV2</b></td><td><b>HCT</b></td></tr>
<tr><td>$\sigma_{a_x} = 3$ m/s$^2$</td><td>$\sigma_{a_x} = 40$ m/s$^2$</td><td>$\sigma_{a_x} = 3$ m/s$^2$</td></tr>
<tr><td>$\sigma_{a_y} = 3$ m/s$^2$</td><td>$\sigma_{a_y} = 40$ m/s$^2$</td><td>$\sigma_{a_y} = 3$ m/s$^2$</td></tr>
<tr><td>$\sigma_{a_z} = 3$ m/s$^2$</td><td>$\sigma_{a_z} = 40$ m/s$^2$</td><td>$\sigma_{a_z} = 3$ m/s$^2$</td></tr>
<tr><td>.</td><td>.</td><td>$\sigma_\Omega = 0.016$ rads/s$^2$</td></tr>
</table>

Table 7: Design parameters for IMM-CVCVHCT.

to zero, the limiting form of the state equations is

$$\tilde{\mathbf{F}}|_{\Omega=0} = \begin{bmatrix} 1 & \Delta t(k) & 0 & 0 & 0 & 0 & -\frac{1}{2}\Delta t_k^2 \dot{y}_k \\ 0 & 1 & 0 & 0 & 0 & 0 & -\Delta t_k \dot{y}_k \\ 0 & 0 & 1 & \Delta t_k & 0 & 0 & \frac{1}{2}\Delta t_k^2 \dot{x}_k \\ 0 & 0 & 0 & 1 & 0 & 0 & \Delta t_k \dot{x}_k \\ 0 & 0 & 0 & 0 & 1 & \Delta t_k & 0 \\ 0 & 0 & 0 & 0 & 0 & 1 & 0 \\ 0 & 0 & 0 & 0 & 0 & 0 & 1 \end{bmatrix}, \tag{121}$$

which should be used to prevent numerical issues. This will be used when the estimate of $\Omega$ is less than $\Omega_{min} = 0.03$ rad/s. Design parameters for this estimator are given in Table 7.

#### *5.2.2.3 IMM-CVCV3DCT*

The third IMM is similar to the estimator used in [51]. The IMM estimator includes three models: two CV models and a 3DCT (the N is dropped for sake of shorter acronyms) model. The first CV model, CV1, has small process noise and should accurately estimate the target state when the target is not maneuvering. The second CV model, CV2, has high process noise and should accurately estimate the target state when the target is at the onset and termination of CT maneuvers. The 3DCT model is used to estimate the target state when the target is performing a coordinated turn in any 3D "turn plane."

The 3DCT model described in Section 5.2.1.3 assumes knowledge of the turn rate $\omega$.

| **IMM-CVCV3DCT** | | |
|---|---|---|
| $\mathbf{\Pi} = \begin{bmatrix} 0.92 & 0.05 & 0.03 \\ 0.10 & 0.70 & 0.20 \\ 0.15 & 0.03 & 0.82 \end{bmatrix}$ | | |
| $\boldsymbol{\mu}_0 \begin{bmatrix} 0.8 & 0.1 & 0.1 \end{bmatrix}$ | | |
| **CV1** | **CV2** | **3DCT** |
| $\sigma_{a_x} = 3$ m/s$^2$ | $\sigma_{a_x} = 30$ m/s$^2$ | $\sigma_{j_x} = 8$ m/s$^3$ |
| $\sigma_{a_y} = 3$ m/s$^2$ | $\sigma_{a_y} = 30$ m/s$^2$ | $\sigma_{j_y} = 8$ m/s$^3$ |
| $\sigma_{a_z} = 3$ m/s$^2$ | $\sigma_{a_z} = 30$ m/s$^2$ | $\sigma_{j_z} = 8$ m/s$^3$ |
| . | . | $r_0 = 500$ |
| . | . | $r_1 = \frac{100}{64\Delta t_k^2}$ |
| . | . | $\delta = 0.9$ |
| . | . | $\omega_{min} = 0.03$ rad/s |

Table 8: Design parameters for IMM-CVCV3DCT.

Since this parameter is not known, it is computed using the state estimate $\hat{\mathbf{x}}(k)$ [40, 51]

$$\hat{\omega}(k) = \frac{\sqrt{\hat{\ddot{x}}(k)^2 + \hat{\ddot{y}}(k)^2 + \hat{\ddot{z}}(k)^2}}{\sqrt{\hat{\dot{x}}(k)^2 + \hat{\dot{y}}(k)^2 + \hat{\dot{z}}(k)^2}} \tag{122}$$

which is the magnitude of the acceleration divided by the speed. Since the 3DCT model has extra states for accelerations, the unbiased mixing procedure described in Appendix C is used during the mixing stage of this IMM estimator. The application of the KC as described in Section 5.2.1.4 is applied after the mixing process and after the measurement update.

The acceleration elements of the 3DCT state estimate are modified before and after the mixing process to enforce a minimum turn rate, $\omega_{min}$, as in [11]. The acceleration estimates are constrained to be othogonal to the velocity estimates by removing the portion of the acceleration parallel to velocity. The remaining acceleration is scaled to yield the minimum turn rate. Design parameters for this estimator are given in Table 8.

### 5.2.3 Results

100 Monte Carlo trials the scenario were performed using the MIMO Radar Benchmark [18]. The nominal tracking SNR, which is investigated in depth below, was set to 25 dB. The metrics used in performance evaluation are Root Sum Square Mean (RSSM), Root

| | **CVCV** | **CVCVHCT** | **CVCV3DCT** |
|---|---|---|---|
| Pos. RSSM (m) | 10.64 | 9.79 | 9.24 |
| Pos. RSSV (m) | 51.72 | 51.07 | 53.87 |
| Vel. RSSM (m/s) | 4.48 | 3.66 | 3.78 |
| Vel. RSSV (m/s) | 8.27 | 8.64 | 10.96 |
| Pos. RMS (m) | 54.74 | 53.86 | 56.04 |
| Vel. RMS (m/s) | 10.66 | 10.38 | 12.45 |

Table 9: Tracking Metrics using 100 Monte Carlo Trials averaged over the scenario.

Sum Square Variance (RSSV), and Root Mean Square (RMS). These metrics are defined as

$$RSSM_k = \left[ \sum_i \left( \frac{1}{N} \sum_n (\mathbf{x}_{k,n}(i) - \mathbf{y}_k(i)) \right)^2 \right]^{\frac{1}{2}} . \tag{123}$$

$$\begin{aligned} RSSV_k = & \left[ \sum_i \left( \frac{1}{N} \sum_n (\mathbf{x}_{k,n}(i) - \mathbf{y}_k(i))^2 \right. \right. \\ & \left. \left. - \left( \frac{1}{N} \sum_n (\mathbf{x}_{k,n}(i) - \mathbf{y}_k(i)) \right)^2 \right)^2 \right]^{\frac{1}{2}} . \end{aligned} \tag{124}$$

$$RMS_k = \left[ \sum_i \left( \frac{1}{N} \sum_n (\mathbf{x}_{k,n}(i) - \mathbf{y}_k(i))^2 \right) \right]^{\frac{1}{2}} . \tag{125}$$

where $N$ is the number of Monte Carlo trials, $k$ is a time index, $n$ is a Monte Carlo trial index, $i$ is an index to a state vector dimension, $\mathbf{x}$ is the state estimate, and $\mathbf{y}$ is the truth state.

To analyze the tracking algorithms, these metrics are averaged over certain time frames. Position and velocity are scored separately using the metrics defined above. Table 9 shows these metrics averaged over all time for all scenarios. This table displays mixed results, without any tracking algorithm showing noticeable benefits. Table 10 shows the metrics averaged over the times of horizontal maneuvers. For the case of horizontal turns, the IMM-CVCVHCT appears to be the superior tracking algorithm, with the IMM-CVCV3DCT performing better than the IMM-CVCV. Table 11 shows the metrics averaged over the times of vertical maneuvers. For this case, the IMM-CVCV3DCT appears to be the superior tracking algorithm, with the IMM-CVCVHCT providing the worst performance.

The results depicted in Tables 9 through 11 suggest that for highly maneuverable targets

| | **CVCV** | **CVCVHCT** | **CVCV3DCT** |
|---|---|---|---|
| Pos. RSSM (m) | 42.71 | 12.90 | 18.18 |
| Pos. RSSV (m) | 67.38 | 53.42 | 61.22 |
| Vel. RSSM (m/s) | 38.16 | 13.12 | 14.43 |
| Vel. RSSV (m/s) | 24.18 | 16.19 | 22.57 |
| Pos. RMS (m) | 83.86 | 55.52 | 65.84 |
| Vel. RMS (m/s) | 46.94 | 21.53 | 29.01 |

Table 10: Tracking Metrics during horizontal turns.

| | **CVCV** | **CVCVHCT** | **CVCV3DCT** |
|---|---|---|---|
| Pos. RSSM (m) | 66.93 | 70.70 | 57.07 |
| Pos. RSSV (m) | 69.81 | 75.15 | 72.55 |
| Vel. RSSM (m/s) | 36.50 | 36.65 | 29.16 |
| Vel. RSSV (m/s) | 19.94 | 24.81 | 23.98 |
| Pos. RMS (m) | 100.46 | 106.18 | 96.54 |
| Vel. RMS (m/s) | 42.51 | 45.39 | 40.01 |

Table 11: Tracking Metrics during vertical maneuvers.

peforming a mixture of horizontal and vertical maneuvers, the IMM-CVCV3DCT estimator may be the estimator of choice. However, for targets that only perform maneuvers in the horizontal plane, the IMM-CVCVHCT is the superior estimator. This is not entirely surprising, since the HCT model assumes that targets perform coordinated turns in the horizontal plane. To examine the behavior of the estimators more closely, Figure 38 shows the mode probabilities and turn rate estimates for the IMM-CVCVHCT and IMM-CVCV3DCT during the vertical maneuver. As shown, the IMM-CVCVHCT has mode probability spread somewhat evenly throughout the vertical maneuver. The models have excessive "comptetition" since none of the models can accurately predict the target motion. In general, this is considered undesirable behavior, as discussed in [31], since no kinematic model can appropriately "explain" the kinematics for an exended period of time. However, since the IMM-CVCV3DCT is not constrained to turns in the horizontal plane, the IMM-CVCV3DCT reports a coordinated turn for a portion of the vertical maneuver, which may explain the performance enhancement during vertical maneuvers. Since the IMM-CVCV3DCT has the ability to distinguish vertical maneuvers effectively, it is considered the superior estimator for the following work in this chapter.

In the following sections, the assumed constant revisit rate is relaxed to an adaptive

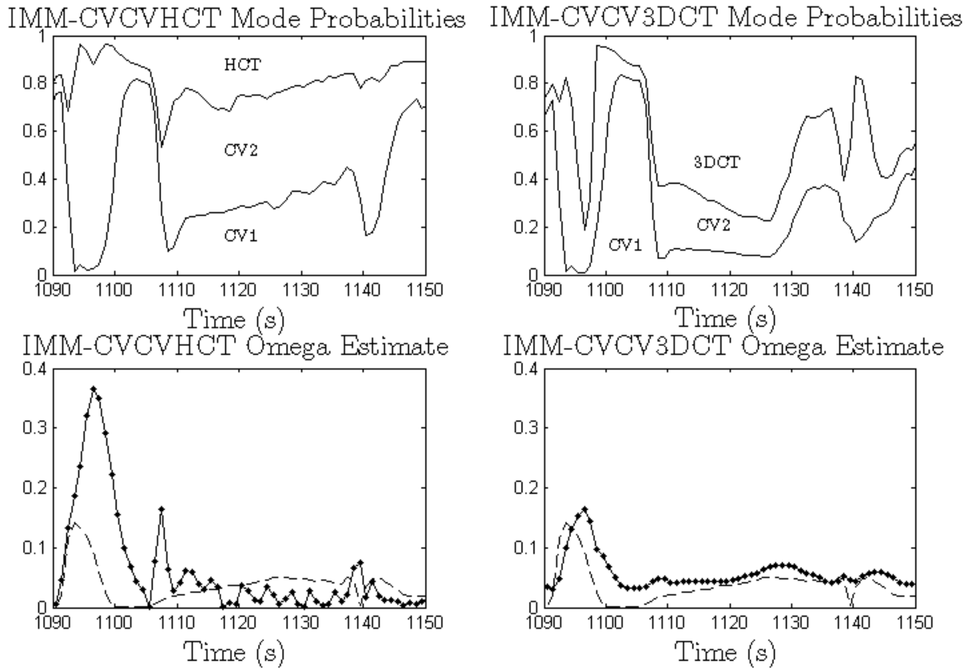

Figure 38: Estimator results during vertical maneuver.

revisit rate. Thus, as discussed in Section 2.2.1, a CWN process noise model should be used. For the NCV kinematic model, the process noise given by (94) is replaced by

$$\mathbf{w}(k) \sim \mathscr{N}\left(\mathbf{0}, \begin{bmatrix} q_{a_x}\mathbf{G}(k) & 0 & 0 \\ 0 & q_{a_y}\mathbf{G}(k) & 0 \\ 0 & 0 & q_{a_z}\mathbf{G}(k) \end{bmatrix}\right), \tag{126}$$

where

$$\mathbf{G}(k) = \begin{bmatrix} \frac{\Delta t(k)^3}{3} & \frac{\Delta t(k)^2}{2} \\ \frac{\Delta t(k)^2}{2} & \Delta t(k) \end{bmatrix}, \tag{127}$$

where $q_{a_x}$, $q_{a_y}$, and $q_{a_z}$ are design parameters. For the 3DCT kinematic model, the process noise given by (107) is replaced by

$$\mathbf{w}(k) \sim \mathscr{N}\left(\mathbf{0}, \begin{bmatrix} q_{j_x}\mathbf{G}(k) & 0 & 0 \\ 0 & q_{j_y}\mathbf{G}(k) & 0 \\ 0 & 0 & q_{j_z}\mathbf{G}(k) \end{bmatrix}\right) \tag{128}$$

where $\mathbf{G}(k)$ is a 3x3 matrix whose individual elements are given by,

$$\begin{aligned}
\mathbf{G}(k)_{1,1} &= \frac{6\omega(k)\Delta t(k) - 8\sin\omega(k)\Delta t(k) + \sin 2\omega(k)\Delta t}{4\omega(k)^5} \\
\mathbf{G}(k)_{1,2} &= \frac{2\sin^4(\omega(k)\Delta t(k)/2)}{\omega(k)^4} \\
\mathbf{G}(k)_{1,3} &= \frac{-2\omega(k)\Delta t(k) + 4\sin\omega(k)\Delta t(k) - \sin 2\omega(k)\Delta t(k)}{4\omega(k)^3} \\
\mathbf{G}(k)_{2,1} &= \frac{2\sin^4(\omega(k)\Delta t(k)/2)}{\omega(k)^4} \\
\mathbf{G}(k)_{2,2} &= \frac{w\omega(k)\Delta t(k) - \sin 2\omega(k)\Delta t(k)}{4\omega(k)^3} \\
\mathbf{G}(k)_{2,3} &= \frac{\sin^2\omega(k)\Delta t(k)}{2\omega(k)^2} \\
\mathbf{G}(k)_{3,1} &= \frac{-2\omega(k)\Delta t(k) + 4\sin\omega(k)\Delta t(k) - \sin 2\omega(k)\Delta t(k)}{4\omega(k)^3} \\
\mathbf{G}(k)_{3,2} &= \frac{\sin^2\omega(k)\Delta t(k)}{2\omega(k)^2} \\
\mathbf{G}(k)_{3,3} &= \frac{2\omega(k)\Delta t(k) + \sin 2\omega(k)\Delta t(k)}{4\omega(k)}.
\end{aligned} \tag{129}$$

The $q_{j_x}$, $q_{j_y}$, and $q_{j_z}$ are design parameters. To our knowledge, this is the first appearance of a CWN process noise model for the 3DCT kinematic model being used in a tracking algorithm.

To account for an adaptive revisit rate, Markov transition probabilities used in the mixing and mode probability update equations of the IMM estimator are based on two nominal sets of Markov transition probabilties. One set is designed for a revisit period of 0 seconds, which is simply the identity matrix, and the second set is designed for a revisit period of 5 seconds. For a specified revisit time, the Markov transition probabilities are an elementwise linear interpolation of the two matrices based on the revisit time. If a revisit period is greater than 5 seconds, then the Markov transition probabilities for a 5 second period is used. New design parameters for the IMM-CVCV3DCT are provided in Table 12.

## *5.3 Selection of Nominal Tracking SNR*

In the previous section, the IMM-CVCV3DCT was shown to be the superior estimator for tracking a highly maneuvering target, using a nominal tracking SNR level of 25 dB. In

Table 12: Design parameters for IMM-CVCV3DCT using CWN.

| **IMM-CVCV3DCT** | | |
|---|---|---|
| $p_{ij,0} = \begin{bmatrix} 1 & 0 & 0 \\ 0 & 1 & 0 \\ 0 & 0 & 1 \end{bmatrix}$ $p_{ij,5} = \begin{bmatrix} 0.92 & 0.05 & 0.03 \\ 0.10 & 0.70 & 0.20 \\ 0.15 & 0.03 & 0.82 \end{bmatrix}$ | | |
| $\mu_j(0) = \begin{bmatrix} 0.1 & 0.8 & 0.1 \end{bmatrix}$ | | |
| **CV1** | **CV2** | **3DCT** |
| $q_{a_x} = 9 \text{ m}^2/\text{s}^3$ | $q_{a_x} = 2500 \text{ m}^2/\text{s}^3$ | $q_{j_x} = 64 \text{ m}^2/\text{s}^3$ |
| $q_{a_y} = 9 \text{ m}^2/\text{s}^3$ | $q_{a_y} = 2500 \text{ m}^2/\text{s}^3$ | $q_{j_y} = 64 \text{ m}^2/\text{s}^3$ |
| $q_{a_z} = 9 \text{ m}^2/\text{s}^3$ | $q_{a_z} = 2500 \text{ m}^2/\text{s}^3$ | $q_{j_z} = 64 \text{ m}^2/\text{s}^3$ |
| . | . | $\rho_0 = 500$ |
| . | . | $\rho_1 = \frac{100}{64\Delta t_k^2}$ |
| . | . | $\delta = 0.9$ |
| . | . | $\omega_{min} = 0.03 \text{ rad/s}$ |

this section, impacts of the nominal tracking SNR on expended radar time and energy is further studied. To illustrate how accurate track predictions positively impact radar energy management, radar time and energy expended using a simple Kalman estimator equivalent to CV2 in the IMM-CVCV3DCT is compared with the IMM-CVCV3DCT.

### 5.3.1 Revisit Time Calculations

Upon the selection of the IMM-CVCV3DCT as the superior estimator for tracking maneuvering air targets, investigation into radar energy management can proceed, beginning with a proposed methodology for computing track revisit rates. Revisit time calculations are based on the extrapolated covariance of the track state and a specified fraction, $f$, of the main beam size. Let $C(t_i)$ be the major axis of an extrapolated positional covariance projected to the 2D plane parallel to the array face at time $t_i$, and let $V$ represent the 3 dB beamwidth of the main beam in Cartesian coordinates at the extrapolated track state. The size of $V$ depends only upon the range of the extrapolated track state. In Cartesian coordinates, a longer range corresponds to a larger cross-range size of the main beam. Since $C(t_i)$ increases with time, a revisit is scheduled when

$$C(t_r) = fV, \tag{130}$$

where $t_r$ is the scheduled revisit time. Extrapolation of the IMM track state, $\hat{\mathbf{x}}_{t_i}$, and covariance, $\mathbf{P}_{t_i}$, consists of standard state extrapolation of each individual mode, followed by a linear combination of the positional elements of each mode based on extrapolated mode probabilities from the last revisit time, denoted as $t_0$:

$$\begin{aligned}
\mu_{t_i|t_0} &= \mathbf{\Pi}_{\mathbf{t_i-t_0}}\mu_{\mathbf{t_0}}, && (131)\\
\hat{\mathbf{x}}_{t_i} &= \hat{\mathbf{x}}^1_{t_i}\mu_{\mathbf{t_i|t_0}}(1) + \hat{\mathbf{x}}^2_{t_i}\mu_{\mathbf{t_i|t_0}}(2) + \hat{\mathbf{x}}^2_{t_i}\mu_{\mathbf{t_i|t_0}}(3), && (132)\\
\mathbf{P}_{t_i} &= \left(\mathbf{P}^1_{t_i} + \tilde{\mathbf{P}}^1\right)\mu_{t_i|t_0}(1) \\
&\quad + \left(\mathbf{P}^2_{t_i} + \tilde{\mathbf{P}}^2\right)\mu_{t_i|t_0}(2) \\
&\quad + \left(\mathbf{P}^3_{t_i} + \tilde{\mathbf{P}}^3\right)\mu_{t_i|t_0}(3), && (133)
\end{aligned}$$

where

$$\begin{aligned}
\tilde{\mathbf{P}}^1 &= (\hat{\mathbf{x}}_{t_i} - \hat{\mathbf{x}}^1_{t_i})(\hat{\mathbf{x}}_{t_i} - \hat{\mathbf{x}}^1_{t_i})^T, && (134)\\
\tilde{\mathbf{P}}^2 &= (\hat{\mathbf{x}}_{t_i} - \hat{\mathbf{x}}^2_{t_i})(\hat{\mathbf{x}}_{t_i} - \hat{\mathbf{x}}^2_{t_i})^T, && (135)\\
\tilde{\mathbf{P}}^3 &= (\hat{\mathbf{x}}_{t_i} - \hat{\mathbf{x}}^3_{t_i})(\hat{\mathbf{x}}_{t_i} - \hat{\mathbf{x}}^3_{t_i})^T, && (136)
\end{aligned}$$

and superscripts indicate mode. The use of extrapolated mode probabilities is not described in the literature, but they should be used if variable Markov transition probabilities are used. Since $C(t_r)$ is very difficult to express in closed form for the IMM estimator, an array of candidate times are evaluated and the longest revisit period satisfying $C(t_r) \leq fV$ is chosen. In the proposed scheduler, candidate times range from 0.1 to 10 seconds in increments of 0.1 seconds. The location of the scheduled beam is at the extrapolated target state estimate $\hat{\mathbf{x}}_{t_r}$. For a simple Kalman CV estimator, extrapolated track states and covariances are straightforwardly given by (16) and (17).

Since highly agile targets can maneuver at any moment, a maximum allowed revisit time is needed to prevent a maneuver that is outside of the predicted beam point. Recalling that $V$ represents the size of the main beam in Cartesian coordinates, and assuming a target can accelerate with $a_m$ in any given direction, the maximum allowed revisit calculation is given by

$$t_m = \sqrt{\frac{V}{a_m}}, \tag{137}$$

Since $V$ increases with increasing range, $t_m$ also increases with range.

### 5.3.2 Pulsewidth Scheduling

Once a track revisit time calculation is complete, a waveform pulsewidth must be selected. For each track, a history of $N$ previous observed SNR levels with corresponding pulsewidth lengths are stored in memory. Then, the median of these SNR levels is found with its corresponding pulsewidth size. By calculating the number of 3 dB steps needed in order to achieve the nominal tracking SNR from the median observed SNR, and recalling from Section 5.1 that pulsewidths are arranged in 3 dB steps, the next pulsewidth can be easily found. Note that the nominal tracking SNR is the key parameter we wish to optimize, as it directly effects the total radar time and energy expended for sufficient tracking. Since practical targets fluctuate in RCS, the median filter provides robustness against outliers. For the tracker, the history window is chosen to be $N = 5$.

### 5.3.3 Missed Detections and Track Loss

Since practical target RCS values can fluctuate drastically with aspect angle and transmitted frequency, missed detections are almost certain to occur and must be handled. For each track in memory, the tracker stores a history of consecutive missed detections. Upon a missed detection, the revisit time calculations from Section 5.3.1 are overwritten by a predefined set of possible revisit times, given by

$$\Delta t_{rm} = [0.1 \;\; 0.1 \;\; 0.2 \;\; 0.2 \;\; 0.5 \;\; 1 \;\; 1 \;\; 1 \;\; 1], \tag{138}$$

where the $i$th element corresponds to an $i$th consecutive missed detection. For each missed detection, an observed SNR of 3 dB below the detection threshold is inserted into the observed SNR window described in the previous section. Therefore, with a window size of $N = 5$, an increase in waveform strength is certain upon 3 consecutive missed detections. If a detection is received on a track dwell, the missed detection counter will be reset and standard revisit calculations from Section 5.3.1 will proceed. However, if the number of consecutive missed detections reaches 10, the track is removed from memory. If a track is dropped, the target may be re-acquired during the search fence that is scheduled to occur every 10 seconds in the MIMO Benchmark.

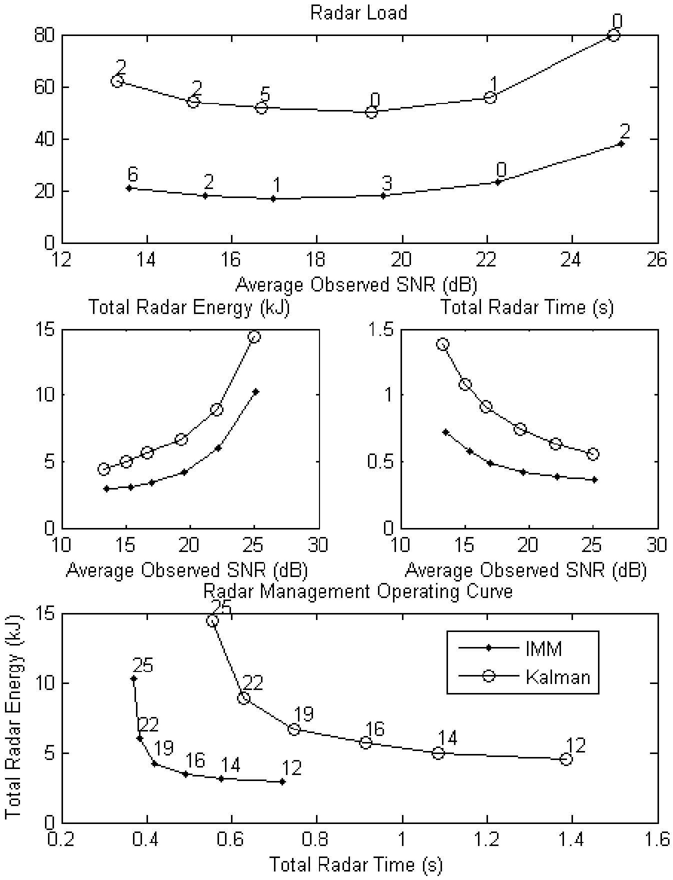

Figure 39: Results from 100 Monte Carlo Trials for each nominal tracking SNR with an IMM estimator and Kalman filter. Circles indicate Kalman filter results, while solid dots denote results for IMM Estimator. Numbers on the symbols of the top chart indicate total number of tracks lost at each SNR level. Numbers on symbols of the bottom chart indicate the nominal SNR level set for tracking.

---

## *5.4 Results*

Several nominal tracking SNR levels were evaluated using Monte Carlo simulations in the MIMO Benchmark with four metrics: total energy, total radar time, radar load, and track loss. Total radar energy is the total energy of all scheduled track waveforms (*i.e.*, transmit power times pulsewidth) divided by the number of Monte Carlo trials. Radar time for a single radar dwell is the round-trip travel time to the maximum range of the range window plus a nominal signal processing time of 1 ms. Total radar time is the total time of all scheduled track dwells divided by the number of Monte Carlo trials. Track loss corresponds to the number of dropped tracks, as described in Section 5.3.3, divided by the total number of tracks initiated during a Monte Carlo simulation. The radar load metric from [48] is calculated as total radar energy times total radar time.

Results are shown in Figure 39. From the radar load metric, the Kalman filter is optimized when the observed SNR is in the range of 16 db to 20 dB, which somewhat agrees with the optimal result of 16 dB reported in [48]. The results appear to suggest an optimal level of 18 dB for the Kalman estimator. Furthermore, an optimal nominal tracking SNR for an IMM estimator is quite close to the optimal level for a Kalman estimator. The radar load metric appears to suggest an optimal tracking SNR level of 17 dB for the IMM estimator, just a single decibel lower than the Kalman estimator. Also, track loss does not appear to be a concern for most of the tracking SNR levels. The IMM estimator operating at 13 dB tends to have issues with missed detections, which increased the number of lost tracks. The track loss of 5 for the Kalman estimator at 17 dB appears to be a statistical outlier. Finally, using the radar load metric, the IMM estimator more than doubles the efficiency of a radar for tracking maneuvering targets regardless of the choice of tracking SNR, verifying the results of the first and second Benchmark problems.

The bottom chart of Figure 39 includes a graph of radar time versus radar energy for all tracking SNR levels. This graph is referred to as the radar management operating curve (RMOC); it portrays the fundamental tradeoff between radar time and energy for the radar tracking system. In general, a desirable RMOC will be “pushed” as far down and to the left as possible, which for a given radar system can be achieved with better tracking and scheduling. Recall that the authors in [48] claim that the radar load metric maximizes the total number of maintainable tracks. However, this is not necessarily true. In practice, radars are generally limited by duty (transmitted energy per second) or occupancy (radar time), which are sensor and situation specific. The y-axis of the RMOC can be scaled to a percent duty per target and the x-axis to a percent occupancy per target, from which a maximum number of maintained tracks can be established for a given radar.

As shown in the RMOC, tracking SNR levels below 16 dB for the IMM estimator tend to waste total radar time while receiving little reduction in radar energy, and a tracking

SNR level above 22 dB tends to waste radar energy with little reduction in radar time. Using this chart, "valid" nominal tracking SNR levels in practice should be around 16-22 dB. Tracking SNR levels above 22 dB with an IMM estimator tend to be limited by the maximum maneuver of the target, thus limiting the possible reduction in total radar time. To illustrate this concept, average revisit periods for several tracking SNR levels during the second maneuver are provided in Figure 40. For tracking SNRs of 12 and 19 dB, the revisit periods decrease during the second coordinated turn and increase after the termination of the maneuver. However, revisit periods with a nominal tracking SNR level of 25 dB appears flat after the maneuver, since the CV1 mode dominates and the revisit calculations are limited on nearly all Monte Carlo trials by the assumed maximum maneuver of the target.[2] Thus, from an energy management perspective, a maximum assumed maneuver sets an upper limit on the desirable tracking SNR level.

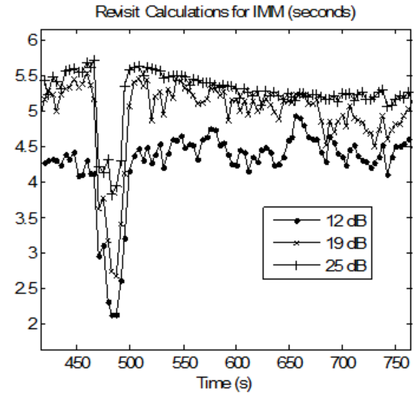

Figure 40: Revisit calculations for the IMM estimator.

Thus far, a $P_{fa}$ of $10^{-5}$ has been used for all of the results. This is a critical design parameter in a radar tracking system; it can impact the RMOC with higher detection probabilities at lower SNR levels through a lower detection threshold. However, a lower detection threshold induces the cost of more false alarms, which consume resources in and of themselves. If not associated to an existing track, false alarms receive confirmation dwells (or deconfirmation, depending upon perspective), further providing a tradeoff in energy management. Monte Carlo simulations were conducted for the IMM tracker at all the SNR

---

[2] Without the maximum maneuver criterion, track loss occurred regularly during the $6g$ vertical maneuver.

levels in Figure 39 with $P_{fa} = 10^{-4}$. The results for track loss as a function of tracking SNR and $P_{fa}$ are provided in Table 13. The misassociation of false alarms to the track state result in the higher rates of track loss, especially at lower tracking SNR levels. For revisit periods in the range of 5 seconds, the IMM estimator sees false alarms as "maneuvers" when the true target is not detected. These tracks diverge from the truth and are eventually lost. Therefore, to facilitate the use of lower detection thresholds for the tracking of maneuvering targets, more sophisticated data association or scheduling algorithms must be used.

Table 13: Lost tracks versus nominal tracking SNR and $P_{fa}$

| | SNR (dB) | | | | | |
|---|---|---|---|---|---|---|
| $P_{fa}$ | 12 | 14 | 16 | 19 | 22 | 25 |
| $10^{-5}$ | 6 | 2 | 1 | 3 | 0 | 2 |
| $10^{-4}$ | 23 | 14 | 11 | 3 | 6 | 4 |

## *5.5 Concluding Remarks*

Using the GTRI/ONR MIMO Benchmark, the problem of tracking maneuvering targets with an agile beam radar was revisited. Using implementations of reasonable tracking and scheduling algorithms, some portions of previous literature were verified, in that the IMM doubles the efficiency of an agile beam radar for tracking maneuverable targets as compared to simple Kalman estimators. The IMM estimator can double the efficiency of an agile beam radar for the tracking of maneuvering targets, and desirable levels for nominal tracking SNR are in the range of 15 - 22 dB. We showed that desirable tracking SNR levels for a Kalman estimator and an IMM estimator are nearly the same. Finally, we introduced the radar management operating curve (RMOC) and its relevance to the design of radar tracking algorithms was justified by illustrating the fundamental tradeoff between radar time and energy in the selection of a radar waveform and overall nominal tracking SNR levels. Future research will include more sophisticated data association algorithms so that the effects of a lower detection threshold on the RMOC can be characterized. Also, further investigation into the RMOC for other radar systems and target types is needed.

# CHAPTER VI

# CONCLUSIONS AND FUTURE RESEARCH

This dissertation advanced several aspects of radar detection, monopulse processing, and radar target tracking. Here, an overview of the contributions and interesting observations contained in this dissertation is provided, along with suggestions for future avenues of research. Detailed descriptions of the contributions can be found at the end of Chapters 3, 4, and 5.

Conventional monopulse processing treats radar signal samples individually. However, in practice, typical sampling rates result in multiple adjacent radar signal samples containing target energy, resulting in correlated samples. Since conventional monopulse processing ignores this correlation it is suboptimal. In this disseration, the radar sampling process was treated in a systematic way, resulting in a joint-bin approach to radar signal processing.

The ALLRT detector was derived in Appendix A and shown to be a weighted sum of observed SNRs and observed correlation between radar signal samples. The ALLRT coefficients depend upon the functional form of the transmitted waveform, and are straightforward to compute. For the triangle matched filter response, the coefficients are equal (i.e., SNR and correlation weighted equally), whereas for a sinc matched filter response, the correlation is weighted slightly more than observed SNR. This dissertation represents the first appearance of the ALLRT formalism in detection theory; an in depth study from a theoretical perspective is needed. In Chapter 3, flaws in traditional radar detectors were illustrated in terms of detection performance losses, particularly for a high number of pulses, and ALLRT was shown to overcome these shortcomings. Furthermore, the proposed ALLRT detector was shown to be a viable alternative to using traditional radar detectors with oversampled matched filter outputs, while adding little computational complexity. While oversampling of radar signals is a reasonable approach to overcome these losses, oversampling may not be cost effective or even possible with the advent of high-bandwidth radar signals.

A new joint-bin approach to monopulse parameter estimation was derived in Appendix B. Using an ML approach, estimators for target range, target strength, and target DOA were provided. A simple expression for target range estimation was given, and shown to depend upon the matched filter response of the transmitted waveform. Assuming a triangular matched filter reponse results in a closed-form expression for target range, as provided in Appendix B. Finding closed-form expressions for target range using more complicated waveforms is left for future work. Given a target range estimate, the target strength estimate is a closed-form expression. Given estimates for target range and target strength, DOA estimation is equivalent to solving a third-order polynomial. Derivations of closed-form CRLBs were also provided in Appendix B.

In Chapter 4, bin straddling was shown to result in a direct loss of target SNR in terms of DOA estimation, and the loss depends upon the transmitted waveform. Also, in Chapter 4, the joint-bin approaches were shown to outperform existing techniques that ignore the correlation between radar signal samples, particularly for the case of low SNR, off-boresight targets. In practical surveillance radar systems, the use of target localization estimates in the tracking requires corresponding error variance reports. In Chapter 4, the GCRLB, which is the CRLB evaluated at parameter estimates, is proposed as an error variance report. This dissertation represents the first appearance of the GCRLB formalism in estimation theory; an in-depth study from a theoretical perspective may provide valuable insights in terms of error variance reporting. Using the ANEES metric, the statistical efficiency and variance consistency of the parameter estimates and associated error variance estimates were analyzed. For off-boresight targets with worst case bin straddling, around 20 dB of total target SNR was shown as a requirement for variance consistency. This total SNR requirement decreases as targets move closer to boresight or if target energy is contained in a single sample.

A second portion of this dissertation re-examined the radar tracking of highly maneuvering targets, with a focus on radar resource management. In Chapter 5, an IMM filter that incorporates a 3D turn model was shown to outperform an IMM filter that incorporates a horizontal turn model. As part of this study, the unbiased mixing procedure seen in recent literature was extended from two modes to three as outlined in Appendix C. Using the IMM filter that incorporates a 3D turn model, an optimal tracking SNR level of 17 dB was found. Also in Chapter 5, we proposed the radar management operating curve (RMOC), which illustrates the fundamental tradeoff between radar time and energy. For a specific radar in a specific operational scenario, the radar management operating curve can be used to select an operating SNR level that will maximize the total number of targets tracked.

Several avenues of research are left for future work:

- Implementation of the proposed detection and estimation techniques of Chapters 3 and 4 into high fidelity radar simulation software is left for future work. A practical issue that needs treatment is the adjacent detection issue, outlined as follows. Although the ALLRT detector described in Chapter 3 alleviates detection losses that result from bin straddling, a high SNR target may result in adjacent ALLRT detections. Thus, a decision must be made as to whether single or multple objects exist in those detections. Furthermore, the impacts of the processing in Chapters 3 and 4 on the RMOC curve needs investigation. Given that observed monopulse ratios are very good for near-boresight targets, the proposed estimation techniques described in Chapter 4 are most useful for tracking groups of resolvable objects separated in a DOA magnitude of $\eta \geq 1$.

- The detection and estimation techniques described herein rely on knowledge of the matched filter response of the transmitted radar waveform. Future work includes investigating waveform design considerations using the joint-bin approaches proposed in this work.

- Although only briefly discussed in Section 2.1, radar tracking of unresolved objects is an important, and still open, research topic. Since our fundamental addition to conventional monopulse processing is the use of observed correlations between radar signal samples, perhaps the observed correlation could be useful in the detection of the presence of unresolved objects. Many authors that treat the monopulse detection of unresolved targets ignore the observed correlation between samples. Furthermore, the effects of unresolved objects on the range and DOA estimators provided in Chapter 4 need exploration. In particular, the signal levels at which unresolved objects corrupt the joint-bin DOA estimate need investigation.

- In Chapter 4, properties of the target amplitude estimator, $\hat{\beta}^2$, and its GCRLB variance report were not studied in depth. Future work includes a study of this estimator in terms of statistical efficiency and consistency. The statistical variance of target amplitudes is often used in target recognition algorithms. In particular, some types of targets may appear as pure Rayleigh targets and some as fixed amplitude targets. Using the signal models provided in this dissertation, studying the impacts of the bin straddling phenomenon on target recognition algorithms may be a promising avenue of research.
- The effects of other relevant radar tracking parameters should be studied in terms of their effect on the RMOC. One example is the probability of a false alarm. By lowering the detection threshold, a higher probability of detection comes at the cost of more false alarms. With the use of sophisticated data association track filters and candidate false alarm probabilities, perhaps the radar time and energy required for tracking can be minimized. Furthermore, the impacts of false alarm probability should be studied in terms of an optimal operating SNR.

# APPENDIX A

# ALLRT DETECTOR

In this section, we derive the average loglikelihood ratio test (ALLRT). Assuming a sample rate equivalent to the Rayleigh resolution of the transmitted waveform, the $l$th i.i.d. observation vector includes two adjacent matched filter samples in the region under test

$$\mathbf{s}_l = \begin{bmatrix} s_l(0) \\ s_l(1) \end{bmatrix}. \tag{139}$$

Probability density functions for the hypothesis of a target present, denoted as $H_1$, and a target not present, denoted as $H_0$, can be expressed as

$$H_1 : \mathbf{s}_l \sim \mathcal{N}\left(\mathbf{0}, \mathbf{K}_1\right), \tag{140}$$

$$H_0 : \mathbf{s}_l \sim \mathcal{N}\left(\mathbf{0}, \mathbf{K}_0\right), \tag{141}$$

where $\mathcal{N}\left(\mathbf{a}, \mathbf{C}\right)$ denotes the multivariate normal distribution with mean $\mathbf{a}$ and covariance $\mathbf{C}$, and

$$\mathbf{K}_1 = \begin{bmatrix} \beta^2 q(c)^2 + \sigma^2 & \beta^2 q(c) q(c-1) \\ \beta^2 q(c) q(c-1) & \beta^2 q(c-1)^2 + \sigma^2 \end{bmatrix}, \tag{142}$$

$$\mathbf{K}_0 = \begin{bmatrix} \sigma^2 & 0 \\ 0 & \sigma^2 \end{bmatrix}. \tag{143}$$

The $q(c)$ is the time-normalized matched filter response from (43), and $c \in [0, 1]$ is related to the location of the target in the region under test from (44). Denoting $2N$ as the total number of i.i.d. observations, the loglikelihood ratio test (LLRT) can be expressed as

$$\frac{1}{2N} \sum_{l=1}^{2N} \mathbf{s}_l^T \left(\mathbf{K}_0^{-1} - \mathbf{K}_1^{-1}\right) \mathbf{s}_l \quad \underset{H_0}{\overset{H_1}{\gtrless}} 2 \ln \left( \frac{|2\pi \mathbf{K}_1|}{|2\pi \mathbf{K}_0|} \right). \tag{144}$$

Analytic evaluation of the matrix inverse and algebraic simplifications give

$$\mathbf{K}_0^{-1} - \mathbf{K}_1^{-1} = \frac{\beta^2}{\sigma^2(\beta^2 q(c)^2 - \beta^2 q(1-c)^2 + \sigma^2)} \begin{bmatrix} q(c)^2 & q(c) q(1-c) \\ q(c) q(1-c) & q(1-c)^2 \end{bmatrix}. \tag{145}$$

The LLRT can now be expressed as

$$\frac{1}{2M\sigma^2}\sum_{l=1}^{2N}\mathbf{s}_l^T\begin{bmatrix} q(c)^2 & q(c)q(1-c) \\ q(c)q(1-c) & q(1-c)^2 \end{bmatrix}\mathbf{s}_l \underset{H_0}{\overset{H_1}{\gtrless}}$$
$$\frac{2\sigma^2(\beta^2 q(c)^2 - \beta^2 q(1-c)^2 + \sigma^2)}{\beta^2}\ln\left(\frac{|2\pi\mathbf{K}_1|}{|2\pi\mathbf{K}_0|}\right). \qquad (146)$$

For simplicity, denoting the right side of (146) as $\gamma\left(q(c), \sigma^2, \beta^2\right)$ gives

$$\frac{1}{2N\sigma^2}\sum_{l=1}^{2N}\mathbf{s}_l^T\begin{bmatrix} q(c)^2 & q(c)q(1-c) \\ q(c)q(1-c) & q(1-c)^2 \end{bmatrix}\mathbf{s}_l \underset{H_0}{\overset{H_1}{\gtrless}} \gamma\left(q(c), \sigma^2, \beta^2\right). \qquad (147)$$

A few observations about the LLRT are worth discussion. First, the test statistic involves the functional form of the matched filter response at matched filter samples. This potentially opens a new avenue for radar waveform design from the perspective of detection performance. Second, rewriting the left side of (147) into an alternate form

$$\frac{1}{2N\sigma^2}\sum_{l=1}^{2N}\mathbf{s}_l^T\begin{bmatrix} q(c)^2 & q(c)q(1-c) \\ q(c)q(1-c) & q(1-c)^2 \end{bmatrix}\mathbf{s}_l = \frac{1}{2N\sigma^2}\sum_{l=1}^{2N}\left(q(c)s_l(0) + q(1-c)s_l(1)\right)^2, \qquad (148)$$

leads to an interesting observation: the LLRT can be seen as a *weighted coherent* sum across adjacent samples, and *noncoherent* sum across i.i.d. observations (i.e., pulses).

In this work, the parameters $c$ and $\beta^2$ are treated as unknowns. A reasonable approach for this issue is to assume a distribution over the unknown parameters and calculate the expected value of the LRT. This has been called the average likelihood ratio test (ALRT) in the literature [42]. Unfortunately, the ALRT for the detection situation described in this section results in an intractable integral involving $\beta^2$ and $c$. Since the test statistic for the LLRT does not involve $\beta^2$, the average loglikelihood ratio test (ALLRT) is proposed, resulting in a simple closed-form expression. To our knowledge, this is the first appearance of the ALLRT formalism in detection theory. Although the ALLRT does not have any specific optimality properties, it has been shown to perform reasonably well. A comparative study of the ALLRT and ALRT detectors is left for future study.

A uniform distribution on the interval of zero to one for the unknown parameter $c$ gives the ALLRT as

$$\int_0^1 \frac{1}{2N\sigma^2}\sum_{l=1}^{2N} \mathbf{s}_l^T \begin{bmatrix} q(c)^2 & q(c)q(1-c) \\ q(c)q(1-c) & q(1-c)^2 \end{bmatrix} \mathbf{s}_l dc \underset{H_0}{\overset{H_1}{\gtrless}} \int_0^1 \gamma\left(q(c),\sigma^2,\beta^2\right) dc = \gamma'\left(\sigma^2,\beta^2\right),$$

$$\frac{1}{2N\sigma^2}\sum_{l=1}^{2N} \mathbf{s}_l^T \left(\int_0^1 \begin{bmatrix} q(c)^2 & q(c)q(1-c) \\ q(c)q(1-c) & q(1-c)^2 \end{bmatrix} dc\right) \mathbf{s}_l \underset{H_0}{\overset{H_1}{\gtrless}} \gamma'\left(\sigma^2,\beta^2\right). \tag{149}$$

Under the Rayleigh sampling assumption, $\int_0^1 q(c)^2 dc = \int_0^1 q(1-c)^2 dc$. Defining ALLRT coefficients as

$$a_1 = \int_0^1 q(c)^2 dc, \tag{150}$$

$$a_2 = 2\int_0^1 q(c)q(1-c)dc, \tag{151}$$

the ALLRT can be expressed as

$$\frac{1}{2N\sigma^2}\sum_{l=1}^{2N} \mathbf{s}_l^T \begin{bmatrix} a_1 & a_2/2 \\ a_2/2 & a_1 \end{bmatrix} \mathbf{s}_l \underset{H_0}{\overset{H_1}{\gtrless}} \gamma',$$

$$\frac{1}{2N\sigma^2}\sum_{l=1}^{2N}(a_1 s_l(0)^2 + a_1 s_l(1)^2 + a_2 s_l(0)s_l(1)) \underset{H_0}{\overset{H_1}{\gtrless}} \gamma'. \tag{152}$$

Under the hypothesis of no target present, the pdf of the ALLRT test statistic is called a distribution of quadratic forms [27]. For a rectangular waveform, the matched filter response is a triangle function as defined in (47), resulting in easy computation of ALLRT coefficients: $a_1 = 1/3$ and $a_2 = 1/3$. Assuming a sinc function matched filter response, defined as

$$q_S(c) = \frac{\sin(\pi c)}{\pi c}, \tag{153}$$

results in $a_1 \approx .4514$ and $a_2 \approx 0.494$. Note that an ALLRT approach could be taken for sample rates above the Rayleigh resolution. However, correlated noise that arises due to oversampling will make such a derivation more challenging than assuming a sample rate equal to the Rayleigh resolution. Derivation of the ALLRT detector for oversampled matched filter outputs is left for future study.

# APPENDIX B

# DERIVATION OF $\beta^2$, $C$, AND $\eta$ ESTIMATORS

In this section, estimators for the unknown $\beta^2$, $c$, and $\eta$ are derived along with their corresponding CRLBs. These derivations focus on finding simple expressions for these estimators, even if approximations to a full ML solution must be made. In many steps of the derivation, symbolic mathematical software was used to simplify overly complex algebraic expressions. The solutions to certain algebraic equations, along with their underlying assumptions, are provided. First, a few relevant expressions from the structured covariance estimation litertature that are used in the derivation are reviewed. Then, ML estimates of $\beta^2$ and $c$ are derived using only samples of the sum channel. Those estimates are further used in a generalized maximum likelihood (GML) solution for estimation of $\eta$.

## *B.1 Basic Relationships of Structured Covariance Estimation*

Following the assumptions described in Section 3.1, the observation vector is distributed as the zero-mean multivariate Gaussian distribution

$$f\left(\mathbf{s}_1,...,\mathbf{s}_{2N}|\Theta\right) = \frac{1}{\left|2\pi\mathbf{K}\left(\mathbf{\Theta}\right)\right|^N}\exp\left(-\frac{\sum_{l=1}^{2N}\mathbf{s}_l^T\left(\mathbf{K}\left(\mathbf{\Theta}\right)\right)^{-1}\mathbf{s}_l}{2}\right), \tag{154}$$

where $N$ is the total number of pulses and $\Theta$ is the unknown parameter set that resides in the covariance matrix. Given a set of measured data, the likelihood function of an estimate $\hat{\Theta}$ is defined as

$$\mathfrak{L}\left(\hat{\Theta}|\mathbf{s}_1,...,\mathbf{s}_{2N}\right) = f\left(\mathbf{s}_1,...,\mathbf{s}_{2N}|\hat{\Theta}\right), \tag{155}$$

and the ML estimator maximizes this function. As shown in [16], finding the ML estimator for $\Theta$ is equivalent to jointly solving

$$\operatorname{tr}\left((\mathbf{K}^{-1}\bar{\mathbf{K}}\mathbf{K}^{-1} - \mathbf{K}^{-1})\frac{\partial\mathbf{K}}{\partial\Theta_i}\right) = 0, \tag{156}$$

for each of the unknown parameters in $\Theta$, denoted as $\Theta_i$, where $\bar{\mathbf{K}}$ is the sample covariance of the measured data, computed as

$$\begin{aligned}\bar{\mathbf{K}} &= \frac{1}{2N}\sum_{l=1}^{2N} \mathbf{s}_l \mathbf{s}_l^T \\ &= \begin{bmatrix} k_{11} & k_{12} & k_{13} & k_{14} \\ k_{12} & k_{22} & k_{23} & k_{24} \\ k_{13} & k_{23} & k_{33} & k_{34} \\ k_{14} & k_{24} & k_{34} & k_{44} \end{bmatrix}. \end{aligned} \tag{157}$$

Furthermore, from [38] the individual elements of the Fisher information matrix for the estimator $\hat{\Theta}$ can be expressed as

$$J_{m,n} = N\mathrm{tr}\left(\frac{\partial \mathbf{K}}{\partial \Theta_m}\mathbf{K}^{-1}\frac{\partial \mathbf{K}}{\partial \Theta_n}\mathbf{K}^{-1}\right), \tag{158}$$

and the CRLB matrix is defined as the inverse the the Fisher information matrix. Diagonal elements of the CRLB matrix correspond to the CRLB for each individual parameter.

### *B.2* $\beta^2$ *and* $c$ *Estimation*

Estimators for $\beta^2$ and $c$ are found using samples of the sum channel. The distribution for sum channel samples is given by (154) with

$$\mathbf{K}_s = \begin{bmatrix} \beta^2 r_1^2 + \sigma_s^2 & \beta^2 r_1 r_2 \\ \beta^2 r_1 r_2 & \beta^2 r_2^2 + \sigma_s^2 \end{bmatrix}, \tag{159}$$

where $r_1$ and $r_2$ are samples of the main lobe of the matched filter response from (61)-(62). Note that $r_1$ and $r_2$ are functions of the unknown $c$. Finding MLEs for $\beta^2$ and $c$ is equivalent to jointly solving (156) for $\Theta_1 = \beta^2$ and $\Theta_2 = c$. The matrix inverse and variations of $\mathbf{K}$

with respect to $\beta^2$ and $c$ can be expressed as

$$\mathbf{K}_s^{-1} = \frac{1}{(\beta^2 r_1^2 + \sigma_s^2)(\beta^2 r_2^2 + \sigma_s^2) - \beta^4 r_1^2 r_2^2} \times \cdot \begin{bmatrix} \beta^2 r_2^2 + \sigma^2 & -\beta^2 r_1 r_2 \\ -\beta^2 r_1 r_2 & \beta^2 r_1^2 + \sigma^2 \end{bmatrix}, \tag{160}$$

$$\frac{\partial \mathbf{K}_s}{\partial \beta^2} = \begin{bmatrix} r_1^2 & r_1 r_2 \\ r_1 r_2 & r_2^2 \end{bmatrix}, \tag{161}$$

$$\frac{\partial \mathbf{K}_s}{\partial c} = \beta^2 \begin{bmatrix} 2r_1 \frac{\partial r_1}{\partial c} & r_1 \frac{\partial r_2}{\partial c} + r_2 \frac{\partial r_1}{\partial c} \\ r_1 \frac{\partial r_2}{\partial c} + r_2 \frac{\partial r_1}{\partial c} & 2r_2 \frac{\partial r_2}{\partial c} \end{bmatrix}. \tag{162}$$

Evaluation of (156) for $\Theta_i = \beta^2$ gives a linear equation in terms of $\hat{\beta}^2$ which can be solved as

$$\hat{\beta}^2 = \frac{k_{11}\hat{r}_1^2 + k_{22}\hat{r}_2^2 - (\hat{r}_1^2 + \hat{r}_2^2)\sigma_s^2 + 2k_{12}\hat{r}_1\hat{r}_2}{(\hat{r}_1^2 + \hat{r}_2^2)^2}, \tag{163}$$

where $k_{11}$, $k_{12}$, and $k_{22}$ correspond to elements of the sample covariance and

$$\hat{r}_1 = r_1(\hat{c}), \tag{164}$$

$$\hat{r}_2 = r_2(\hat{c}), \tag{165}$$

correspond to the two samples of the matched filter response of the transmitted waveform evaluated at the estimated $\hat{c}$. Substituting (163) into (162) and (160), and further evaluating (156) for $\hat{c}$ gives the following expression:

$$0 = \left(k_{12}\hat{r}_2^2 - k_{12}\hat{r}_1^2 + k_{11}\hat{r}_1\hat{r}_2 - k_{22}\hat{r}_1\hat{r}_2\right) \times \left(k_{11}\hat{r}_1^2 + k_{22}\hat{r}_2^2 - \hat{r}_1^2\sigma_s^2 - \hat{r}_2^2\sigma_s^2 + 2k_{12}\hat{r}_1\hat{r}_2\right), \tag{166}$$

which interestingly does not include the partial derivatives $\frac{\partial r_1}{\partial c}$ and $\frac{\partial r_2}{\partial c}$.[1] Assuming the sample covariance approaches $\mathbf{K}_s$ and $\hat{c}$ approaches $c$ in the limit, evaluation of the limiting form of (166) gives $0 = (0)\left(\beta^2(r_1^2 + r_2^2)^2\right)$. Thus, the second term is not considered useful

---

[1] Actually, evaluation of (156) *does* result in a function of the partials. However, they completely factor out into an expression that does not include the sample covariance, and can thus be eliminated since we desire the solution of (156) equal to zero.

in finding a MLE for $\hat{c}$ since its limiting form does not approach zero. Rewriting the first term of (166) as

$$\frac{k_{11}-k_{22}}{k_{12}}=\frac{\hat{r}_1^2-\hat{r}_2^2}{\hat{r}_1\hat{r}_2}, \tag{167}$$

gives an interesting expression for the MLE of $c$, in which the left side is a quantity involving only measured data and the right side is a quantity that involves the matched filter response of the transmitted waveform as a function of $\hat{c}$. Depending upon the functional form of the matched filter response, (167) may or may not be easy to solve in closed form. Regardless, assuming $c \in [0,1]$, simple search strategies can be devised with (167) using a known functional form of the matched filter response.[2] Once a $\hat{c}$ is found, it can be further used in (163) to compute $\hat{\beta}^2$ if desired.

Substituting (160)-(162) in (158) and computing the matrix inverse gives the CRLB for $c$ as

$$CRLB_{\hat{c}}=\frac{(r_1^2+r_2^2)+\frac{1}{\Re_r}}{2\Re_t\left(r_1\frac{\partial r_2}{\partial c}-r_2\frac{\partial r_1}{\partial c}\right)^2}, \tag{168}$$

with $\Re_r$ as in (12) and $\Re_t$ as in (13). This lower bound on the variance of unbiased estimates of $\hat{c}$ suggests better estimates arise from a higher SNR and a larger number of independent observations. In terms of the target location in range, estimation performance depends upon the selection of the transmitted waveform. One can show that for a triangular matched filter response, the CRB is minimized when a target is centered between matched filter samples.

A simple matched filter output is the triangle function.[3] Under this assumption, the matched filter samples correspond to

$$r_1=(1-c), \tag{169}$$

$$r_2=c, \tag{170}$$

which reduces (167) to

$$(k_{11}-k_{22})\hat{c}^2+(k_{22}-k_{11}-2k_{12})\hat{c}+k_{12}=0, \tag{171}$$

---

[2] The limiting form of $k_{12}$ is a number greater than or equal to zero; however, for a finite number of observations, no guarantees can be made. A negative $k_{12}$ can result in erroneous results, thus ad-hoc approaches must be taken in practice to handle this case.

[3] This assumption can be found extensively in the literature. For examples, see [45], [56], [15], [17].

which has two solutions

$$\hat{c} = \frac{k_{11} - k_{22} + 2k_{12} \pm \sqrt{(k_{11} - k_{22})^2 + 4k_{12}^2}}{2(k_{11} - k_{22})}. \tag{172}$$

Assuming $\bar{\mathbf{K}}_s$ equals $\mathbf{K}_s$ in the limit, the limiting form can be written as

$$\hat{c}_{N\to\infty} = \left( c, \frac{c-1}{2c-1} \right), \tag{173}$$

where the first solution corresponds to the $(-)$ sign and the second solution corresponds to the $(+)$ sign in (172). An additional assumption imposed in (173) is $\beta^2 > 0$, since $\sqrt{(\beta^2)^2}$ is involved in the computation. The second solution can be eliminated, thus $\hat{c}$ is given as (172) using the (-) sign.[4] By rationalizing the numerator, an alternative form of (172) can be found for the numerically unstable case of $k_{11} \approx k_{22}$.

## B.3 $\eta$ Estimation

An estimator for $\eta$ is found using samples of both the sum and difference channel. For the full distribution, $\mathbf{K}^{-1}$ is quite difficult to compute and simplify algebraically with the standard matrix inverse equations for a four-by-four matrix. However, if $\mathbf{K}$ is expressed as the sum of two matrices, a convenient theorem may be used. Defining

$$\mathbf{R} = \begin{bmatrix} r_1^2 & r_1 r_2 \\ r_1 r_2 & r_2^2 \end{bmatrix}, \tag{174}$$

$\mathbf{K}$ can be expressed as the sum of two matrices

$$\mathbf{K} = \mathbf{B} + \mathbf{A}, \tag{175}$$

where

$$\mathbf{B} = \beta^2 \begin{bmatrix} \mathbf{R} & \eta\mathbf{R} \\ \eta\mathbf{R} & \eta^2\mathbf{R} \end{bmatrix}, \tag{176}$$

$$\mathbf{A} = \begin{bmatrix} \sigma_s^2\mathbf{I} & \mathbf{0} \\ \mathbf{0} & \sigma_d^2\mathbf{I} \end{bmatrix}. \tag{177}$$

---

[4] If $\beta^2$ is assumed less than zero, then the two solutions would switch. Therefore, the solution with the $(+)$ sign in (172) corresponds to $\hat{\beta}^2 < 0$, which is outside of our desired solution domain.

Notice that the second column of $\mathbf{B}$ is equal to the first column multiplied by $\eta$, and the second column of $\mathbf{R}$ is equal to the first column multiplied by $r_1/r_0$. Thus, $\mathbf{B}$ is a rank one matrix. Since $\mathbf{B}$ is a rank one matrix, using the result of [33] gives

$$\mathbf{K}^{-1} = (\mathbf{A}+\mathbf{B})^{-1} = \mathbf{A}^{-1} + \frac{1}{a}\mathbf{A}^{-1}\mathbf{B}\mathbf{A}^{-1}, \tag{178}$$

where

$$a = \mathrm{tr}(\mathbf{B}\mathbf{A}^{-1}) + 1. \tag{179}$$

$\mathbf{A}^{-1}$ is easy to compute since it is a diagonal matrix. Analytic evaluation of (178), followed by algebraic manipulations, gives

$$\mathbf{K}^{-1} = \frac{1}{d}\begin{bmatrix} \frac{d\mathbf{I}-\beta^2\sigma_d^2\mathbf{R}}{\sigma_s^2} & -\beta^2\eta\mathbf{R} \\ -\beta^2\eta\mathbf{R} & \frac{d\mathbf{I}-\beta^2\sigma_s^2\eta^2\mathbf{R}}{\sigma_d^2} \end{bmatrix}, \tag{180}$$

where

$$d = \beta^2(r_1^2+r_2^2)(\sigma_d^2+\eta^2\sigma_s^2)+\sigma_s^2\sigma_d^2. \tag{181}$$

Furthermore, the variation of $\mathbf{K}$ with respect to $\eta$ can be expressed as

$$\frac{\partial\mathbf{K}}{\partial\eta} = \begin{bmatrix} \mathbf{0} & \beta^2\mathbf{R} \\ \beta^2\mathbf{R} & 2\beta^2\eta\mathbf{R} \end{bmatrix}. \tag{182}$$

Using (182) and (180) in (156) results in a third order polynomial in $\hat{\eta}$:

$$a_1\hat{\eta}^3 + a_2\hat{\eta}^2 + a_3\hat{\eta} + a_4 = 0, \tag{183}$$

with

$$\begin{aligned} a_1 = {} & \beta^2 r_1^4\sigma_s^4 + 2\beta^2 r_1^2 r_2^2\sigma_s^4 + \\ & \beta^2 r_2^4\sigma_s^4, \end{aligned} \tag{184}$$

$$\begin{aligned} a_2 = {} & \beta^2 k_{13} r_1^4\sigma_s^2 + \beta^2 k_{24} r_2^4\sigma_s^2 + \\ & \beta^2 k_{14} r_1 r_2^3\sigma_s^2 + \beta^2 k_{14} r_1^3 r_2\sigma_s^2 + \\ & \beta^2 k_{23} r_1 r_2^3\sigma_s^2 + \beta^2 k_{23} r_1^3 r_2\sigma_s^2 + \\ & \beta^2 k_{13} r_1^2 r_2^2\sigma_s^2 + \beta^2 k_{24} r_1^2 r_2^2\sigma_s^2, \end{aligned} \tag{185}$$

$$\begin{aligned} a_3 = {} & r_1^2\sigma_d^2\sigma_s^4 - k_{44}r_2^2\sigma_s^4 - \\ & k_{33}r_1^2\sigma_s^4 + r_2^2\sigma_d^2\sigma_s^4 + \\ & \beta^2 k_{11}r_1^4\sigma_d^2 + \beta^2 k_{22}r_2^4\sigma_d^2 - \\ & \beta^2 k_{33}r_1^4\sigma_s^2 - \beta^2 k_{44}r_2^4\sigma_s^2 - \\ & 2k_{34}r_1r_2\sigma_s^4 + \beta^2 r_1^4\sigma_d^2\sigma_s^2 + \\ & \beta^2 r_2^4\sigma_d^2\sigma_s^2 + 2\beta^2 r_1^2r_2^2\sigma_d^2\sigma_s^2 + \\ & 2\beta^2 k_{12}r_1r_2^3\sigma_d^2 + 2\beta^2 k_{12}r_1^3r_2\sigma_d^2 - \\ & 2\beta^2 k_{34}r_1r_2^3\sigma_s^2 - 2\beta^2 k_{34}r_1^3r_2\sigma_s^2 + \\ & \beta^2 k_{11}r_1^2r_2^2\sigma_d^2 + \beta^2 k_{22}r_1^2r_2^2\sigma_d^2 - \\ & \beta^2 k_{33}r_1^2r_2^2\sigma_s^2 - \beta^2 k_{44}r_1^2r_2^2\sigma_s^2, \end{aligned} \tag{186}$$

$$\begin{aligned} a_4 = {} & -(\beta^2 k_{13}r_1^4\sigma_d^2 + \beta^2 k_{24}r_2^4\sigma_d^2 + \\ & k_{13}r_1^2\sigma_d^2\sigma_s^2 + k_{24}r_2^2\sigma_d^2\sigma_s^2 + \\ & k_{14}r_1r_2\sigma_d^2\sigma_s^2 + k_{23}r_1r_2\sigma_d^2\sigma_s^2 + \\ & \beta^2 k_{14}r_1r_2^3\sigma_d^2 + \beta^2 k_{14}r_1^3r_2\sigma_d^2 + \\ & \beta^2 k_{23}r_1r_2^3\sigma_d^2 + \beta^2 k_{23}r_1^3r_2\sigma_d^2 + \\ & \beta^2 k_{13}r_1^2r_2^2\sigma_d^2 + \beta^2 k_{24}r_1^2r_2^2\sigma_d^2). \end{aligned} \tag{187}$$

Note that the MLE described by (183) assumes $\beta^2$ and $c$ are known parameters. We propose using the generalized maximum-likelihood (GML) estimator for $\hat{\eta}$, which involves solving (183) using the $\hat{\beta}^2$ and $\hat{c}$ from (163) and (167).

The CRLB for $\eta$ is computed under the assumption that $\beta^2$ and $c$ are unknown parameters. The variation of $\mathbf{K}$ with respect to $\beta^2$ and $c$ can be expressed as

$$\frac{\partial \mathbf{K}}{\partial \beta^2} = \begin{bmatrix} \mathbf{R} & \eta\mathbf{R} \\ \eta\mathbf{R} & \eta^2\mathbf{R} \end{bmatrix}, \tag{188}$$

$$\frac{\partial \mathbf{K}}{\partial c} = \beta^2 \begin{bmatrix} \frac{\partial \mathbf{K}_s}{\partial c} & \eta\frac{\partial \mathbf{K}_s}{\partial c} \\ \eta\frac{\partial \mathbf{K}_s}{\partial c} & \eta^2\frac{\partial \mathbf{K}_s}{\partial c} \end{bmatrix}, \tag{189}$$

where $\frac{\partial \mathbf{K}_s}{\partial c}$ is given by (162). Using (182), (188), (189), and (180) in (158) followed by a matrix inversion gives

$$CRLB_\eta = \frac{(r_1^2 + r_2^2)\left(\eta^2 + \frac{\sigma_d^2}{\sigma_s^2}\right) + \frac{\sigma_d^2}{\beta^2}}{2\Re_t(r_1^2 + r_2^2)^2}. \tag{190}$$

Note that $\eta$ estimation performance should degrade when a target is centered between matched filter samples, and when a target is located off-boresight (i.e. large $\eta$). As expected, estimation performance increases with a higher target SNR and larger number of pulses.

# APPENDIX C

# UNBIASED MIXING OF STATE ESTIMATES

Unbiased mixing addresses bias issues with the IMM estimator when the state vectors of the assumed kinematic models have different dimension. The mixing step of the IMM algorithm was provided in Chapter 2.2. The unbiased mixing procedure described in this section is an extension of previous work [55] to the case of three modes.

Assume that we have an IMM estimator with three modes. For simplicity, the time index $k$ as seen in Chapter 2.2 is dropped. For mode 1, the state vector estimate and covariance can be written as

$$\hat{\mathbf{x}}^1 = \begin{bmatrix} \hat{\mathbf{x}}_c^1 \\ \hat{\mathbf{x}}_e^1 \end{bmatrix} \quad \text{and} \quad \mathbf{P}^1 = \begin{bmatrix} \mathbf{P}_c^1 & \mathbf{P}_{ce}^1 \\ \mathbf{P}_{ec}^1 & \mathbf{P}_e^1 \end{bmatrix}, \tag{191}$$

where $\hat{\mathbf{x}}_c^1$ and $\mathbf{P}_c^1$ correspond to state elements that are common among the three modes, and $\hat{\mathbf{x}}_e^1$ and $\mathbf{P}_e^1$ correspond to state elements that are "extra" in the first mode. For modes 2 and 3, the state estimate and covariance can be written as

$$\hat{\mathbf{x}}^2 = \left[\hat{\mathbf{x}}_c^2\right] \quad \text{and} \quad \mathbf{P}^2 = [\mathbf{P}_c^2], \tag{192}$$

$$\hat{\mathbf{x}}^3 = \left[\hat{\mathbf{x}}_c^3\right] \quad \text{and} \quad \mathbf{P}^3 = [\mathbf{P}_c^3], \tag{193}$$

which are elements that are common with the first mode.

## *C.1 Mixing for Mode 1*

Issues arise when computing the mixed estimate for the first mode because of the extra terms in the state vector. The conventional approach would mix $\hat{\mathbf{x}}_e^1$, with the (default) values of $\hat{\mathbf{x}}_e^2 = 0$ and $\hat{\mathbf{x}}_e^3 = 0$, which will bias the extra state estimate towards zero [4]. The unbiased mixing procedure will augment the second and third state vector with the extra terms from the first state vector, namely,

$$\hat{\mathbf{x}}^2 = \begin{bmatrix} \hat{\mathbf{x}}_c^2 \\ \hat{\mathbf{x}}_e^1 \end{bmatrix} \quad \text{and} \quad \mathbf{P}^2 = \begin{bmatrix} \mathbf{P}_c^2 & \mathbf{0} \\ \mathbf{0} & \mathbf{P}_e^1 \end{bmatrix}, \tag{194}$$

$$\hat{\mathbf{x}}^3 = \begin{bmatrix} \hat{\mathbf{x}}_c^3 \\ \hat{\mathbf{x}}_e^1 \end{bmatrix} \quad \text{and} \quad \mathbf{P}^3 = \begin{bmatrix} \mathbf{P}_c^3 & \mathbf{0} \\ \mathbf{0} & \mathbf{P}_e^1 \end{bmatrix}. \tag{195}$$

Using this modification, the unbiased mixing procedure for mode 1 will be [55],

$$\begin{aligned} \hat{\mathbf{x}}^{01} &= \hat{\mathbf{x}}^1 \mu_{1|1} + \hat{\mathbf{x}}^2 \mu_{2|1} + \hat{\mathbf{x}}^3 \mu_{3|1} \\ &= \begin{bmatrix} \hat{\mathbf{x}}_c^1 \mu_{1|1} + \hat{\mathbf{x}}_c^2 \mu_{2|1} + \hat{\mathbf{x}}_c^3 \mu_{3|1} \\ \hat{\mathbf{x}}_e^1 \end{bmatrix}, \end{aligned} \tag{196}$$

$$\begin{aligned} \mathbf{P}^{01} = &\left\{ \begin{bmatrix} \mathbf{P}_c^1 & \mathbf{P}_{ce}^1 \\ \mathbf{P}_{ec}^1 & \mathbf{P}_e^1 \end{bmatrix} + \begin{bmatrix} \tilde{\mathbf{P}}_c^{1|1} & \tilde{\mathbf{P}}_{ce}^{1|1} \\ \tilde{\mathbf{P}}_{ec}^{1|1} & \tilde{\mathbf{P}}_e^{1|1} \end{bmatrix} \right\} \mu_{1|1} \\ &+ \left\{ \begin{bmatrix} \mathbf{P}_c^2 & \mathbf{0} \\ \mathbf{0} & \mathbf{P}_e^2 \end{bmatrix} + \begin{bmatrix} \tilde{\mathbf{P}}_c^{2|1} & \tilde{\mathbf{P}}_{ce}^{2|1} \\ \tilde{\mathbf{P}}_{ec}^{2|1} & \tilde{\mathbf{P}}_e^{2|1} \end{bmatrix} \right\} \mu_{2|1} \\ &+ \left\{ \begin{bmatrix} \mathbf{P}_c^3 & \mathbf{0} \\ \mathbf{0} & \mathbf{P}_m^3 \end{bmatrix} + \begin{bmatrix} \tilde{\mathbf{P}}_c^{3|1} & \tilde{\mathbf{P}}_{ce}^{3|1} \\ \tilde{\mathbf{P}}_{ec}^{3|1} & \tilde{\mathbf{P}}_e^{3|1} \end{bmatrix} \right\} \mu_{3|1}, \end{aligned} \tag{197}$$

where

$$\tilde{\mathbf{P}}_c^{m|1} = (\hat{\mathbf{x}}_c^m - \hat{\mathbf{x}}_c^{01})(\hat{\mathbf{x}}_c^m - \hat{\mathbf{x}}_c^{01})^T, \tag{198}$$

$$\tilde{\mathbf{P}}_{ce}^{m|1} = (\hat{\mathbf{x}}_c^m - \hat{\mathbf{x}}_c^{01})(\hat{\mathbf{x}}_e^m - \hat{\mathbf{x}}_e^{01})^T, \tag{199}$$

$$\tilde{\mathbf{P}}_{ec}^{m|1} = (\hat{\mathbf{x}}_e^m - \hat{\mathbf{x}}_e^{01})(\hat{\mathbf{x}}_c^m - \hat{\mathbf{x}}_c^{01})^T, \tag{200}$$

$$\tilde{\mathbf{P}}_e^{m|1} = (\hat{\mathbf{x}}_e^m - \hat{\mathbf{x}}_e^{01})(\hat{\mathbf{x}}_e^m - \hat{\mathbf{x}}_e^{01})^T. \tag{201}$$

Note that in view of (194), (195), and (196), we have $\tilde{\mathbf{P}}_{ce}^{2|1} = \tilde{\mathbf{P}}_{ec}^{2|1} = \tilde{\mathbf{P}}_e^{2|1} = \tilde{\mathbf{P}}_{ce}^{3|1} = \tilde{\mathbf{P}}_{ec}^{3|1} = \tilde{\mathbf{P}}_e^{3|1} = \mathbf{0}$.

## *C.2 Mixing for Mode 2*

The mixed estimate for the second mode, $\hat{\mathbf{x}}^{02}$, is obtained in the standard manner using $\hat{\mathbf{x}}_c^1$, $\hat{\mathbf{x}}_c^2$, $\hat{\mathbf{x}}_c^3$, $\mathbf{P}_c^1$, $\mathbf{P}_c^2$, $\mathbf{P}_c^3$, and the mixing probabilities $\mu_{1|2}$, $\mu_{2|2}$, and $\mu_{3|2}$,

$$\begin{aligned} \hat{\mathbf{x}}^{02} &= \hat{\mathbf{x}}_c^1\mu_{1|2} + \hat{\mathbf{x}}_c^2\mu_{2|2} + \hat{\mathbf{x}}_c^2\mu_{3|2}, && (202) \\ \mathbf{P}^{03} &= \left(\mathbf{P}_c^1 + \tilde{\mathbf{P}}_c^{1|3}\right)\mu_{1|2} \\ &\quad + \left(\mathbf{P}_c^2 + \tilde{\mathbf{P}}_c^{2|2}\right)\mu_{2|2} \\ &\quad + \left(\mathbf{P}_c^3 + \tilde{\mathbf{P}}_c^{3|2}\right)\mu_{3|2}, && (203) \end{aligned}$$

where

$$\begin{aligned} \tilde{\mathbf{P}}_c^{1|2} &= (\hat{\mathbf{x}}_c^1 - \hat{\mathbf{x}}_c^{02})(\hat{\mathbf{x}}_c^1 - \hat{\mathbf{x}}_c^{02})^T, && (204) \\ \tilde{\mathbf{P}}_c^{2|2} &= (\hat{\mathbf{x}}_c^2 - \hat{\mathbf{x}}_c^{02})(\hat{\mathbf{x}}_c^2 - \hat{\mathbf{x}}_c^{02})^T, && (205) \\ \tilde{\mathbf{P}}_c^{3|2} &= (\hat{\mathbf{x}}_c^3 - \hat{\mathbf{x}}_c^{02})(\hat{\mathbf{x}}_c^3 - \hat{\mathbf{x}}_c^{02})^T. && (206) \end{aligned}$$

## *C.3 Mixing for Mode 3*

The mixed estimate for the third mode, $\hat{\mathbf{x}}^{03}$, is obtained in the standard manner using $\hat{\mathbf{x}}_c^1$, $\hat{\mathbf{x}}_c^2$, $\hat{\mathbf{x}}_c^3$, $\mathbf{P}_c^1$, $\mathbf{P}_c^2$, $\mathbf{P}_c^3$, and the mixing probabilities $\mu_{1|3}$, $\mu_{2|3}$, and $\mu_{3|3}$.

$$\begin{aligned} \hat{\mathbf{x}}^{03} &= \hat{\mathbf{x}}_c^1\mu_{1|3} + \hat{\mathbf{x}}_c^2\mu_{2|3} + \hat{\mathbf{x}}_c^2\mu_{3|3}, && (207) \\ \mathbf{P}^{03} &= \left(\mathbf{P}_c^1 + \tilde{\mathbf{P}}_c^{1|3}\right)\mu_{1|3} \\ &\quad + \left(\mathbf{P}_c^2 + \tilde{\mathbf{P}}_c^{2|3}\right)\mu_{2|3} \\ &\quad + \left(\mathbf{P}_c^3 + \tilde{\mathbf{P}}_c^{3|3}\right)\mu_{2|3}, && (208) \end{aligned}$$

where

$$\begin{aligned} \tilde{\mathbf{P}}_c^{1|3} &= (\hat{\mathbf{x}}_c^1 - \hat{\mathbf{x}}_c^{03})(\hat{\mathbf{x}}_c^1 - \hat{\mathbf{x}}_c^{03})^T, && (209) \\ \tilde{\mathbf{P}}_c^{2|3} &= (\hat{\mathbf{x}}_c^2 - \hat{\mathbf{x}}_c^{03})(\hat{\mathbf{x}}_c^2 - \hat{\mathbf{x}}_c^{03})^T, && (210) \\ \tilde{\mathbf{P}}_c^{3|3} &= (\hat{\mathbf{x}}_c^3 - \hat{\mathbf{x}}_c^{03})(\hat{\mathbf{x}}_c^3 - \hat{\mathbf{x}}_c^{03})^T. && (211) \end{aligned}$$

# REFERENCES

[1] Alouani, A. and Blair, W. D., “Use of a Kinematic Constraint in Tracking Constant Speed, Maneuvering Targets,” *IEEE Transactions on Automatic Control*, vol. 38, no. 7, pp. 1107–1111, 1993.

[2] Athans, M., Wishner, R., and Bertolini, A., “Suboptimal State Estimation for Continuous-time Nonlinear Systems from Discrete Noisy Measurements,” *IEEE Transactions on Automatic Control*, vol. 13, no. 5, pp. 504–514, 1968.

[3] Bar-Shalom, Y., Li, X., and Kirubarajan, T., *Estimation with Applications to Tracking and Navigation: Theory Algorithms and Software.* Wiley-Interscience, 2001.

[4] Bar-Shalom, Y., Willett, P., and Tian, X., *Handbook on Tracking and Data Fusion.* YBS Publishing, 2011.

[5] Blackman, S., *Design and Analysis of Modern Tracking Systems.* 1999.

[6] Blackman, S., Dempster, R., Busch, M., and Popoli, R., “IMM/MHT Solution to Radar Benchmark Tracking Problem,” *IEEE Transactions on Aerospace and Electronic Systems*, vol. 35, no. 2, pp. 730–738, 1999.

[7] Blair, W., *Monopulse Processing and Tracking of Unresolved Targets.* PhD thesis, University of Virginia, 1998.

[8] Blair, W. and Brandt-Pearce, M., “Statistical Description of Monopulse Parameters for Tracking Rayleigh Targets,” *IEEE Transactions on Aerospace and Electronic Systems*, vol. 34, no. 2, pp. 597–611, 1998.

[9] Blair, W. and Brandt-Pearce, M., “Unresolved Rayleigh Target Detection using Monopulse Measurements,” *IEEE Transactions on Aerospace and Electronic Systems*, vol. 34, no. 2, pp. 543–552, 1998.

[10] Blair, W. and Brandt-Pearce, M., “Monopulse DOA Estimation of Two Unresolved Rayleigh Targets,” *IEEE Transactions on Aerospace and Electronic Systems*, vol. 37, no. 2, pp. 452–469, 2001.

[11] Blair, W. and Watson, G., “IMM Algorithm for Solution to Benchmark Problem for Tracking Maneuvering Targets,” in *Proceedings of SPIE*, vol. 2221, pp. 476–488, 1994.

[12] Blair, W., Watson, G., and Hoffman, S., “Benchmark Problem for Beam Pointing Control of Phased Array Radar against Maneuvering Targets,” in *1994 American Control Conference*, vol. 2, pp. 2071–2075, IEEE, 1994.

[13] Blair, W., Watson, G., Kirubarajan, T., and Bar-Shalom, Y., “Benchmark for Radar Allocation and Tracking in ECM,” *IEEE Transactions on Aerospace and Electronic Systems*, vol. 34, no. 4, pp. 1097–1114, 1998.

[14] Blom, H. and Bar-Shalom, Y., "The Interacting Multiple Model Algorithm for Systems with Markovian Switching Coefficients," *IEEE Transactions on Automatic Control*, vol. 33, no. 8, pp. 780–783, 1988.

[15] Brown, G., Blair, W., and Ogle, T., "AOA Estimation with Merged Measurements from Squint Beam Monopulse Data in Conjunction with Multiple Range Samples," in *Proceedings of SPIE*, vol. 5204, pp. 446–457, 2003.

[16] Burg, J., Luenberger, D., and Wenger, D., "Estimation of Structured Covariance Matrices," *Proceedings of the IEEE*, vol. 70, no. 9, pp. 963–974, 1982.

[17] Cann, A., "Range Gate Straddling Loss and Joint Probability with Partial Correlation," *IEEE Transactions on Aerospace and Electronic Systems*, vol. 38, no. 3, pp. 1054–1058, 2002.

[18] Coogle, R., Glass, J., Smith, L., Miceli, P., Register, A., West, P., and Blair, W., "A MIMO Radar Benchmarking Environment," in *Proceedings of 2011 IEEE Aerospace Conference*, 2011.

[19] DiFranco, J. and Rubin, B., *Radar Detection*. SciTech Publishing, 2004.

[20] Dufour, F. and Mariton, M., "Tracking a 3D Maneuvering Target with Passive Sensors," *IEEE Transactions on Aerospace and Electronic Systems*, vol. 27, no. 4, pp. 725–739, 1991.

[21] Glass, J., Blair, W., and Bar-Shalom, Y., "IMM Estimators with Unbiased Mixing for Tracking Targets Performing Coordinated Turns," *Proceedings of 2013 IEEE Aerospace Conference*, 2013.

[22] Glass, J., Blair, W., and Bar-Shalom, Y., "Optimizing radar signal to noise ratio for tracking maneuvering targets," in *2014 International Conference on Information Fusion (FUSION)*, 2014.

[23] Glass, J. D. and Blair, W., "Monopulse DOA Estimation Using Adjacent Matched Filter Samples," in *2015 IEEE Aerospace Conference*, 2014.

[24] Glass, J. D. and Blair, W., "Range Estimation Using Adjacent Matched Filter Samples," in *2014 IEEE Aerospace Conference*, 2014.

[25] Glass, J. D. and Blair, W., "Detection of Rayleigh Targets using Adjacent Matched Fliter Samples," *Accepted to IEEE Transactions on Aerospace and Electronic Systems*, 2015.

[26] Glass, J. D., Blair, W., and Lanterman, A., "Joint-Bin Monopulse Processing of Rayleigh Targets," *Submitted to IEEE Transactions on Aerospace and Electronic Systems*, 2015.

[27] Grad, A. and Solomon, H., "Distribution of Quadratic Forms and Some Applications," *The Annals of Mathematical Statistics*, vol. 26, no. 3, pp. 464–477, 1955.

[28] Johnson, D. and Dudgeon, D., *Array Signal Processing: Concepts and Techniques*. Prentice-Hall, 1993.

[29] Kalman, R., "A New Approach to Linear Filtering and Prediction Problems," *Transactions of the ASME–Journal of Basic Engineering*, vol. 82, no. Series D, pp. 35–45, 1960.

[30] Kirubarajan, T., Bar-Shalom, Y., Blair, W., and Watson, G., "IMMPDAF for Radar Management and Tracking Benchmark with ECM," *IEEE Transactions on Aerospace and Electronic Systems*, vol. 34, no. 4, pp. 1115–1134, 1998.

[31] Li, X. and Bar-Shalom, Y., "Multiple-model Estimation with Variable Structure," *IEEE Transactions on Automatic Control*, vol. 41, no. 4, pp. 478–493, 1996.

[32] Mahafza, B. and Elsherbeni, B., "Radar Detection," in *Wireless, Networking, Radar, Sensor Array Processing, and Nonlinear Signal Processing* (Madisetti, V., ed.), CRC Press, 2010.

[33] Miller, K., "On the Inverse of the Sum of Matrices," *Mathematics Magazine*, vol. 54, no. 2, pp. 67–72, 1981.

[34] Mosca, E., "Angle Estimation in Amplitude Comparison Monopulse Systems," *IEEE Transactions on Aerospace and Electronic Systems*, no. 2, pp. 205–212, 1969.

[35] Nabaa, N. and Bishop, R., "Validation and Comparison of Coordinated Turn Aircraft Maneuver Models," *IEEE Transactions on Aerospace and Electronic Systems*, vol. 36, no. 1, pp. 250–259, 2000.

[36] Nickel, U., "Overview of Generalized Monopulse Estimation," *IEEE Aerospace and Electronic Systems Magazine*, vol. 21, no. 6, pp. 27–56, 2006.

[37] Papoulis, A. and Pillai, S., *Probability, Random Variables, and Stochastic Processes.* McGraw-Hill, fourth ed., 2002.

[38] Porat, B., *Digital Processing of Random Signals: Theory and Methods.* Prentice-Hall, Inc., 1994.

[39] Richards, M., *Fundamentals of Radar Signal Processing.* McGraw-Hill, 2005.

[40] Rong Li, X. and Jilkov, V., "Survey of Maneuvering Target Tracking. Part I: Dynamic Models," *IEEE Transactions on Aerospace and Electronic Systems*, vol. 39, no. 4, pp. 1333–1364, 2003.

[41] Rong Li, X. and Jilkov, V., "Survey of Maneuvering Target Tracking. Part V. Multiple-model Methods," *IEEE Transactions on Aerospace and Electronic Systems*, vol. 41, no. 4, pp. 1255–1321, 2005.

[42] Selin, I., "Detection of Coherent Radar Returns of Unknown Doppler Shift," *IEEE Transactions on Information Theory*, vol. 11, no. 3, pp. 396–400, 1965.

[43] Sherman, S., *Monopulse Principles and Techniques.* Artech House, 1984.

[44] Slocumb, B. and Blair, W., "EM-Based Measurement Fusion for HRR Radar Centroid Processing," in *Proceedings of SPIE*, vol. 4728, 2002.

[45] Slocumb, B. and Blair, W., "Maximum Likelihood Narrowband Radar Data Segmentation and Centroid Processing," in *Proceedings of SPIE*, vol. 5204, 2003.

[46] Tian, X. and Bar-Shalom, Y., "Coordinate Conversion and Tracking for Very Long Range Radars," *IEEE Transactions on Aerospace and Electronic Systems*, vol. 45, no. 3, pp. 1073–1088, 2009.

[47] Tullsson, B., "Monopulse Tracking of Rayleigh Targets: A Simple Approach," *IEEE Transactions on Aerospace and Electronic Systems*, vol. 27, no. 3, pp. 520–531, 1991.

[48] van Keuk, G. and Blackman, S. S., "On Phased-Array Radar Tracking and Parameter Control," *IEEE Transactions on Aerospace Electronic Systems*, vol. 29, pp. 186–194, 1993.

[49] Wang, H., Kirubarajan, T., and Bar-Shalom, Y., "Precision Large Scale Air Traffic Surveillance using IMM/Assignment Estimators," *IEEE Transactions on Aerospace and Electronic Systems*, vol. 35, no. 1, pp. 255–266, 1999.

[50] Wang, Z., Sinha, A., Willett, P., and Bar-Shalom, Y., "Angle Estimation for Two Unresolved Targets with Monopulse Radar," *IEEE Transactions on Aerospace and Electronic Systems*, vol. 40, no. 3, pp. 998–1019, 2004.

[51] Watson, G. and Blair, W., "IMM Algorithm for Tracking Targets that Maneuver through Coordinated Turns," in *Proceedings of SPIE*, vol. 1698, pp. 236–247, 1992.

[52] Willett, P., Blair, W., and Bar-Shalom, Y., "Correlation Between Horizontal and Vertical Monopulse Measurements," *IEEE Transactions on Aerospace and Electronic Systems*, vol. 39, no. 2, pp. 533–549, 2003.

[53] Willett, P., Blair, W., and Zhang, X., "The Multitarget Monopulse CRLB for Matched Filter Samples," *IEEE Transactions on Signal Processing*, vol. 55, no. 8, pp. 4183–4197, 2007.

[54] Xie, J. and Luo, Y., "Comments on "Range Gate Straddling Loss and Joint Probability with Partial Correlation"," *IEEE Transactions on Aerospace and Electronic Systems*, vol. 45, no. 2, pp. 773–775, 2009.

[55] Yuan, T., Bar-Shalom, Y., Willett, P., Mozeson, E., Pollak, S., and Hardiman, D., "A Multiple IMM Estimation Approach with Unbiased Mixing for Thrusting Projectiles," *IEEE Transactions on Aerospace and Electronic Systems*, vol. 48, no. 4, pp. 3250–3267, 2012.

[56] Zhang, X., Willett, P., and Bar-Shalom, Y., "Monopulse Radar Detection and Localization of Multiple Unresolved Targets via Joint Bin Processing," *IEEE Transactions on Signal Processing*, vol. 53, no. 4, pp. 1225–1236, 2005.

[57] Zhang, X., Willett, P., and Bar-Shalom, Y., "Detection and Localization of Multiple Unresolved Extended Targets via Monopulse Radar Signal Processing," *IEEE Transactions on Aerospace and Electronic Systems*, vol. 45, no. 2, pp. 455–472, 2009.

# VITA

John D. Glass was born in Dyersburg, Tennessee, in 1985. He received the Bachelor's of Science in Electrical Engineering from the University of Tennessee in 2009, and the Master's of Science in Electrical and Computer Engineering from Georgia Institute of Technology in 2010. During his undergraduate studies, John did several co-op and internship semesters at Honeywell, Inc., in Clearwater, Florida, and the Y-12 National Security Complex in Oak Ridge, Tennessee. He was a graduate research assistant in the Electronic Systems Lab of the Georgia Tech Research Institute from 2010 to 2013. In June 2013 John became a full-time researcher in the Sensors and Electromagnetic Applications Lab of the Georgia Tech Research Institute. During graduate school John was the associate editor of student research for the *IEEE Aerospace and Electronic Systems Magazine.* He plans to receive the Ph.D. degree in Electrical and Computer Engineering in May 2015.